creative commons

COMMONS DEED

저작자표시-비영리-변경금지 2.0 대한민국

이용자는 아래의 조건을 따르는 경우에 한하여 자유롭게

- 이 저작물을 복제, 배포, 전송, 전시, 공연 및 방송할 수 있습니다.

다음과 같은 조건을 따라야 합니다:

저작자표시. 귀하는 원저작자를 표시하여야 합니다.

비영리. 귀하는 이 저작물을 영리 목적으로 이용할 수 없습니다.

변경금지. 귀하는 이 저작물을 개작, 변형 또는 가공할 수 없습니다.

- 귀하는, 이 저작물의 재이용이나 배포의 경우, 이 저작물에 적용된 이용허락조건을 명확하게 나타내어야 합니다.
- 저작권자로부터 별도의 허가를 받으면 이러한 조건들은 적용되지 않습니다.

저작권법에 따른 이용자의 권리는 위의 내용에 의하여 영향을 받지 않습니다.

이것은 이용허락규약(Legal Code)을 이해하기 쉽게 요약한 것입니다.

Disclaimer

dCollection

Doctor of Philosophy

Exploring the Electrolyte Additives For Aqueous Zinc Ion Batteries

The Graduate School

of the University of Ulsan

Department of Chemical Engineering

Haiji Huang

Exploring the Electrolyte Additives for Aqueous Zinc Ion Batteries

Supervisor: Prof. Won Mook Choi, Prof. Jianfeng Mao, Prof. Pinhua Rao

A Dissertation

Submitted to

the Graduate School of the University of Ulsan

In partial Fulfillment of the Requirements

for the Degree of

Doctor of Philosophy

By

Haiji Huang

Department of Chemical Engineering

University of Ulsan, Korea

June 2022

Exploring the Electrolyte Additives for Aqueous Zinc Ion Batteries

This certifies that the dissertation of Haiji Huang is approved.

Committee Chair Prof. Sung Gu Kang

Committee Member Prof. Seung Hyun Hur

Committee Member Prof. Jin Suk Chung

Committee Member Prof. Won Mook Choi

Committee Member Prof. Jianfeng Mao

School of Chemical Engineering

University of Ulsan, Korea

June 2022

DEDICATION

All Glory to God

ACKNOWLEDGEMENTS

This thesis would not have been completed without the all-around support by the researchers in the College of Chemistry and Chemical Engineering of University of Ulsan and Shanghai University of Engineering Science. I would like to deliver a sincere appreciate to my first supervisor, Professor Won Mook Choi during my academic research in Ulsan, who not only gave me the opportunity to become the one member of Flexible and Nano Materials Lab, but also guide me to be a rigorous and wise researcher with the personalities of kind and patience. And I also would like to thanks to the help by Prof. Won Mook Choi, Research Prof. Tran Van Tam, Mrs. Kyung Jo Lim, M.S. Sim Sori, Ph.D. Di Liu, Ph.D. Yiwen Hong and M.S. Yinong Wang. And I also would like to thanks the support of life and study from Prof. Eun Suok Oh, Prof. Sung Gu Kang, Prof. Ik-Keun Yoo, Prof. Kuen-Garp Ryu, Prof. Seung Hyun Hur, Prof. Eun Woo Shin, Prof. Jin Suk Chung, Prof. Soon Ho Hong in University of Ulsan and Prof. Prof. Pinhua Rao Prof. Jiachang Zhao, Prof. Ya Li, Prof. Yichuan Rui, Prof. Bohejin Tang, Prof. Runkai Wang, Mrs. Lili Yan, Mrs. Jinjie Wang, Ms. Wenjuan Zhang, and Mr. Hao Yin after come back to Shanghai University of Engineering Science. And I would like to pay my highest respects to the Distinguished Professor Jianfeng Mao, Professor Zaiping Guo (University of Adelaide), Professor Pinhua Rao, Professor Jiachang Zhao for their great help and instruction of research continuously. And I would like to thanks to the Prof. Kenneth Davey (University of Adelaide) for his help for the language polishing. And I also would like to thanks to team members, including M.S. Qiong Jiang, M.S. Dongmei Xie, M.S. Hao Wang, Ms. Yan Wang, M.S. Zedong Zhang and many friends in the Department of Chemical and Chemical, including Ph.D. Yuanyuan Li, Ph.D. Linlin Wang, Ph.D. Kaiming Jiang, Ph.D. Lijun Sui, Ph.D. Yue Xu, Ph.D. Yanchunxiao Qi, Ph.D. Yuanyuan Wang, Ph.D. Hongyan Yu, Ph.D. Yujie Wu, Ph.D. Yiming Meng, Ph.D. Mi Tian, Ph.D. Mingyan Wang, Ph.D. Lihua Wen, M.S. Guoqiang Hao, M.S. Rao Wang, M.S. Jiakai Du, M.S. Kainan Huang, M.S. Yonghang Liu, M.S. Siyu Jiang, M.S. Liqun Hu, M.S. Yutian Xie, M.S. Yongliang Liu, M.S.W Zixiu

Wang, M.F.A. Jun Ma, M.S. Yanchun Xie, Mr. Hongqiang Wan, M.S. Hao Liu, M.S. Ruihao Zhang, M.S. Zhuo Wang, M.S. M.S. Zongjie Chen, Mr. Di Sun, M.S. Guo Zhao, M.S. Yaozhong Liang, Mr. Jiaju Zhang, Mr. Chenglong Lv, M.S. Zongjie Chen, M.S. Shuo Cao, Mr. Honghao Chen and Mr. Bowen Tang who assisted me to carry out experiments and tests and be always with me. For FTIR test, I would like to thank to the Prof. Jinjie Wang for her patient instrument maintenance and guidance again and again. For the NMR test and patient guidance, I would like to thank to the Mrs. Wu (Shanghai Jiaotong University) and Mrs. Lili Yan. These silently paid and hard-working people ensure the proper functioning of the whole institute. And I would like to thank my wife Hongmei Zhao, my mother Yuying Gao, my father Zhongfa Huang, and a lot of favourite friends, more precisely, truth-seekers in CCC, SFC, Kosin University and Ulsan church for their full supports of life, moral and ethical guidance and delicious food made of love. Moreover, I would like to express my appreciate to my dear friends for their company and their prayers for my graduation and my relationship with my wife and my family (mother and father) , including D.T. Jinsheng Zhong, Mrs. Yating, Mr. Jian Sun, Mrs. En Liu, M.S. Zhuang Li, Mrs. Junwei Gong, Mr. Youwei Yang, Mrs. Juan Ma, Ph.D. Chaochao Shen, M.Ed Lili Zhang, M.E. Shang Zhang, Mrs. Yuanyuan Zhang, Mr. Kun Zhou, Mrs. Xiao Zhang, Mr. Weimin Tao, Mrs. Xinyue Tan, Mr. Dewei Gong, Mrs. Lijun Deng, M.A. Linwei Chang, Mrs. Yue Zhang, M.M. Shengjie Jia, Ms. Danqian Wang, Mr. Yang Yang, M.Mus Yujie Li, D.M.A Yue Hou, J.M. Attorney Yang, Ms. Linyan Gu, Ms. Yongping Yu, M.S. Juan Huang, Ms. Yuanmei Zhang, Ms. Menyao Peng, M.S. Rui Yu, Ms. Juan Gao, Mr. Shilong Wu, Mr. Xiangfei Liu, M.M. Yu Zhang, Mr. Jun Chen, Mr. Wenrang Liu, Mr. Qiang Zhang, Mr. Tianzhu Zhang, Mr. Tengfei Ma, Ms. Xuemie Li, Ms. Li Li, Mr. Wenqiang Chi, Mr. Mingfei, Mr. Youmin Zhu, Mr. Qiang Guo, Ms. Xue Chen, Ms. Haolin Jia, Ms. Yasheng Bai, Mr. Zhonghui Qian, Mr. Xiuming, Mr. Zaiming Piao, Mr. Zhengzhe Ding, Mrs. Zhengnan Jin, Mrs. Haishu Jin, Mrs. Yonglan Jin, Mrs. Xuemei Liang, Mr. Xiangchu Li, D.T. Hongbin Yu, B.M.E Yuanzhao Duan, B.M.E Wenqin Li, M.S. Jiacheng Li, M.Div. Yaocai Huang, M.Div. Minqiang Tan, M.S. Zhenyu Jia, Mr. Jingying Liu, Mrs. Zhimin Huang, Mr. Dongxu Cui, Mrs. Yuan Chen, Ph.D. He Wang, Mrs. Jiahong Li, M.A.E

Jincheng Wang, Ph.D. Yingqing Chen, M.S. Guoen Li, Mrs. Yanping Liang, Mrs. Yuan Hao, Mrs. Xin Zhou, M.S. Qin Tang, M.S. Zhaoxiu Meng, M.S. Ying Han, Mrs. Fan Zhang, Mr. Grady Morley, Ph.D. Riming Nie, and Ph.D. Shiming Liu.

I am also grateful for the support from the Basic Science Research Program through the National Research Foundation of Korea (NRF) funded by The Ministry of Education (NRF-2018R1D1A1B07047042), the Priority Research Center Program through the National Research Foundation of Korea (NRF) funded by the Ministry of Education (2021R1A6A1A03038858), the Basic Science Research Program through the National Research Foundation of Korea (NRF) funded by the Ministry of Science and ICT (MSIT) (2021R1F1A1063291), the Priority Research Center Program through the National Research Foundation of Korea (NRF) funded by the Ministry of Education (2021R1A6A1A03038858) and the financial support from Shanghai University of Engineering Science.

Thanks, God, for bringing so many lovely people including teachers, parents, and friends into my life to help and support me, and with their help, I was able to complete the doctoral degree.

ABSTRACT

To greatly improve the ecological environment and achieve the target of carbon neutrality around 2050s, it is significant to develop a kind of low-cost convenient-eco-friendly-green assemble-disassemble-recycle next-generation energy system. It is urgent to develop electrical energy storage which could achieve discharge-charge quickly and effective long life-span of advanced all-size devices and electrics. Rechargeable aqueous zinc batteries have been considered as a promising candidate for large-scale energy storage due to the low cost, intrinsic safety, low toxicity, the abundance of materials, and the unique features of zinc: good conductivity (5.91 microohm), low redox potential (-0.7626 V vs. standard hydrogen electrode, in acidic solution, 298.15 K), high gravimetric capacity (821 mAh g^{-1}) and high volumetric capacity (5855 Ah L^{-1} compared to 2061 Ah L^{-1} for Li anode). Nevertheless, state-of-the-art techniques of ZIBs are far from satisfactory of industry standard due to the difficult ability to improve the poor reversibility (caused by evolution of hydrogen, the metal dendrite and by-products, etc.) of Zn anode, matching with the dissolution of cathode materials (such as shuttle effect), resulting in the obvious decline in battery performance.

In the acidic electrolytes, HER inevitably happens and limits the coulombic efficiency (CE) of half-cell or full-cell, significantly influencing on the capacity. Further, the evolution of hydrogen makes the environment instability and annoys the hydroxyl ion (OH^-) localized concentration around the surface of zinc anode, which accelerates the corrosion reaction of zinc and form the by-products (e.g., $Zn_4SO_4(OH)_6 \cdot nH_2O$). The compound acts as an isolation between zinc anode and electrolyte, not only deteriorate the ability to ion-electron diffusion but also have the side effects on the reversibility of zinc plating/stripping. And the evident Zn dendrite growth has a close relationship with the Coulombic efficiency (CE) during battery cycling and the battery lifespan. In the electrolytes, Zn^{2+} ion could form the solvation structure like a chelate structure, which is surrounded by six H_2O molecules. These strong

bonds make the Zn firmly riveted from desolvation and deposition more difficult, like a high energy barrier.

In conclusion, it is necessary to develop strategies for modulating the kinetics of Zn electrodeposition so as to obtain a smoothly homogeneous reversible Zn nucleation. Therefore, one of the strategies is to add the electrolyte additives to minimize the electrolysis of water (e.g., electrolyte decomposition) while suppressing the dendrite growth and parasite reactions as well as controlling regulation of the solvation structure which significantly affect the aqueous Zn batteries.

In the first case, the effects of electrolyte additive, dimethyl sulfone or (methylsulfonyl)methane (MSM) on the electrochemical performance of Zn/MnO_2 was studied. The results show the additive promotes the deposit pattern of Zn ion, intending the dendrite-free Zn plating/stripping highly reversible reaction. Meanwhile, the hydrophilic ability of metal face was optimized by introducing the additive, accelerating the Zn-ion diffusion at the Zn anode/electrolyte interface. Benefiting from these effects, the capacity and cycling life of Zn/MnO_2 batteries were improved to some certain degree.

In the second case, Zn metal plating/stripping mechanism was thoroughly explored in 2M $ZnSO_4$ electrolyte, demonstrating that the poor performance was ascribed to the formation of a by-product $Zn_4SO_4(OH)_6{\cdot}5H_2O$ flakes, hydrogen evolution reaction, and extremely grievous pulverization dendrite growth. To suppress the dendrite growth and parasitic reactions, a kind of rust remover and reactive organic diluent, Gamma-butyrolactone ($C_4H_6O_2$, GBL) was introduced to be a new electrolyte additive into $ZnSO_4$ electrolyte for dendrite-free ZIBs. A small volume of GBL (1% solvent) in 2M $ZnSO_4$ could markedly improve the performance of Zn plating/stripping behavior under different current density (4200 h for 1 mAh cm^{-2} at 1 mAh cm^{-2}; 1170 h for 10 mAh cm^{-2} at 10 mA cm^{-2}; and 140 h for 20 mAh cm^{-2} at 20 mA cm^{-2}). The high average CE of MnO_2-cathodes and a high plating/stripping average CE of 99.7% for Zn anodes demonstrate that the problem of MnO_2 dissolution and dendrite Zn growth have been effectively suppressed. Experiment and theoretical calculations confirmed that GBL could assist to help changing the solvation structure of Zn^{2+}, alleviating the H_2O activation

and prohibit the by-product to some extent. Additionally, Zn metal surface was inclined to absorb GBL other than H_2O, which is in favor of hoisting the nucleation overpotential and guiding the uniform deposition. It is noteworthy that 2M $ZnSO_4$-GBL electrolyte is nonflammable, and conveniently stable, which is promising for next generation green and high-performance Zn-ion batteries. And the outstanding performance was attributed to the i) the nanoarchitecture that provides electrochemically large active sites, leading to the high energy storing performance and ii) the enhanced ionic transport from the hierarchically interconnected 2D-Zn nanostructures.

In the third case, an important chemical raw material, α-pyrrolidone, which can be used as solvent and intermediate of organic synthesis. The effects of α-pyrrolidone on the electrochemical performance of Zn/MnO_2 was studied. The results show the additive promotes the deposit pattern of Zn ion, intending the dendrite-free Zn plating/stripping highly reversible reaction. Meanwhile, the hydrophilic ability of metal face was optimized by introducing the additive, accelerating the Zn-ion diffusion at the Zn anode/electrolyte interface. Benefiting from these effects, the capacity and cycling life of Zn/MnO_2 batteries were improved to some certain degree.

In the future work, I would try more organic molecules as electrolyte additives such as Aspartame, Betaine, and Glucurolactone, etc.

In summary, the chaos of low CE and terrible reversibility of Zn electrode cause of the dendrite growth, hydrogen evolution reaction, by-products and metal corrosion in mild electrolyte severely hinder the further development of aqueous Zn-based batteries at the industry standard. I believe this doctoral research could provide a fundamental understanding of Zn electrode interplay with aqueous-organic media and presents a potential and perspective direction to develop and open up the electrolyte additives in purpose of making advanced aqueous Zn-ion batteries more closely to be commercialized.

TABLE OF CONTENTS

DEDICATION ..... **I**

ACKNOWLEDGEMENTS ..... **II**

ABSTRACT ..... **V**

TABLE OF CONTENTS ..... **VIII**

CHAPTER 1 INTRODUCTION **1**

1.1 RESEARCH BACKGROUND **1**
1.2 OBJECTIVES OF THE RESEARCH **4**
1.3 THESIS STRUCTURE **5**
REFERENCES **6**

CHAPTER 2 LITERATURE REVIEW **7**

2.1 INTRODUCTION **7**
2.2 PRINCIPALS OF AQUEOUS ZINC ION BATTERIES **9**
2.2.1 Reactions of Water Molecules 9
2.2.2 Zn deposition process 12
2.2.3 Zinc Manganese-Based Reactions 14
2.3 ISSUES, MECHANISMS AND STRATEGIES **22**
2.3.1 Electrochemical Stability Window 24
2.3.2 Side reactions, corrosion and formation of by-products 26
2.3.3 Zn dendrite 30
2.3.3.1 Electrolytes and Zn Dendrites 33
2.3.3.2 Accumulation Effect 34
2.3.4 Advancements in Zn Dendrite Protection 35
2.3.4.1 Artificial Interface Layer 35
2.3.4.2 Inorganic Interface Layer 36
2.3.4.3 Organic Interface Layer 38
2.3.4.4 Electrolyte Modification 40
2.3.4.5 Additives 41
REFERENCES **44**

CHAPTER 3 EXPERIMENTAL SECTIONS **56**

3.1 OVERVIEW **56**
3.2 CHEMICALS AND MATERIALS **59**
3.3 MATERIAL PREPARATIONS **59**
3.4 CHARACTERIZATIONS **62**
3.4.1 Fourier-transform Infrared spectroscopy (FT-IR) 62
3.4.2 Raman spectroscopy 63
3.4.3 ^{2}H nuclear magnetic resonance (NMR) 63

3.4.4 X-ray diffraction (XRD) 64
3.4.5 Scanning electron microscope (SEM) 65
3.4.6 In situ optical microscopy 65
3.4.7 Contacting angle measurements 65
3.5 THEORETICAL CALCULATIONS 66
3.5.1 Ab-initio (VASP) simulations 66
3.5.2 Quantum Chemistry Calculations 67
3.5.3 Molecular Dynamic (MD) Emulations 67
3.6 ELECTROCHEMICAL MEASUREMENTS 69
3.6.1 Cyclic voltammetry (CV) 69
3.6.2 Galvanostatic charge/discharge curves 70
3.6.3 Linear Sweep voltammetry (LSV) 70
3.6.4 Polarization curve test 70
3.6.5 Electrochemical impedance spectroscopy (EIS) 70
REFERENCES 71

CHAPTER 4 MSM AS ELECTROLYTE ADDITIVES FOR AQUEOUS ZN-ION BATTERIES 75

4.1 INTRODUCTION 75
4.2 RESULTS AND DISCUSSION 77
4.2.1 Stability of the Zn Electrode 77
4.2.2 Reversibility of the Zn Electrode 78
4.2.3 Chemical and physical properties of electrolytes 81
4.2.4 Theoretical Calculation 86
4.2.5 Mechanism Analysis 86
4.3 CONCLUSION 87
REFERENCES 88

CHAPTER 5 GBL AS ELECTROLYTE ADDITIVES FOR AQUEOUS ZN-ION BATTERIES 99

5.1 INTRODUCTION 99
5.2 RESULTS AND DISCUSSION 101
5.2.1 Stability of the Zn Electrode 101
5.2.2 Reversibility of the Zn Electrode 103
5.2.3 Scanning Electron Microscope 103
5.2.4 Chemical and physical properties of electrolytes 107
5.2.5 Molecular Dynamics (MD) Simulation 107
5.2.6 Quantum Chemistry Computation 109
5.2.7 Ab-initio theoretical calculation 112
5.2.8 Mechanism Analysis 113
5.3 CONCLUSION 119
REFERENCES 125

CHAPTER 6 PYRROLIDONE AS ELECTROLYTE ADDITIVES FOR AQUEOUS ZN-ION BATTERIES 129

6.1 INTRODUCTION 129

6.2 RESULTS AND DISCUSSION **131**
6.2.1 Stability of the Zn Electrode 131
6.2.2 Reversibility of the Zn Electrode 131
6.2.3 Chemical and physical properties of electrolytes 135
6.2.4 Mechanism Analysis 137
6.3 CONCLUSION **138**
REFERENCES **146**

CHAPTER 7 CONCLUSION AND PROSPECTS **150**

7.1 CONCLUSION **150**
7.2 PROSPECTS FOR FUTURE WORK **153**
REFERENCES **156**

APPENDIX A: PUBLICATIONS **157**

APPENDIX B: CONFERENCES & ACTIVITIES **157**

LIST OF FIGURES, TABLES and ABBREVIATIONS

Figure 1.1 Ragone plot of some conventional commercialized batteries, typical metal ions (including Li^+, Na^+, K^+, Zn^{2+}, Mg^{2+}, Al^{3+} and Ca^{2+}), and non-metal ion charge carrier-based ABs.

Figure 1.2 (a) Comparison of cost, abundance, and volumetric capacity of metal anodes. (b) Comparison between Zn and other metal anodes in terms of redox potential and ionic conductivity. Copyright 2020, John Wiley and Sons. (c) Price comparison of commonly-used salts in different batteries. The price is calculated based on the available largest pack size from Sigma. Copyright 2021, Royal Society of Chemistry. (d) The three criteria for the future road to commercialization of AZIBs.

Figure 2.1 Summary of the as-developed electrolyte systems of AZIBs with distinct compositions and features related to the dendrite issue of the Zn anode.

Figure 2.2 Diagram showing the types of organic compounds used in AZIBs.

Figure 2.3 (a) Pourbaix diagram of Zn-H_2O system at 25 °C. (b) Schematic illustration of four major issues that may occur on the zinc electrode: insert label (a) dendrite growth, (b) shape change, (c) passivation, and (d) hydrogen evolution. (c-d) Schematic open-circuit energy diagram of (c) aqueous and (d) organic electrolytes.

Figure 2.4 Illustrations of Zn deposition process, C_o is the concentration of Zn^{2+} cations in the bulk electrolyte, and the C_s the concentration of Zn^{2+} cations at the interface, with the dashed line illustrating the concentration gradient during electrodeposition (gradually decreasing from C_o to C_s). IHL and OHL is the inner and outer Helmholtz layer, respectively.

Figure 2.5 Schematic diagram of Zn^{2+}-intercalation mechanism in γ-MnO_2. Reproduced with permission. Copyright 2015, American Chemical Society.

Figure 2.6 Schematic diagram of the formation of $Zn_4SO_4(OH)_6{\cdot}4H_2O$ (ZHS) at the first discharge process.

Figure 2.7 Issues of electrolytes and interplay with Zn anode, cathode.

Figure 2.8 The contrast of topologies and ion environments between Zn dendrite and its counterparts (Li, Al). (a) SEM image of Li dendrite. (b) SEM observation of Al dendrite. c) SEM image of Zn dendrite prepared by this work. (d–f) Schematic diagrams showing the topologies of dendrites and the related ion environments for Li, Al, and Zn, respectively.

Figure 2.9 Issues associated with aqueous electrolytes and Zn metal anode in aqueous electrolyte. a) Side reactions on Zn anode in aqueous electrolyte; b) stripping resulted holes and newly formed Zn deposits are not at the same positions due to the "hostless" stripping-plating mechanism; c) uneven surface caused dendrite issues; d) concentration polarization caused by slower diffusion compared with redox reaction at the interface, and the resulted dendrites formation. Such concentration polarization gets severer at high current density.

Figure 3.1 (a) SEM image and (b) XRD pattern of β-MnO2 as synthesized.

Figure 3.2 Image capture of binder samples: Ca-SA and Ca-CMC.

Figure 3.3 The components structure of Zn symmetric, half and full cells.

Figure 4.1 Zn|Zn symmetric cells containing 2M $ZnSO_4$ with different amount of MSM at the areal capacity and current density of (a) 1 mAh cm^{-2} at 1 mA cm^{-2}; (b) 5 mAh cm^{-2} at 5 mA cm^{-2}.

Figure 4.2 Zn|Cu half cells performance and properties. (a) Coulombic efficiency of the cells in 2 M $ZnSO_4$ electrolytes with different amount of MSM. The half cells after 50 cycles at 1 mAh cm^{-2} at 1 mA cm^{-2}. SEM images of the Zn foils in (b) 2M and (c) 2MS0.9 electrolytes for half cells after 50 cycles. Charge/discharge voltage profiles of half cells with (d) 2M and (e) 2MS0.9 electrolytes at 1st, 50th and 200th cycles with magnified views of corresponding cycles in the potential range between 0.4 and 0.6 V at a current density of 1 mA cm^{-2}. (f) Cyclic voltammetry at 5 mV s^{-1}.

Figure 4.3 *In-situ* optical microscopic images for Zn deposition process at the current density of 5 mA cm^{-2}.

Figure 4.4 (a) Anodic and (b) cathodic LSV response curves for aqueous $ZnSO_4$ and $ZnSO_4$-MSM electrolyte at 1 mV s^{-1}.

Figure 4.5 Zn|MnO_2 full cells performance. (a) Rate capability at 0.1, 0.2, 0.3, 0.5, 1 A g^{-1} and back to 0.5 A g^{-1}; (b) Galvanostatic Charge Discharge (GCD) profiles at different current density 0.1, 0.2, 0.3, 0.5 and 1 A g^{-1}; and (c) Cycle performance at 0.5 A g^{-1}.

Figure 4.6 Image captures of 1M / 2M $ZnSO_4$ with different amount of MSM.

Figure 4.7 pH value of 2M, 2MS0.5, 2MS0.7 and 2MS0.9 electrolytes.

Figure 4.8 FT-IR spectra of 2 M $ZnSO_4$ electrolytes without and with different amount of MSM at ATR mode. (a) OH stretching (3600 - 3000 cm^{-1}) and (b) S=O, ν (SO_4^{2-}) (1500 - 950 cm^{-1})

Figure 4.9 FTIR spectroscopy for H_2O, H_2O-MSM and MSM.

Figure 4.10 Raman spectra of 2 M $ZnSO_4$ electrolytes without and with different amount of MSM. (a) 500-4000 cm^{-1} (b) 920-1180 cm^{-1} and (c) 3050-3650 cm^{-1}.

Figure 4.11 Contact angle of 2M and 2MS0.9 electrolytes with Zn foil.

Figure 4.12 Comparison of adsorption energy of H_2O and MSM molecules on Zn (002) crystal plane, vertically and parallelly. Inset shows corresponding absorbed model.

Figure 5.1 Zn||Zn plating/stripping and stability. Zn||Zn symmetric cells containing differing concentration of $ZnSO_4$ with same volume percent of additive at current density and areal capacity of a) 1 mA cm^{-2} at 1 mAh cm^{-2}, b) 10 mA cm^{-2} at 10 mAh cm^{-2} and c) 20 mA cm^{-2} at 20 mAh cm^{-2}. d) Cumulative plated capacity *vs.* capacity per cycle of 2MG1 electrolyte compared with selected others.

Figure 5.2 Cycle performance for Zn||Zn symmetric cells using 2M $ZnSO_4$ electrolyte with differing volume percent of GBL at 1 mA cm^{-2} and 1 mAh cm^{-2}.

Figure 5.3 Zn||Cu half-cell performance and properties. a) Coulombic efficiency (CE) for cells in 2M $ZnSO_4$ electrolyte with (2MG1) and without (2M) 1% GBL. b) Time-voltage curves. Charge/discharge voltage profiles of half cell with c) 2M and d) 2MG1 electrolyte at 1st, 50th and 200th cycle with magnified view of corresponding cycles in potential range between 0.4 and 0.6 V at current density 1 mA cm^{-2}. SEM images of Zn-foil in e) 2M and f)

2MG1 electrolyte for half cells following 50 cycles. g) XRD spectra for Zn-foil in 2M and 2MG1 electrolyte for half cells following 50 cycles.

Figure 5.4 Coulombic efficiency for Zn||Cu half cells using 2M $ZnSO_4$ electrolyte with differing volume percent of GBL at 1 mA cm^{-2} and 1 mAh cm^{-2}.

Figure 5.5 Nyquist plots between 2M and 2MG1 electrolytes of the cells before and following 50 cycles.

Figure 5.6 Chemical and physical properties of electrolytes. a) Polarization of corrosion curve, b) Contact angle capure of electrolytes with Zn-foil and c) ^2H NMR spectra for 2M and 2MG1 electrolyte. FT-IR spectra for H_2O, H_2O-GBL, GBL, 2M and 2MG1. d) CH- and OH-stretching, e) ν (SO_4^{2-}). f) Raman spectra for 2M, 2MG1 and GBL. g) 3D snapshot with enlarged area of $ZnSO_4$-GBL and h) RDF and coordination number for Zn^{2+}-O (H_2O) from MD simulations.

Figure 5.7 (a) Anodic and (b) cathodic LSV response curves for aqueous $ZnSO_4$ and $ZnSO_4$-GBL electrolyte at 1 mV s^{-1}.

Figure 5.8 FTIR spectroscopy for H_2O, H_2O-GBL and GBL.

Figure 5.9 3D snapshot for (a) $ZnSO_4$ and (b) $ZnSO_4$-GBL determined from molecular dynamics (MD) simulation.

Figure 5.10 Comparison of coordination number of H_2O molecules for Zn^{2+} *vs.* distance in $ZnSO_4$ and $ZnSO_4$-GBL electrolyte from MD simulation. Inset shows comparison at low value of distance.

Figure 5.11 Theoretical computations for $ZnSO_4$-GBL electrolyte. (a) Binding energy for Zn^{2+} with differing compounds from DFT computation. (b) Electrostatic potential mapping of original Zn^{2+}-6H_2O (Left) and Zn^{2+}-5H_2O-GBL (Right) solvation structures. (c) Comparison of adsorption energy of H_2O and GBL molecules on Zn (002) crystal plane. Inset shows corresponding absorbed model. (d) LUMO and HOMO iso-surface (iso-value = 0.02 a.u.) of H_2O (Right) and GBL (Left) molecules.

Figure 5.12 MSD as a function of time under $ZnSO_4$ and $ZnSO_4$-GBL electrolyte.

Figure 5.13 Comparison of absorption energy for H_2O and GBL on Zn (002) and Zn (101) crystal plane (more possible absorbed sites for GBL in a parallel direction). Insets show corresponding absorbed models.

Figure 5.14 Nucleation overpotential curve for Zn|Zn symmetric cells 2M and 2MG1 $ZnSO_4$ electrolyte.

Figure 5.15 Iso-surface model of charge density difference for ZSC-002 with (a) one H_2O, (b) one GBL in a parallel direction and (c) one GBL vertically (iso-value = 2.5 x 10^{-4} e $Bohr^{-3}$).

Figure 5.16 Iso-surface model of charge density difference for ZSC-101 with (a) one H_2O, (b) one GBL in a parallel direction and (c) one GBL vertically (iso-value = 2.5 x 10^{-4} e $Bohr^{-3}$).

Figure 5.17 2D contours for charge density difference for ZSC-002 with (a) one H_2O, (b) one GBL in a parallel direction and (c) one GBL vertically (iso-value = 2.5 x 10^{-4} e $Bohr^{-3}$).

Figure 5.18 2D contours for charge density difference for ZSC-101 with (a) one H_2O, (b) one GBL in a parallel direction and (c) one GBL vertically (iso-value = 2.5 x 10^{-4} e $Bohr^{-3}$).

Figure 5.19 Schematic mechanism of some reactions between electrolytes and electrode.

Figure 5.20 Ignition test for a pristine glass-fibre separator with saturated GBL, H_2O/GBL solution, 2M $ZnSO_4$ solution (2M) and 2M $ZnSO_4$-GBL solution (2MG1).

Figure 5.21 XRD pattern for β-MnO_2 nano-rod.

Figure 5.22 SEM image of β-MnO_2 nano-rod.

Figure 5.23 Zn||MnO_2 full cell performance. a) Cyclic voltammetry curves for 1st, 2nd and 3rd cycle. b) Rate capability at 0.1, 0.2, 0.3, 0.5, and 1 A g^{-1} and back to 0.5 A g^{-1}. c) Galvanostatic Charge and Discharge (GCD) profiles at current density of 0.1, 0.2, 0.3, 0.5 and 1 A g^{-1} and d) Cycle performance of full cell with 2M and 2MG1 electrolyte.

Figure 5.24 XRD pattern confirms stability of MnO_2 electrodes in $ZnSO_4$-GBL electrolyte before and following 50 cycles in electrolyte at 0.5 A g^{-1}.

Figure 6.1 Zn|Zn symmetric cells containing 2M $ZnSO_4$ with different amount of Pyrrolidone at the areal capacity and current density of (a) 1 mAh cm^{-2} at 1 mA cm^{-2}; (b) 10 mAh cm^{-2} at 10 mA cm^{-2} and (c) 20 mAh cm^{-2} at 20 mA cm^{-2}

Figure 6.2 Zn|Cu half cells performance and properties. (a) Coulombic efficiency of the cells in 2M $ZnSO_4$ electrolytes with different amount of Pyrrolidone. The half cells after 50 cycles at 1 mAh cm^{-2} at 1 mA cm^{-2}. Charge/discharge voltage profiles of half cells with (b) 2M and (c) 2MP3 electrolytes at 1st, 50th and 200th cycles with magnified views of corresponding cycles in the potential range between 0.4 and 0.6 V at a current density of 1 mA cm^{-2}. SEM images of the Zn foils in (d) 2M and (e) 2MP3 electrolytes for half cells after 50 cycles. (f) Cyclic voltammetry at 5 mV s^{-1}.

Figure 6.3 *In-situ* optical microscopic images for Zn deposition process at the current density of 5 mA cm^{-2}.

Figure 6.4 (a) Anodic and (b) cathodic LSV response curves for aqueous $ZnSO_4$ and $ZnSO_4$-Pyrrolidone electrolyte at 1 mV s^{-1}.

Figure 6.5 Zn|MnO_2 full cells performance. (a) Rate capability at 0.1, 0.2, 0.3, 0.5, 1 A g^{-1} and back to 0.5 A g^{-1}; (b) Galvanostatic Charge Discharge (GCD) profiles at different current density 0.1, 0.2, 0.3, 0.5 and 1 A g^{-1}; and (d) Cycle performance at 0.5 A g^{-1}.

Figure 6.6 FT-IR spectra of 2M $ZnSO_4$ electrolytes without and with different volume of Pyrrolidone at ATR mode. (a) OH stretching (3600 - 3000 cm^{-1}) and (b) S=O, ν (SO_4^{2-}) (1500 - 950 cm^{-1})

Figure 6.7 Raman spectra of 2M $ZnSO_4$ electrolytes without and with different volume of Pyrrolidone. (a) 500-4000 cm^{-1} (b) 920-1180 cm^{-1} and (c) 3050-3650 cm^{-1}.

Figure 6.8 Contact angle 2M and 2MP3 electrolytes with Zn foil.

Figure 7.1 Schematic of the strategies toward aqueous electrolytes for AZIBs.

Table 1.1. Comparison of monovalent and multivalent metal electrodes.

Table 2.1 Properties of several aqueous Zn^{2+} electrolytes.

Table 4.1 Boiling point, flash point and solubility (25 °C) of selected rganic additives in electrolyte of AZIBs.

Table 4.2 Comparison of accumulative plated capacity with current density of selected organic additives in electrolyte of AZIBs.

Table 5.1 Boiling point, flash point and solubility (25 °C) of selected rganic additives in electrolyte of AZIBs.

Table 5.2 Comparison of accumulative plated capacity with current density of selected organic additives in electrolyte of AZIBs.

Table 5.3 Comparison of Coulombic efficiency (CE) and cumulaltive plated capacity for Zn half cells with selected organic additives in electrolyte of AZIBs.

Table 6.1 Boiling point, flash point and solubility (25 °C) of selected rganic additives in electrolyte of AZIBs.

Table 6.2 Comparison of accumulative plated capacity with current density of selected organic additives in electrolyte of AZIBs.

Abbreviation	Full name
2D	Two-dimensional
3D	Three-dimensional
ACN	Average coordination number
AM	Acrylamide
AN	Acetonitrile
ATR	Attenuated total reflection
AZIB	Aqueous zinc-ion battery
BIS-TRIS	2-Bis(2-hydroxyethyl) amino-2-(hydroxymethyl)-1,3-propanediol
CCC	Campus Crusade for Christ
CDD	Charge density difference
CE	Coulombic efficiency
CV	Cyclic voltammetry
D_{Zn}^{2+}	Zn^{2+} diffusion coefficient
D_2O	Deuterium oxide
DFT	Density functional theory
DME	1,2-dimethoxyethane
DMF	N, N-Dimethylformamide
DMSO	Dimethyl sulfoxide
EEI	Electrolyte electrode interface
EIS	Electrochemical impedance spectroscopy
ESP	Electrostatic potential
Et	Erythritol
Et_2O	ethyl ether
EC	Ethyl carbonate
EMC	Ethyl methyl carbonate

EG	Ethylene glycol
FE-SEM	Field emission scanning electron microscopy
FTIR	Flourier transformed infrared spectroscopy
g	gram
GBL	Gamma-Butyrolactone or 1,4-Butyrolactone
GCD	Galvanostatic charge-discharge
GITT	Galvanostatic intermittent titration technique
GROMACS	Groningen Machine for Chemical Simulations
h	hour
HOMO	Highest occupied molecular orbital
ICE	Initial Coulombic efficiency
JCPDS	Joint Committee on Powder Diffraction Standards
KIB	Potassium-ion battery
LIB	Lithium-ion battery
Li^+	Lithium ions
LUMO	Lowest unoccupied molecular orbital
M	Metal element
µm	Micrometer
mA	Milliampere
mg	Milligram
MD	Molecular dynamics
Me3EtNOTF	trimethylethyl ammonium trifluoromethanesulfonate
MSD	Mean-squared displacement (MSD)
MSIT	Ministry of Science and ICT
MSM	Methyl sulfone
Na2EDTA	Ethylenediaminetetraacetic acid disodium salt
nm	Nanometer
ns	Nanosecond
NOP	Nucleation overpotential
NRF	National Research Foundation
NPT	constant-pressure, constant-temperature
OPL	Organic protection layer
OPLS	Orthogonal projections to latent structures
$P_{444(2O1)}$-TFSI	tributyl(2-methoxyethyl)-TFSI
PAM	polyacrylamide
PAW	Projector augmented wave
PBE	Perdew-Burke-Ernzerhof
PC	Propylene carbonate
PPG	Potential platform gap
ps	Picosecond
PTFE	Poly(tetrafluoroethylene)
PVDF	Polyvinylidene fluoride
Raman	Raman spectroscopy
RDFs	Radial distribution functions

Sac	Saccharin
SDBS	sodium dodecyl benzene sulfonate
SEI	Solid electrolyte interphase
SEM	Scanning electron microcopy
SFC	Student for Christ
SHE	Standard hydrogen electrode
SIB	Sodium-ion battery
SL	Sulfolane
SN	Succinonitrile
SPC	Simple point charge
SUES	Shanghai University of Engineering Science
T	Thermodynamic temperature
TBA_2SO_4	tetrabutylammonium sulfate
TC	triethylmethylammonium chloride
TEP	triethyl phosphate
TFEP	tris(2,2,2-trifluoroethyl) phosphate
TMP	trimethyl phosphate
TSP	Trimethylsilyl propanoic acid
UOU	University of Ulsan
VASP	Vienna ab-initio simulation package
XRD	X-ray diffraction
Zn^{2+}	Zinc ions
ZSC	Zinc stacked cube
ΔG	Wetting free energy
θ_A	Contact angle
(h k l)	Miller indices

CHAPTER 1 Introduction

1.1 Research background

To greatly improve the ecological environment and achieve the target of carbon neutrality around 2050s, it is significant to develop a kind of low-cost convenient-eco-friendly-green and assemble-disassemble-recyclable next-generation energy system. It is urgent to develop an electrical energy storage system which could achieve discharge-charge quickly and effective long life-span of advanced all-size devices and electrics, including the flexible smart equipment.[1] (Figure 1.1)

Figure 1.1 Icon collections of electric tools and equipment from the portable flashlight to the rocket, even Metaverse.

Nowadays, lithium-ion battery (LIB) is the most advanced secondary battery, which occupies a dominant position in the portable electronic product market. Unfortunately, the increasing attention to its security and high cost limit its further development. In addition, waste lithium-ion batteries containing flammable organic electrolytes and toxic elements

cause another huge environmental problem. Therefore, it is urgent to find safe, cheap and environmental benignity alternatives to LIBS. Aqueous secondary battery has great application potential in the field of large-scale energy storage because of its inherent rich resources, safety, low cost, large capacity and environmental friendliness, which has triggered an unstoppable literature upsurge. Among them, aqueous rechargeable zinc batteries have been considered as a promising candidate for large-scale energy storage due to the low cost, intrinsic safety, low toxicity, high energy density with high power density (Figure 1.2) and the unique features of zinc: good conductivity (5.91 μΩ), low redox potential (-0.7626 V vs. standard hydrogen electrode, in acidic solution, 298.15 K), high abundance (300 times higher than lithium), high gravimetric capacity (821 mAh g^{-1}) and high volumetric capacity (5855 Ah L^{-1} compared to 2061 Ah L^{-1} for Li anode), as well as the good insensitivity in oxygen and humid atmosphere, which broadens the availability of electrolytes. Zn^{2+} has a relatively small ionic radius (0.75 Å) and the size of hydrated Zn^{2+} is also comparable with hydrated Li^{+}, which is beneficial for the intercalation/deintercalation of divalent Zn^{2+} ions into/from the crystal structures of cathode materials. (Table 1.1).[1]

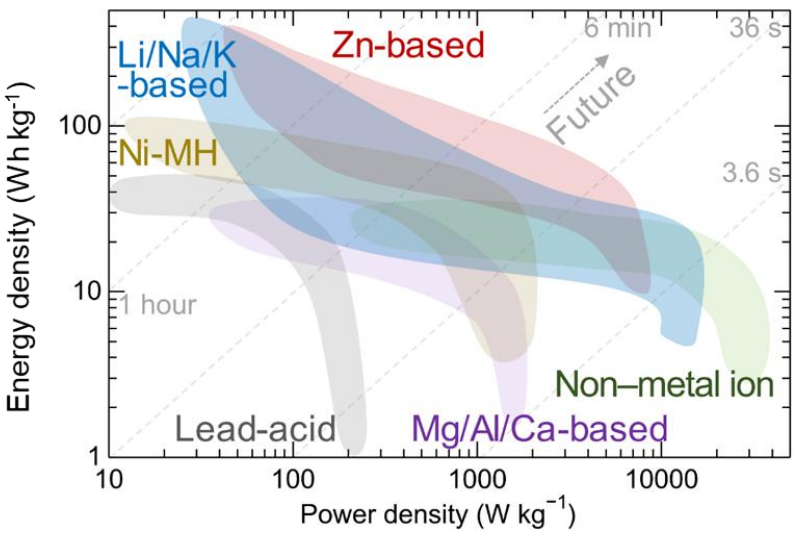

Figure 1.2 Ragone plot of some conventional commercialized batteries, typical metal ions (including Li^{+}, Na^{+}, K^{+}, Zn^{2+}, Mg^{2+}, Al^{2+}, and Ca^{2+}), and non–metal ion charge carrier-based ABs.[1]

Table 1.1. Comparison of monovalent and multivalent metal electrodes.

Metal electrode	Ionic radius (Å)	Hydrated ion radius (Å)	Specific gravimetric capacity (mA h g^{-1})	Specific volumetric capacity (mA h cm^{-3})	Potential vs SHE (V)	Element abundance in the Earth's crust (%)
Li	0.76	-3.40-3.82	3860	2061	-3.04	0.0017
Na	1.02	2.76-3.60	1166	1129	-2.71	2.3
K	1.38	2.01-3.31	685	610	-2.92	1.7
Mg	0.72	3.00-4.70	2206	3834	-2.36	2.9
Ca	1.00	4.12-4.20	1337	2072	-2.84	5.0
Zn	0.75	4.12-4.30	821	5855	-0.76	0.0079
Al	0.53	4.80	2980	8046	-1.68	8.2

As a key component, the electrolyte provides a basic working environment, determining the electrochemically stability potential window (ESPW), affecting Zn^{2+} storage coulombic efficiencies and storage behaviors, etc. Due to the characteristics and formation mechanism of organic-functional modified (electrolyte electrode interface) EEI, it can solve or alleviate the problems such as anode dendrite, corrosion, electrolyte decomposition (HER and OER), dissolution, and structural collapse, etc. Considering the availability, cost and conductivity of different kinds of salt electrolytes and simple or complexity producing process, we choose mild zinc sulfate as the base electrolyte for AZIBs. (Figure 1.3)

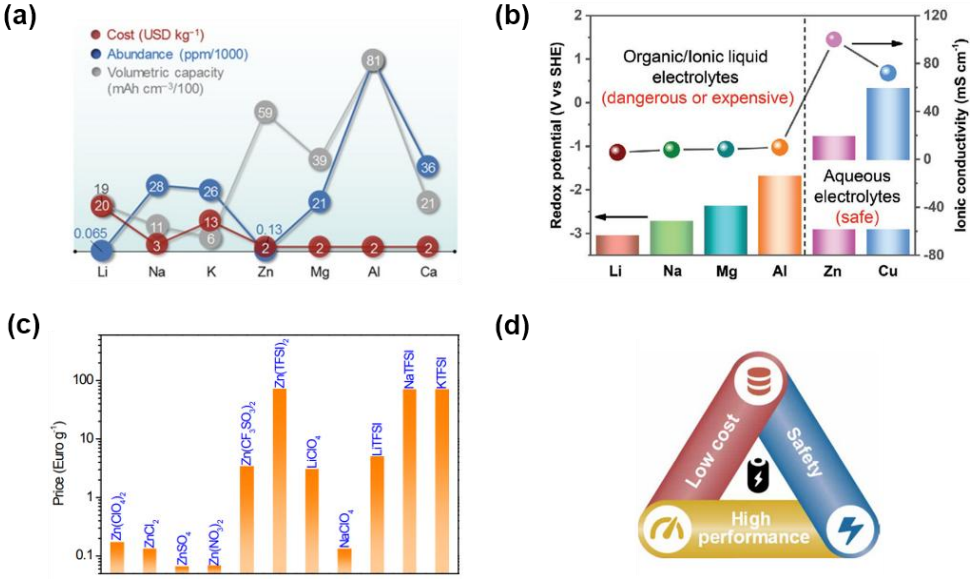

Figure 1.3 (a) Comparison of cost, abundance, and volumetric capacity of metal anodes. [1] (b) Comparison between Zn and other metal anodes in terms of redox potential and ionic conductivity.[2] Copyright 2020, John Wiley and Sons. (c) Price comparison of commonly-used salts in different batteries. The price is calculated based on the available largest pack size from Sigma.[3] Copyright 2021, Royal Society of Chemistry. (d) The three criteria for the future road to commercialization of AZIBs.[1]

1.2 Objectives of the research

As mentioned above, aqueous zinc batteries with mild electrolytes (e.g., 2 M $ZnSO_4$) as reaction media have attracted a lot of research work in the past decade. However, the study of cathode active materials and their zinc ion storage mechanism accounts for a great part. Until recently, zinc metal anode has gradually begun to receive due attention. Due to the dendrite growth and side reactions (including zinc electrode corrosion and hydrogen evolution reaction), zinc anode continues to have low Coulomb efficiency and limited reversibility in mild electrolyte. The poor performance of zinc electrode seriously restricts the effective development of aqueous Zn-ion batteries. Therefore, the purpose of this study is to find the effective method to inhibit zinc dendrites and side reactions to develop the advanced zinc

metal electrodes. In this doctoral thesis, the interfacial chemistry of zinc metal electrode in 2 M $ZnSO_4$ solution electrolyte with and without additives was studied, which shows that the growth of zinc dendrite is the main potential factor leading to battery short-circuit fault. At the same time, the freshly polished zinc metal is highly unstable in 2M $ZnSO_4$ electrolyte, which is easy to form a loose and discontinuous overall disordered structure of hydroxyl zinc sulfate hydrate structure. Moreover, there is no buffer layer between zinc ions and zinc electrode, which cannot block the active water to protect the zinc electrode. At the same time, hydrogen is generated, and the battery volume is easy to expand. In order to solve the problems of zinc electrode, different strategies have been proposed to solve various problems, including the introduction of electrolyte additives and the construction of artificial or in-situ SEI layer, so as to effectively improve the performance of zinc metal electrode.

1.3 Thesis structure

The structure of this thesis work is briefly outlined as follows

Chapter 1 introduces the background for aqueous batteries and the background for the Zn-ion batteries with electrolyte.

Chapter 2 presents a literature review on principals of AZIBs (reaction of water molecules, Zn-MnO_2 reactions and Zn deposition process), electrolyte, as well as the issues of aqueous Zn-ion batteries.

Chapter 3 illustrates the general experimental procedures including functional zinc sulfate electrolyte preparation, the synthesis method of cathode material MnO_2, physical characterization methods, the electrochemical measurements and the model settings of theoretical calculations.

Chapter 4 introduces the electrolyte additive methyl sulfone effects on the Zn metal electrode in aqueous Zn-ion batteries.

Chapter 5 introduces the adsorption and binding effect on Zn electrode surface towards the dendrite-free and side reaction-free Zn anode for advanced aqueous Zn-ion batteries.

Chapter 6 introduces the electrolyte additive pyrrolidone effects on the Zn metal electrode in aqueous Zn-ion batteries.

Chapter 7 summarizes the work in this thesis and provide some prospects for the development of high current density and capacity, coupling with Mn-based cathodes, aiming for more stable, higher rate, longer cycle life, wider potential range, wider temperature range (-30 - 60°C) and high-power density AZIBs

References

[1] D. Chao, W. Zhou, F. Xie, C. Ye, H. Li, M. Jaroniec, S-Z. Qiao. Sci. Adv. 2020, 6, eaba4098.

[2] Q. Yang, Q. Li, Z. Liu, D. Wang, Y. Guo, X. Li, Y. Tang, H. Li, B. Dong, and C. Zhi. Adv Mater. 2020, 32, 2001854

[3] Y. Zhu, J. Yin, X. Zheng, A-H. Emwas, Y. Lei, O. F. Mohammed, Y. Cui and H. N. Alshareef. Energy Environ. Sci., 2021, 14, 4463.

CHAPTER 2 Literature Review

2.1 Introduction

Aqueous Zinc-ion batteries (AZIBs) characterize high safety index, low-cost, benign to develop and promising electrochemical storage property, thus are considered as a potential energy storage method to be applied in large-scale energy storage devices. However, AZIBs still face various pressing challenges and dilemmas. The electrolyte is an essential part in the AZIBs. The mechanisms, equilibrium of ions reflux, reaction kinetics, and the sides reactions of AZIBs would be affected by the modulation of electrolyte systems to a great extent. The electrolytes and electrolyte additives in AZIBs could be summarized and classified into different sorts of systems. As to the liquid phase (Figure 2.1), the electrolyte systems were categorized into aqueous (alkaline, neutral or mild acid, gel) and organic systems which containing KOH, $ZnSO_4$, $Zn(CF_3SO_4)_2$, $Zn(TFSI)_2$ based on different mechanisms such as in-stable $Zn(OH)_4^{2-}$ complex ions, half-hexagon dendritic seed, special solvent sheath, interfacial ion flux mediation and solid electrolyte interface (SEI), etc.

Another way of classification is according to the solubility or the formation method of additives (Figure 2.2), the electrolyte systems were categorized into soluble (in H_2O), hydrated or deep eutectic solvent (HES or DES), miscible and immiscible (with H_2O) based on different mechanisms such as the absorption of Zn surface, modulation of solvation sheath structure (including anion-coordinated, organic-coordinated, and etc.), organic-H_2O-hydrogen bonding network, in-situ formation of SEI and phase separation, etc.

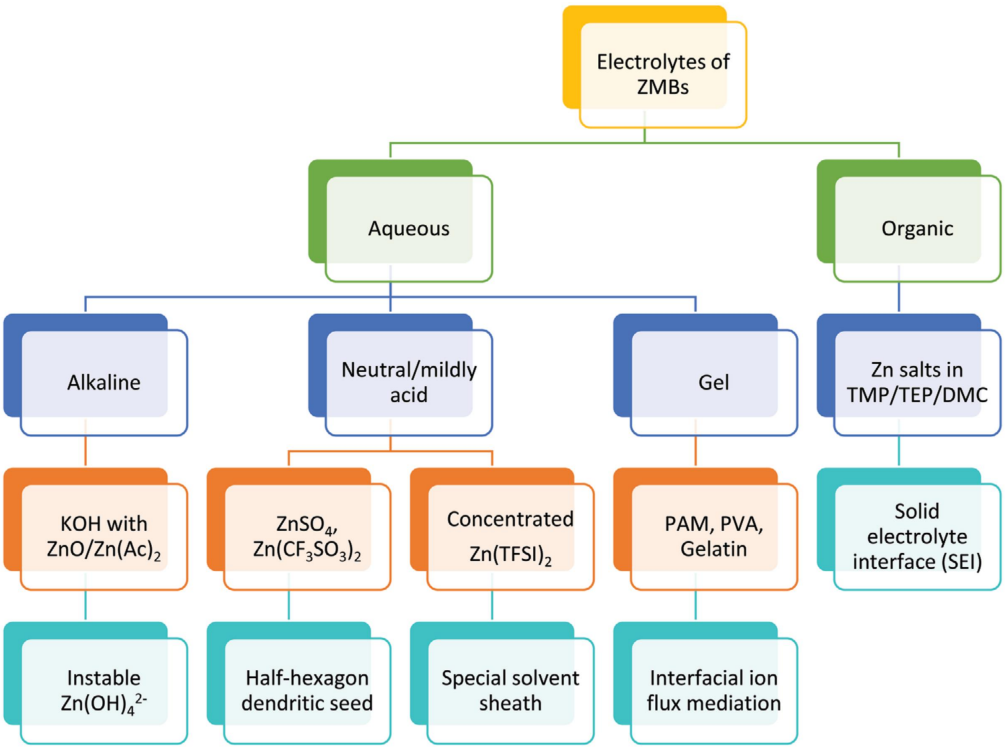

Figure 2.1 Summary and classification of the as-developed electrolyte systems of AZIBs with distinct compositions and features related to the dendrite issue of the Zn anode. Reproduced with permission.[1] Copyright 2020, John Wiley and Sons.

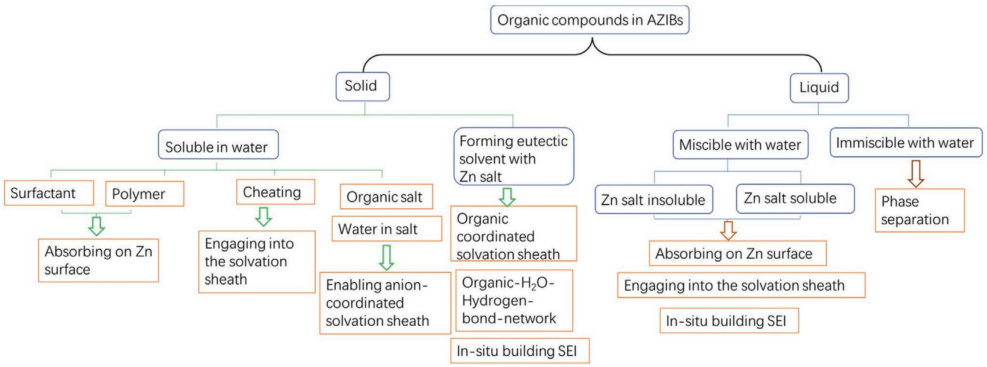

Figure 2.2 Summary and classification on the solubility, mechanism role of the organic compounds used in AZIBs. Reproduced with permission.[2] Copyright 2022, John Wiley and Sons.

2.2 Principals of Aqueous Zinc Ion Batteries

2.2.1 Reactions of Water Molecules

In the aqueous zinc ion batteries, water is of some helpful and unavoidable part which not only ensures the safety and unique features for the aqueous electrolytes but also determine the environment stability or exactly, the electrochemical stability of window (ESW). It should be highly noteworthy that water molecules in aqueous would be liable to electro-reduced (H_2 evolution reaction HER, Equation (3)) or electro-oxidized (O_2 evolution reaction OER, Equation (5)) at the anode or cathode thermodynamically, which could bring out the low and unstable Coulombic efficiency, unreversible anode and low operating voltage of AZIBs. [3]

$$2H_2O + 2e^- \rightarrow H_2 + 2OH^- \tag{3}$$

$$E_{H_2O/H_2} = E^{\Theta}_{H_2O/H_2} + \frac{RT}{2F}\text{In}\left(\frac{\alpha^2_{H_2O}}{\alpha^2_{OH^-} P_{H_2}/P_0}\right)$$
$$= E^{\Theta}_{H_2O/H_2} + 2.303\frac{RT}{F}[\log(\alpha_{H_2O}) + 14 - \text{pH}] \tag{4}$$

$$H_2O - 2e \rightarrow \frac{1}{2}O_2 + 2H^+ \tag{5}$$

$$E_{H_2O/O_2} = E^{\Theta}_{H_2O/O_2} + \frac{RT}{2F}\text{In}\left(\frac{\alpha^2_{H^+}(P_{O_2}/P_0)^{1/2}}{\alpha_{H_2O}}\right)$$
$$= E^{\Theta}_{H_2O/O_2} - 2.303\frac{RT}{F}\left[\frac{1}{2}\log_{10}(\alpha_{H_2O}) + pH\right] \tag{6}$$

and the potential difference (ΔE) between OER and HER would be defined as following.

$$\Delta E = E^{\Theta}_{H_2O/O_2} - E^{\Theta}_{H_2O/H_2} - 2.303 \times 14 \times \frac{RT}{F} - 2.303\frac{RT}{F}\left[\frac{3}{2}\log_{10}(\alpha_{H_2O})\right] \quad (7)$$

In the Equations (4, 6, 7), E^{Θ} is the standard potential and E is the potential in different conditions, α means the activity and for pure water α is 1. P_{H2} / P_0 and P_{O2} / P_0 are the partial pressure of hydrogen and oxygen gas and normally is 1 at the standard atmosphere. Besides, F, R and T are standard for the Faraday constant, thermodynamic constant and temperature, respectively.

Ideally, the activity of water molecules (α_{H_2O}) is 1, then the potential of HER and OER is in a linear relationship with the pH value, as displayed in the Pourbaix diagram (Figure 2.3a), while the overall ESW of aqueous electrolyte keeps unchanged, irrelevant to the pH value and the dependence of the ESW on the water activity can be revealed by Equation (7). Meanwhile, the ESW is governed by the activity of water molecules in the corresponding aqueous electrolyte, with the reduced activity of water molecules, the two potentials could be shifted upward and downward for OER and HER, expanding the ESW. [4]

To understand the fundamental mechanism of According to the Pourbaix diagram of Zn with H_2O (Figure 2.3), the working environment of aqueous media is thermodynamically unstable with different potential range in the pH value, which would change in real time. Moreover, Zn is thermodynamically unstable and the redox potential for hydrogen evolution reaction (HER) is climbing with a reducing pH of the electrolyte, which the potential tendency line of oxygen evolution reaction (OER) is parallel and linear to the HER, the equilibrium balance. As for the acidic conditions (pH < 4.0), Zn would be more soluble and to be favorably transformed into Zn^{2+} ions during the cathodic process. As for the mild conditions (5.0 < pH < 8.0), the dissolution of Zn would become the solvation sheath structure $Zn(H_2O)_6^{2+}$ in the electrolyte, which conforms a high energy barrier. This conformation distinctly gives rise to the charge transfer resistance.

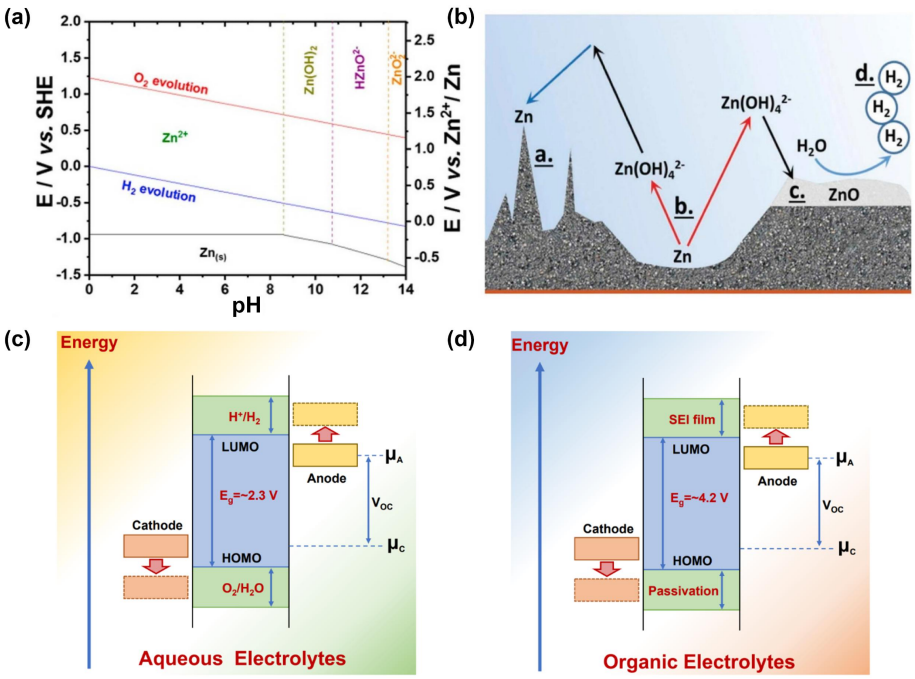

Figure 2.3 (a) Pourbaix diagram of Zn-H_2O system at 25 °C. Reproduced with permission.[3] Copyright 2020, Elsevier. (b) Schematic illustration of four major issues that may occur on the zinc electrode: insert label (a) dendrite growth, (b) shape change, (c) passivation, and (d) hydrogen evolution. Reproduced with permission.[3] Copyright 2020, Elsevier. (c-d) Schematic open-circuit energy diagram of (c) aqueous and (d) organic electrolytes. Reproduced with permission.[5] Copyright 2020, Royal Society of Chemistry.

Moreover, if the shell-layered H_2O molecules near the zinc anode surface occurs easily to form H_2 and OH^- in the charging process, the dissolution of Zn would become relatively slower due to the high overpotential and the lower corrosion activity compared with strong acid solution. As for the alkaline conditions (8.0 < pH < 10.5), the dissolution of Zn decreases could force the presence of $Zn(OH)_2$, which would subsequently transfers into the passivated electrochemically ZnO precipitates, thus increasing significantly the interface resistance and failing the battery property such as Coulombic efficiency. Additionally, the dissolution of Zn decreases and more stable Zn corrosion products would be generated (e.g., $Zn(OH)_2$). Furthermore, as for the alkaline environment (pH > 11), Zn solubility increases again, which the oxygen reduction reaction (OER) dominates the cathodic corrosion process. Different

from the electrochemical behaviors in neutral or mildly acidic solutions, the zinc electrodes undergo a solid-solute-solid transformation in alkaline electrolytes (ZnO-$Zn(OH)_4^{2-}$-Zn), which inherently faces four major performance-liming phenomenon, which occur during battery operations:

(i) the non-uniform dissolution and deposition of zinc would occur at random locations of electrode surface, leading to severe electrode morphology change and dendrite growth after continuous cycling.

(ii) the discharge product ZnO passivates on the surface of Zn, which lowers the utilization of zinc active materials and increase the internal resistance.

The anodic reaction in alkaline media is expressed by the following equations:

$$Zn(s) \rightarrow Zn^{2+}(aq) + 2e^- \quad (8)$$

$$Zn^{2+}(aq) + 4OH^-(aq) \rightarrow Zn(OH)_4^{2-}(aq) \quad (9)$$

$$Zn(OH)_4^{2-}(aq) \rightarrow ZnO(s) + 2\,OH^-(aq) + H_2O(l) \quad (10)$$

Therefore, strategies to increase the overpotential and decrease exchange current density for hydrogen evolution should be developed to improve the charging efficiency and reduce the self-discharge rate of the zinc electrode.[6].

2.2.2 Zn deposition process

Addition to the reaction of H_2O and Zn with H_2O molecules, another phenomenon is also very important which is the process of Zn deposition during the electrochemical transportation. The process of electrochemical Zn deposition from an electrolyte to the electrode is shown in Figure 2.4.

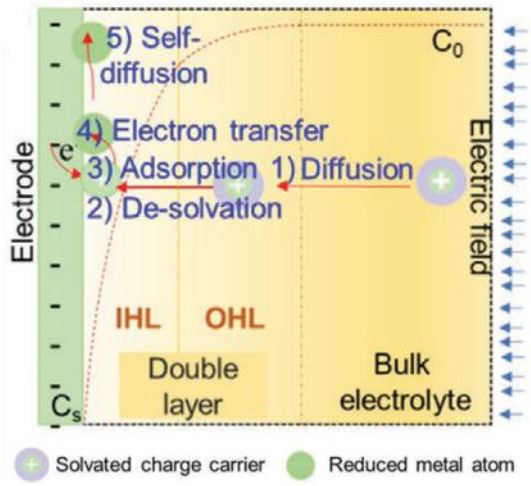

Figure 2.4 Illustrations of Zn deposition process, C_o is the concentration of Zn^{2+} cations in the bulk electrolyte, and the C_s the concentration of Zn^{2+} cations at the interface, with the dashed line illustrating the concentration gradient during electrodeposition (gradually decreasing from C_o to C_s). IHL and OHL is the inner and outer Helmholtz layer, respectively. Reproduced with permission.[2] Copyright 2022, John Wiley and Sons.

First, under the action of electric field and the contact of electrolyte and electrode, the solvated cations (charge carrier) of bulk electrolyte (C_0 initial high concentration) become thermodynamically mobile diffusion toward another side (C_s low concentration). In another words, along with the electrode, Zn^{2+} would be electro-reduced and quickly depleted at the interface, and results in a concentration dilution arc that gradually decreases from C_o in the bulk electrolyte to C_s at the interface.[7]

The molecules and ions in the electrolyte (take zinc sulfate as an example, such as H_2O, Zn^{2+}, SO_4^{2-}, OH^- and etc.) would impact on the electrode surface due to the thermal motion and the pressure from liquid phase. Meanwhile, during the collision or impact, the electrons would be transferred between solid and liquid atoms due to the overlapping of the electron clouds of atoms, and ionization reactions may also occur. Thus, electrons and ions would be generated simultaneously on the surface, the charge carriers would be attracted by electrostatic interactions and to form electric double layer. [8]

Secondly, the ions would deep through the electric double layer, gradually evolve into de-solvated states in the inner Helmholtz layer (IHL).

Thirdly, the de-solvated Zn^{2+} cations would absorb onto the surface of Zn electrode, and simultaneously, the electrons would transfer from the electrode to the absorbed Zn^{2+}, which would be reduced to Zn metal, along with the self-diffusion.[2] Mass transport refers to the diffusion of charge carriers and the charge transfer process contains the de-solvation, absorption, and the spontaneous electron transfer.

2.2.3 Zinc Manganese-Based Reactions

Manganese-based oxides, because of their low cost, low toxicity and their relatively high reduction potentials, have received widespread attention since the 1990s in the field of electrochemical energy storage, such as supercapacitors, pseudo capacitors, primary batteries, rechargeable metal-air batteries, and Li-ion batteries (LIBs) [9–12].

Generally, the batteries that consist of an aqueous Zn^{2+}-containing electrolyte, a cathode for hosting Zn^{2+} and a zinc anode are called aqueous zinc-ion batteries (AZIBs), which have attracted particular interests in the recent years [13]. Especially, as the development of the aqueous zinc ion batteries, it becoming hot-topic about manganese oxide (MnO_2) based cathode coupled with Zn anode.

Seven kinds of manganese oxide were categorized by the different crystal phases and atomic architectures, such as including α-MnO_2 (2 × 2 tunnels) [14–19], β-MnO_2 (1 × 1 tunnels) [20–22], γ- or ε-MnO_2 (1 × 1 and 1 × 2 tunnels) [23–26], todorokite (3 × 3 tunnels) [27], δ-MnO_2 (layered structure) [28, 29], R-MnO_2 and other Mn oxides with different oxidation states such as Mn_2O_3 [30, 31], Mn_3O_4 [32, 33], and $ZnMn_2O_4$ [34] due to the different two-dimensional (2D) layered or tunnel-type structure. [35]

Charge:

$$2MnO_2 + Zn^{2+} + 2e^- \rightarrow ZnMn_2O_4 \quad (11)$$

$$MnO_2 + xZn^{2+} + 2xe^- \rightarrow Zn_xMnO_2 \quad (12)$$

$$2Zn_{0.5}MnO_2 + 2H_2O \rightarrow Zn^{2+} + Mn^{2+} + MnO_2 + 4OH^- \quad (13)$$

$$4Zn^{2+} + 6OH^- + SO_4^{2-} + 5H_2O \rightarrow Zn_4(OH)_6(SO_4)\cdot 5H_2O \quad (14)$$

Discharge:

$$Zn_xMnO_2 \rightarrow MnO_2 + xZn^{2+} + 2xe^- \quad (15)$$

$$ZnMn_2O_4 + Mn^{2+} + 6H_2O \rightarrow ZnMn_3O_7\cdot 3H_2O + 6H^+ + 4e^- \quad (16)$$

$$Zn_4(OH)_6(SO_4)\cdot 5H_2O + 6H^+ \rightarrow 4Zn^{2+} + SO_4^{2-} + 11H_2O \quad (17)$$

$$Mn^{2+} + 2H_2O \rightarrow MnO_2 + 4H + 2e^- \quad (18)$$

So far, different kinds of transition metal oxides and compounds with a two-dimensional (2D) layered structure or tunnel-type structure that enable the reversible insertion/extraction of Zn^{2+} into/out of the lattice have been investigated. Manganese (Mn) -based cathodes usually would suffer from irreversible phase changes, structural collapse, and the Jahn–Teller effect inducing Mn^{2+} dissolution, resulting in rapid fading of capacity and undesirable cyclability and stability.[36] To adjust lattice distance, form tunnels, and layered configurations by choosing different bonding element, researchers also developed $Na_2Mn_3O_7$, $ZnMn_2O_4$, Ca_2MnO_4, $MgMn_2O_4$, and other Mn-based materials as cathode materials for ZIBs.[36]

For example, by using in situ X-ray absorption near edge structure (XANES) and in situ synchrotron X-ray diffraction (XRD) techniques, Kim and co-workers elucidated that intercalation-deintercalation mechanism of Zn^{2+} into/out of the orthorhombic tunnel-type γ-$Mn^{4+}O_2$ (Figure 2.5) [37]. During the discharge process (corresponding to Zn^{2+}

intercalation), the initial tunnel-type γ-MnO_2 phase is successively transformed to spinel-type $ZnMn^{3+}{}_2O_4$, tunnel-type γ-$Zn_xMn^{2+}O_2$, and layered-type L-$Zn_yMn^{2+}O_2$, which is accompanied by the reduction of MnO_2 from Mn^{4+} to the Mn^{3+} and Mn^{2+}, respectively. Upon charging (as Zn^{2+} deintercalation), these Zn-intercalated manganese phases gradually revert back to the original state of γ-$Mn^{4+}O_2$, revealing a reversible Zn^{2+} insertion/extraction mechanism for γ-$Mn^{4+}O_2$. For example, there are several equations of stages, including Hetaerolite formation (Equation 11), Zn^{2+} insertion (Equation 12), Disproportionation (Equation 13), ZHS formation (Equation 14), Deintercalation of Zn^{2+} (Equation 15), Chalcophanite formation (Equation 16), ZHS dissolution (Equation 17) and H^+/Zn^{2+} co-insertion mechanism [38]. It is obviously that most manganese-based cathodes including δ-MnO_2 exhibited two obvious discharge platform stages (e.g., 1.1-1.3 V and 1.35-1.4 V vs Zn^{2+}/Zn) in $ZnSO_4$-based or Zn $(CF_3SO_3)_2$-based aqueous electrolyte. [38-41] In the ionic liquid electrolyte, the manganese-based cathodes such as spinel LiMn2O4 show a low capacity which is far less than that in the aqueous electrolyte. [40, 42]

Some literature reported that H^+ insertion would form MnOOH during discharge may occur simultaneously [43], or sequentially [44] with Zn^{2+} insertion. Some studies have suggested that the formation of MnOOH occurs first and is followed by dissolution of highly soluble Mn^{2+} by electrochemical reduction (Equation 19) [45] or chemical disproportionation (Equation 20) and that there is no Zn^{2+} insertion. On the other hand, it has been reported that Mn^{4+} in MnO_2 is reduced to Mn^{3+} upon electrochemical intercalation of Zn^{2+} and the resulting Mn^{3+} compound is disproportionated into Mn^{4+} and Mn^{2+} (Equation 21) [46]. The purpose of this study is to investigate the mechanisms associated with the use of electrolyte manganese oxide as the positive electrode in aqueous ZIBs. Cycled batteries are disassembled to characterize the electrolyte manganese oxide electrodes at different potential stages using X-ray powder diffraction (XRD), scanning electron microscopy (SEM) and transmission/scanning transmission electron microscopy (TEM/STEM). The results are compared with and supported by electrochemical measurements, including galvanostatic charge–discharge and rotating ring-disk electrode tests. Briefly, there is reversible Zn^{2+}

intercalation into the tunnels of γ-/ε-MnO_2 (in electrolyte manganese oxide) in addition to dissolution/precipitation side reactions.

$$MnOOH + H_2O + e^- \rightarrow Mn^{2+} + 3OH^- \quad (19)$$

$$2MnOOH \rightarrow Mn^{2+} + MnO_2 + 2OH^- \quad (20)$$

$$2Zn_{0.5}MnO_2 + 2H_2O \rightarrow Zn^{2+} + Mn^{2+} + MnO_2 + 4OH^- \quad (21)$$

Continuously dissolved Mn^{2+} ions can account for nearly 1/3 of the total amount of manganese in a cathode, leaving abundant manganese vacancy sites in the electrode.[47] Even worse, the original structure of the host materials would be destroyed, resulting in significant capacity fading. A typical example is Mn dissolution resulted by the classic Jahn-Teller effect. The manganese oxygen octahedron deforms, and the trivalent manganese is prone to disproportionation reaction to generate divalent manganese ions, which will cause interface dissolution, and gradually cause the internal structure of the material to collapse. [48] Secondly, Cathode crystal structure collapse will result in the instability. On the one hand, material dissolution may cause structural collapse; on the other band, divalent zinc ions have a strong binding force with the host structure, which is easy to cause structural damage and material shedding [49]; Thirdly, stress can also cause cathode instability [50]. the continuous insertion and extraction of ions causes the expansion and contraction of the cathode material, which eventually leads to the presence of the electrode material stress, which leads to capacity decay. These undesirable issues can be effectively alleviated by electrolyte modulation. It has been reported that the addition of Mn^{2+} into an electrolyte is a useful strategy to balance the equilibrium between the dissolution and recombination of active materials, and therefore improve the electrochemical performance of manganese-based materials.[51], of which the corresponding dissolution/oxidation reaction equation is shown in Equation (19).

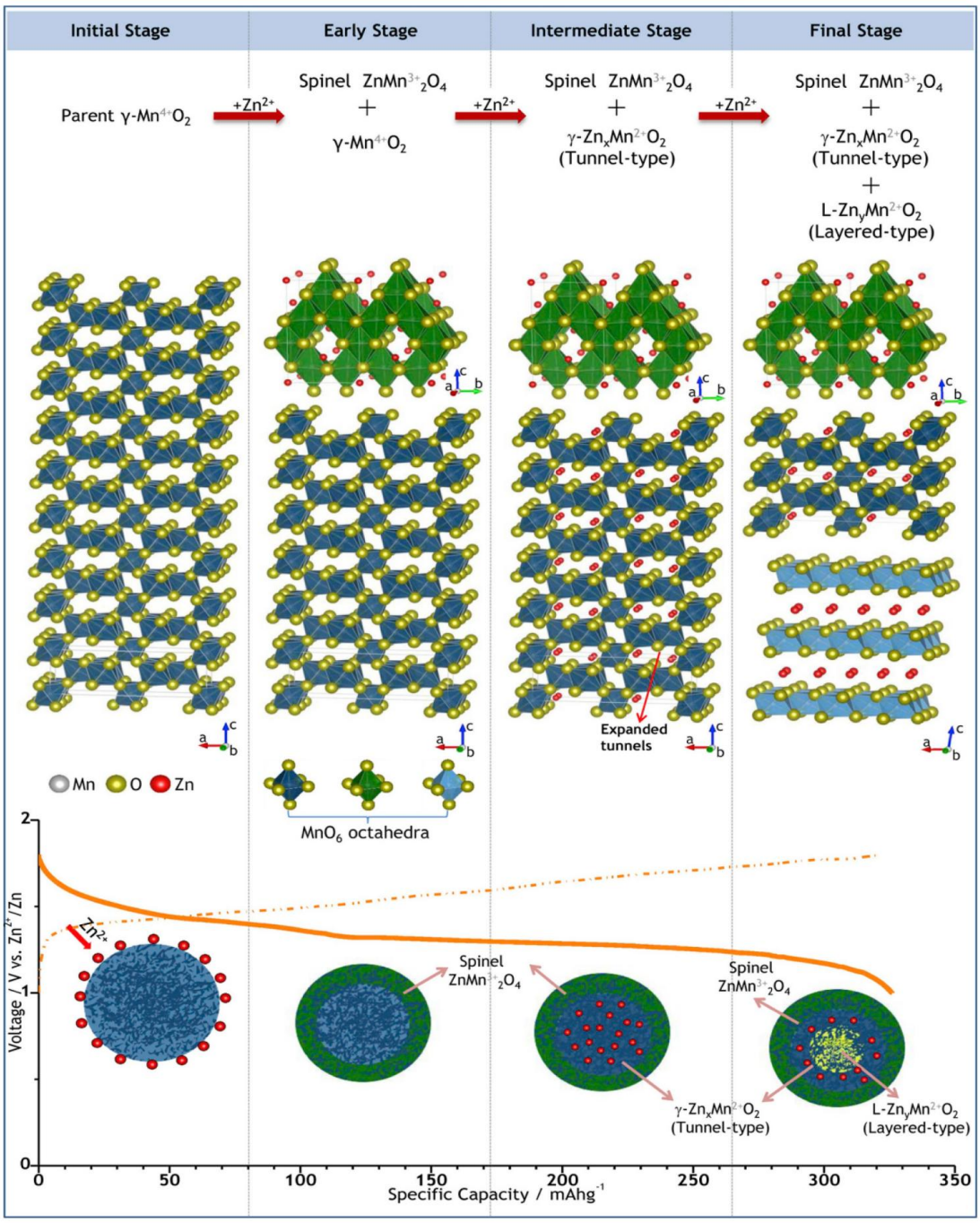

Figure 2.5 Schematic diagram of Zn^{2+}-intercalation mechanism in γ-MnO_2. Reproduced with permission [37]. Copyright 2015, American Chemical Society.

$$3MnO_2 + ZnSO_4 + 6H^+ + 3Zn + 4H_2O \rightarrow 3Mn^{2+} + ZnSO_4[Zn(OH)_2]_3 \cdot H_2O \qquad (22)$$

$$[Mn^{2+}] = [ZnSO_4]^{\frac{1}{3}} \cdot [H^+]^2 \cdot e^{-2\Delta\Delta_0/RT} \qquad (23)$$

Furthermore, according to the Equation (23), the solubility of Mn^{2+} at equilibrium state was calculated according to Equation (22). In addition, the content of Mn^{2+} additives will also affect the level of stability. For instance, in the 2 M $ZnSO_4$ electrolyte, as the concentration of the Mn^{2+} additive increases, the battery capacity and stability of a MnO_2/C–Zn battery increase correspondingly, and the performance is optimal when the concentration of $MnSO_4$ reached 0.5 M. [52].

Although the positive role of Mn^{2+} additive has been widely recognized, researchers have made differing claims about the underlying mechanisms. They pointed out that the continuously increased capacity and extended lifespan of Zn/MnO_2 cells is highly related to the concentration of Mn^{2+} additive. The more Mn^{2+} additive added, which could be electro-oxidized, the more MnO_2 can be electrodeposited onto the cathode, and thus higher capacity can be achieved.[53] It would be inevitable of capacity fading since it would be out of Mn^{2+} ions from additive due to the generation of inactive phase. Besides these aforementioned effects, insoluble MnO_x that is deposited on the surface of a $ZnMn_2O_4$ cathode could also serve as host material for Zn^{2+} insertion/ extraction, further increasing the capacity of the cell. Soluble Mn^{2+} from a suitable electrolyte is electrochemically deposited onto the cathode in the form of solid MnO_2 during charging and it undergoes a reverse reaction during discharging, achieving a highly reversible energy storage system.[54] Another useful approach to solve the manganese dissolution issue is to form an interfacial inorganic layer on the cathode. When 2 M $ZnSO_4$ and 0.1 M $MnSO_4$ is used as electrolytes to couple with a Ca_2MnO_4 cathode, the sulfate from the electrolyte combines with calcium ions extracted from the cathode and generates a high-quality calcium sulfate dihydrate ($CaSO_4{\cdot}2H_2O$) film on the surface of cathode. This layered SEI film is verified to significantly suppress the dissolution of manganese and promote cyclability of the battery.[50] Compared with the one-electron reaction based on the Mn^{4+}/Mn^{3+} redox couple, this two-electron redox reaction boosts the theoretical capacity of cathode material to 616 mAh g^{-1}.[55] Besides these good features, the discharge voltage during MnO_2 dissolution process can even reach a higher value than that of the insertion mechanism. However, this theoretical

state is hard to achieve because $Zn_4SO_4(OH)_6 \cdot 4H_2O$ (ZHS) generated during the first discharge process covers the surface of MnO_2 and impedes its further dissolution (Figure 2.6). While, the situation would be mitigated in acidic solution. After adding a small amount of sulphuric acid (H_2SO_4) into 1 M $ZnSO_4$ - 1 M $MnSO_4$ electrolyte in an electrolytic Zn/MnO_2 system, the capacity contribution of the high-voltage region at a stable output voltage of 1.95 V. [56] Although the acidic electrolyte could favor the reaction of MnO_2, it brings the risk of hydrogen evolution and corrosion of the Zn anode. Because the alkaline electrolyte can reduce the potential of the HER and the acid electrolyte can promote the potential of the OER. It is an interesting design to operate the zinc anode in the alkaline environment and cathode in the acid environment to enlarge the electrochemical stability potential window of the aqueous electrolyte and gain a high energy rechargeable aqueous zinc-manganese dioxide battery. [57-58]

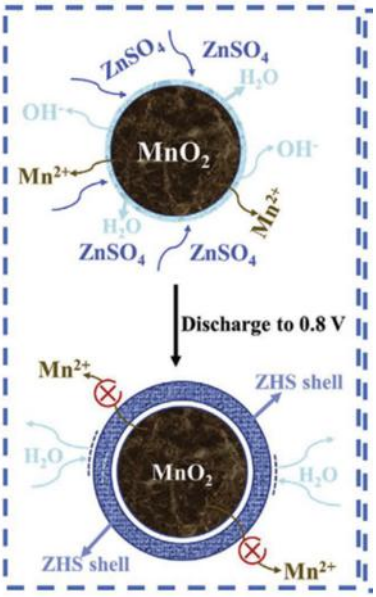

Figure 2.6 Schematic diagram of the formation of $Zn_4SO_4(OH)_6 \cdot 4H_2O$ (ZHS) at the first discharge process.

Preintercalated metal ions can effectively solve the above problem by acting as pillars that stabilize the framework. For example, a layered framework of MnO_2 nanospheres with

zinc-ion pillars as the cathode for AZIBs was prepared via a facile chemical reaction, [59] which exhibited a high capacity of 124 mA h g^{-1} at a current density of 3 A g^{-1} and an outstandingly long lifespan of over 2000 cycles. Similarly, Ca ions were also verified to stabilize layered δ-MnO2 ($Ca_{0.28}MnO_2 \cdot 0.5H_2O$). [60]

Benefiting from the pinning effect of Ca^{2+} ions, the structural stability was strengthened. Thus, the cathode delivered a much higher capacity of 135 mA h g^{-1} at 1.5 A g^{-1} after 300 cycles than the δ-MnO2 cathode (54.9 mA h g^{-1}) and manifested a significantly long cycle life of over 5000 cycles. Cu^{2+}-intercalated layered MnO2 also exhibited long-term cycling stability for over 6000 cycles. [61]

The high reversibility and durability of the cathode during cycling can be ascribed to the redox reaction of the intercalated Cu^{2+}. Cu^{2+} was reduced to Cu during the discharge process, which decreased the charge transfer resistance (R_{ct}) during the redox reaction and ensured that δ-MnO_2 underwent a reversible phase transition from the dissolved state ($Mn(OH)_2$) to the initial state upon charging. In addition, preintercalated metal ions (K^+) were also deemed to play a critical role in alleviating manganese dissolution and preventing structural degradation. [62]

Liang and coworkers found that the dissolution of Mn in Mn_8O_{16} incorporated with K^+ ions was effectively suppressed even after 50 cycles. As shown in the paper that the intercalated K^+ ions bonded with oxygen atoms in the MnO_6 polyhedrons, which strengthened the stability of the tunnel structure and suppressed Mn dissolution.

Based on the above discussion, we agree that Mn-based materials are the most promising cathode candidates for Zn-based batteries, not only because of their environment friendliness and low cost but also because of their controllable reaction mechanisms. For the conventional insertion reaction, the effects of pre-adding Mn2+ into electrolytes are quite prominent in enhancing the capacity and cyclability of batteries. However, its full functions are still in dispute and need further investigation. Compared with the sluggish cation insertion reaction, the deposition/dissolution reaction of MnO_2/Mn^{2+} can fully exhibit the merits of Zn/MnO_2 batteries, in terms of theoretical capacity, output voltage, rate performance, and reversibility.

Nonetheless, it is worth noting that the theoretical capacity calculation based on MnO_2 is not reasonable when it comes to practical application. In fact, the capacity is stored in the electrolyte so its weight and volume should be taken into consideration when labeling the energy density. In addition, some proposed battery systems would not use regular assembly methods, such as coin cells or pouch cells, and therefore, the devices' design and optimization should be taken seriously to minimize the mass and volume of inactive materials.

Liang et al. [63] evaluated the electrochemical behaviors of manganese-based cathodes in three types of conventional electrolytes including aqueous electrolyte, "water-in-salt" electrolyte, and organic electrolyte. The activated electrochemical process in aqueous electrolyte indeed originates from the de-solvation of $Zn(H_2O)_6^{2+}$ at CEI (Fig. 3g). While in the other two electrolytes, there is insufficient or no active water in the electrolyte. It is hard to trigger the de-solvation of Zn^{2+} with the high desolvation energy, so the cathode will exhibit low capacity.

2.3 Issues, Mechanisms and Strategies

The properties of electrolyte, ionic conductivity, Zn^{2+} transfer number, and viscosity are controlled by the interactions among the water solvent, Zn^{2+} cations, and anions. For zinc ion solutes, the difference is controlled by the anions. Normally, bulky anions with electron-withdrawing groups can promote the dissociation and increase the transfer of cations (Table 2.1), which explains the better reversibility and faster kinetics of Zn deposition/dissolution with zinc trifluoromethanesulfonate $Zn(CF_3SO_3)_2$ based electrolytes, compared to $ZnSO_4$ based electrolytes.[64, 65] The ionic conductivity is also influenced by the concentration and viscosity.[66, 67] Generally, as the concentration increases, the ionic conductivity climbs before reaching a peak value and then fades due to a detrimental viscosity increasement. [64, 68] The anions also influence the stability of the electrolyte and the pH value (Table

2.1), [69-77] for instance, unstable ClO^{4-} and NO^{3-} anions may first be decomposed and generate dense layer on Zn. [69, 70]

Table 2.1 Properties of several aqueous Zn^{2+} electrolytes.

Solute	C_0 [M]	σ [mS cm^{-1}]	Passivation layer	Solvation structure	pH	Stability
$ZnSO_4$	2	56.9	$Zn_4(OH)_6SO_4 \cdot xH_2O$	$[Zn(OH_2)_6]^{2+}$	4.9 (1 M)	-1.06-1.18 V (Ag/AgCl)
	3	48.5	$Zn_4(OH)_6SO_4 \cdot 0.5H_2O$		≈ 4.5	
$ZnCl_2$	5	35	$Zn(OH)_2/ZnO$	$[Zn(OH_2)_2Cl_4]^{2-}$-$[Zn(OH)_2]^{2+}$	3.2	-0.3-1.3 V (SHE)
	30	2.5	None	$[ZnCl_4]^{2-}$-$[Zn(OH)_2Cl_4]^{2-}$	5.7	-0.5-1.8 V (SHE)
$Zn(ClO_4)_2$	1		Protect layer		4.9	2.4 V
	4	17.66	$Zn_4ClO_4(OH)_7$ and $Zn_5(OH)_8Cl_2$	$[Zn(OH_2)_6]^{2+}$		2.4 V (Zn/Zn^{2+})
$Zn(BF_4)_2$	4	≈ 10		$Zn(H_2O)_4(BF_4)_2$		2.0 V (Zn/Zn^{2+})
$Zn(Ac)_2$	1		$Zn_5(OH)_6(CO_3)_2$		5.7	
$Zn(NO_3)_2$	0.09		$Zn_5(OH)_8(NO_3)_2 \cdot 2H_2O$		2.85	
$Zn(OTF)_2$	3	≈ 41	$ZnO/Zn(OH)_2$		3.6	2.5 V (Zn/Zn^{2+})
$Zn(TFSI)_2$	1	35.9		$[Zn(OH_2)_6]^{2+}$	3	HER (0.16 V) (Zn/Zn^{2+})

In the table, C denotes concentration, Ac is CH_3COO, OTF is CF_3SO_3, TFSI is NCF_3SO_3, and σ denotes the ionic conductivity.

The solvation structure and the interfacial stability are also affected by the electrolyte. As shown in Figure 2.6, in traditional dilute electrolyte, the large amount of free water molecules results in water molecules surrounded Zn^{2+} solvation sheath and intimate contact between the water molecules and Zn surface. With the regulation of electrolyte, each Zn^{2+} is surrounded by both anions and water molecules, in which the anions possess higher activity than water molecules, thus the interphasial chemistry on the Zn anode is altered. [71, 72] And the schematic Figure 2.7 shows the most issues caused by the aqueous electrolytes.

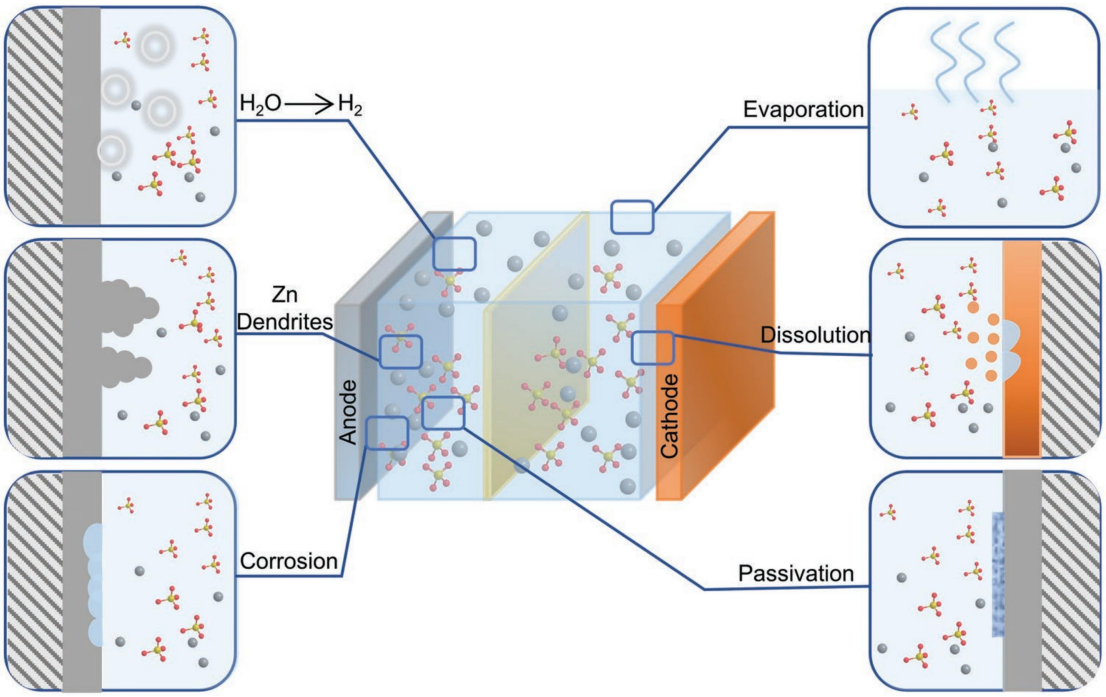

Figure 2.7 Issues of electrolytes and interplay with Zn anode, cathode.

2.3.1 Electrochemical Stability Window

Cell voltage is ultimately confined by electrochemical stability window (ESW) of electrolytes, as the operating voltage of a designed battery is decided by the potential difference of redox reactions between cathode and anode, which should lie within the ESW of electrolyte.[78] The ESW of aqueous electrolyte is governed by the decomposition reactions of water molecules, which is only 1.23 V for pure water and no more than 2.0 V for traditional aqueous electrolytes.[79] This narrow window of aqueous electrolyte disenables the potential cathodes with higher charging voltage over 2.0 V and thus restrains the operating

output voltage, leading to insufficient energy density. The side reactions in an AZIB are heavily related to the undesired reactions of water molecules with/along the electrodes, including Zn corrosion, surface passivation, and H2 evolution. [80, 81] Intensive previous investigations have been dedicated to handling these Zn-related issues in recent years, mainly include the following aspects: 1) constructing an artificial surface electrochemical interface, [82, 83] 2) current collector selecting and structural engineering, [84] 3) designing hierarchical Zn structure or Zn alloy, [85] 4) utilization of water-insalt electrolytes, [86, 87] and 5) introducing additives into electrolytes. [88-90] Among these strategies, the simple design of electrolytes with additives can effectively promote stable and facile Zn stripping/plating from/on zinc electrodes, as the electrolyte is essential to a battery just like blood for a human body. [91, 92] The electrolyte engineering with additives can lead to a synergy effect to the ESW, anode side, and cathode, boosting the electrochemical performance of the full battery, [80, 93] as the electrochemical reactions occur on the interfaces is highly dependent on the electrolyte and the electrodes with a dynamic change during cycling. It is a real devil that complicates the stability of the bulk electrolyte and electrodes. [91, 93] Although these manipulations on the electrolyte have shown a remarkable effect on raising the Coulombic efficiency, utilization, and cycle life, the underlying mechanism on raising the battery voltage, the inhibition of undesired side reactions and Zn dendrites, as well as enhancing the cathode stability has not been entirely understood yet. In this review, through carefully figuring out the principle for the limited ESW, the detailed processes along with the deposition/stripping of the Zn metal, the roots for the side reactions and dendrites are profoundly discussed. With organic molecules as the electrolyte regulator, after sorting out the roles and achievements in the advanced AZIBs, the beneath mechanisms and effects are summarized. Due to the limited research on the cathodes via developing organic molecules in electrolyte tuning, the focus is concentrated on the remarkable effect on the Zn anode. Furthermore, the profits of expanded ESW and widen temperature adaptability for the electrolyte are also included.

Similarly, Zhang et al. [94] did not observe the formation of anode by-products in the "water-in-salt" electrolyte with 30 M $ZnCl_2$, in which the solvated structure will be converted to $[ZnCl_4]^{2-}$. The electrochemical stability window of the $ZnCl_2$ electrolyte was widened along with the decrease in the hydrogen evolution potential due to the increase in concentration, which improved the CE of Zn plating/stripping as well (Fig. 16k). However, in addition to the increasing cost and reducing battery energy density, the electrolyte with an excessively high concentration exposes the characteristics of high viscosity, poor wettability, and low ionic conductivity, which limits the commercial development of Zn^{2+} ion batteries. Nevertheless, this strategy of applying high-concentration electrolytes still has a great practical effect. For example, appropriately increasing the electrolyte concentration is beneficial to the improvement in battery performance. We need to explore the appropriate concentration of electrolytes to achieve the optimization of comprehensive benefits.

2.3.2 Side reactions, corrosion and formation of by-products

Interestingly, the surface of Zn metal possesses different tolerance to corrosion and activation energy for HER and Zn nucleation. Research reveals that, the activation energies for HER increases in the sequence as the order of (110) < (002). [258] Therefore, the side reactions along (002) surface is largely suppressed. Furthermore, the atoms on the (002) plane are compactly arranged and have high binding energy. These contributes to the uniform deposition of Zn on (002) surface. However, in ordinary dilute electrolyte, the poor interactions between the water molecules and Zn surface induced the deposits with (100) surfaces exposed, which further gave rise to side reactions and dendrite issues. Fortunately, some organic molecules prefer to absorb on (002) crystal plane at a parallel state and tend to induce Zn deposition on the (002) facet in a parallel orientation. [258-261]

The stable interfaces can be divided into thermodynamic stability and kinetic stability. Thermodynamically stable interface, where there is no formation of intermediate layer, is conductive to the stability of batteries. Thermodynamic criterion

can be determined by the energy state difference between electrode and electrolyte which is proposed by Goodenough's group [262]. Thermodynamic stability requires: the lowest unoccupied molecular orbital (LUMO) of the electrolyte is higher than the Fermi level of the anode (μ_A), the highest occupied molecular orbital (HOMO) of the electrolyte is below the Fermi level of the cathode (μ_C), as illustrated in Fig. 2.3c, d (drawn with solid line). In other words, μ_A and μ_C locate within the E_g of electrolyte, which constrains the open circuit voltage V_{oc} of a battery:

$$Zn_xMnO_2 \rightarrow MnO_2 + xZn^{2+} + 2xe^- \quad (25)$$

$$ZnMn_2O_4 + Mn^{2+} + 6H_2O \rightarrow ZnMn_3O_7 \cdot 3H_2O + 6H^+ + 4e^- \quad (26)$$

$$Zn_4(OH)_6(SO_4) \cdot 5H_2O + 6H^+ \rightarrow 4Zn^{2+} + SO_4^{2-} + 11H_2O \quad (27)$$

$$eV_{OC} = \mu_A - \mu_C \leqslant E_g \quad (28)$$

$$\Delta E = \Delta E_0 + \eta_C + \eta_A + \eta_O \quad (29)$$

where e is the magnitude of the electron charge.

And if LUMO energy level of A is lower than B that is E (LUMO)(A) < E (LUMO)(B), then the electron would be easier transferred from A to B.

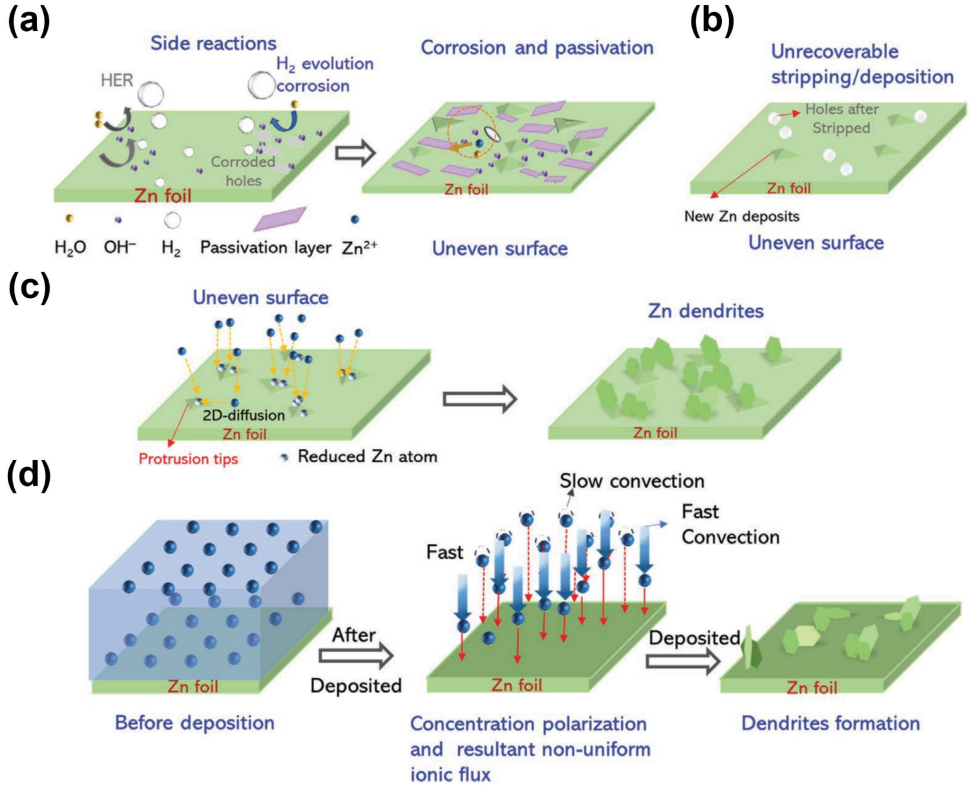

Figure 2.8 Issues associated with aqueous electrolytes and Zn metal anode in aqueous electrolyte. a) Side reactions on Zn anode in aqueous electrolyte; b) stripping resulted holes and newly formed Zn deposits are not at the same positions due to the "hostless" stripping-plating mechanism; c) uneven surface caused dendrite issues; d) concentration polarization caused by slower diffusion compared with redox reaction at the interface, and the resulted dendrites formation. Such concentration polarization gets severer at high current density.

There are no spontaneous reactions on the interface, so that an intrinsic stable EEI can be obtained. Intrinsic stable interfaces where only occurs transfer of charged ions and charges are limited in real condition due to the complicated nature of aqueous electrolyte. Pan et al. proposed a solid-state electrolyte of single-ion conductor in ZIBs [263]. The microporous structure with nano-wetted interface forming fast zinc-ion transport channels. A high Zn^{2+} ions transference number of 0.93 was achieved. However, the electrode potential is generally outside the Eg of electrolyte.

Electrons in the anode flow to the electrolyte when the μA of anode is higher than the LUMO of the electrolyte, resulting in a reduction reaction of electrolyte and formation of AEI film, as illustrated in Fig. 2.3c, d (drawn with dotted line). Similarly, a lower μC of cathode than the HOMO of the electrolyte would lead to the oxidation of electrolyte, and following CEI formation. Different from the decomposition of organic electrolytes, the decomposition of aqueous electrolytes signifies the production of gas (H_2 or O_2). Thermodynamically, the ESW of water restrained by the inherent thermodynamic oxidation potential of OER and reduction potential of HER. Though the actual ESW of aqueous electrolyte is expanded to ~ 2 V due to the exist of overpotential (η). Typically, the practical ESW (ΔE) of water can be described as:

where η_C, η_A and η_O refer to cathodic, anodic and other overpotential. The risk of water splitting suppresses the operating voltage, leading to insufficient energy density of ZIBs. Recent efforts have successfully transplanted the concept of solid/electrolyte interface (SEI) into aqueous media, achieving aqueous lithium-ion battery with an output voltage of 4.5 V. Typically, a more durable interface can be formed by the design of electrode and electrolyte. For instance, the novel water-in-salt (WiS), water-in-bisalt electrolytes and hydrate-melt electrolytes are impressive in expanding voltage window (Fig. 2c). A dense and protective layer formed under the decomposition of salt anion, dissolved O_2/CO_2 and H_2O, which kinetically stabilizes electrolytes at potentials far beyond their thermodynamic stability limits.

The interface, an ionic conductor but electronic insulation, can be kinetically stabilized, and the Zn^{2+} can be free to pass through. Additionally, cost-effective and facile strategies have also been envisioned and implemented by the preconditioning of electrodes and electrolytes. For example, an in-situ generated passivation film was observed in Zn/$Ca_2Mn_2O_4$ batteries, which defended active materials from dissolution. Electrolyte additives, for example, organic acids including tartaric acid, succinic acid, citric acid, etc., can increase hydrogen overpotential and prevent dendrite growth. A

stable SEI of polydopamine is constructed successfully on a Zn anode via an in-situ electrochemical polymerization process of a dopamine additive, which regulated Zn nucleation, Zn-ion conductivity and adhesion capability to achieve dendrite-free Zn deposition, fast Zn^{2+} transport, and alleviated interfacial side reactions. The electrochemical performance improved a lot by these dynamically stable modification strategies. Such strategies focus on in-situ regulation without artificial coating, which is an effective tactic to promote the interfacial stabilities based on kinetically stabilization. The interfacial composition and structure are situated in the condition of dynamic changes during the cycling process. Therefore, the stability of the in-situ interfaces in ZIBs deserves a careful evaluation to obtain a thorough understanding and accelerate the optimization of desired EEI.

For the unstable additive, the HOMO energy level of additives that aid the CEI film is higher than the cathode chemical potential μ_C. This will cause the additive to have higher oxidizability than the cathode, so the additive will preferentially get electrons from the cathode to chemically react and deposit on the cathode surface to form a stable CEI membrane. This CEI film can improve the interface compatibility by protecting the cathode, reducing the interface impedance, and inhibiting further decomposition of the electrolyte.

2.3.3 Zn dendrite

Dendrite traits, including origins, nucleation/growth kinetics, and topologies, are distinct for different MBs (such as Li, [95] Al, [96] Zn, [97] Mg, [98] etc.) due to their respective characteristics. This difference makes it difficult to address some metal dendrites, while it is relatively facile to address others. Because Mg batteries are believed to be less affected by dendrites due to their specific characteristics, we will only briefly discuss and compare Li, Al, and Zn dendrites.

Specifically, Li metal batteries (LMBs) demonstrate the most serious dendrite issue, despite having the lowest Young's modulus and being the most researched. [99, 100] The Li dendrite emerges as a result of the surface roughness-triggered uneven electric field or the inhomogeneous solid electrolyte interface (SEI) formed by the decomposition of organic electrolytes.[101-103] In fact, the protective SEI can suppress the growth of Li dendrites to some degree and rapidly cover the fresh surface of a newly formed Li dendrite, but Li dendrites can still break the defensive SEI layer and further pierce the subsequent separator, resulting in battery failure.[104] This is correlated with the 1D topology and ramified structure of the Li dendrite. On the one hand, the 1D topology, possibly originating from the body-centered cubic (bcc) matrix, manifests aggressive piercing capability (Figure 1a, d). On the other hand, the ramification texture resulting from the large electric field near the interface or space charge enables Li dendrite to invade the separator from multiple directions.[105] Hence, it is very difficult to completely suppress the Li dendrite despite the possible rescuing strategies, such as the adoption of solid-state electrolytes.

Aluminum metal batteries (AMBs) also suffer from the dendrite issue, which has been widely evidenced in various electrolytes (such as AlCl3-NaCl melts,[106] Al-containing ionic liquids (ILs), etc.) [107] and been profoundly studied since 1990.[96, 108] It was uncovered that the Al dendrite forms due to nonuniform Al deposition resulting from increased nucleation sites, which originate from breaks in the Al_2O_3 passivation films.[109] Differing from the SEI in lithium batteries, the Al_2O_3 film is a completely inorganic phase and tends to be anisotropically smashed in specific IL media under the relatively low redox potential of Al. [107] It is worth noting that, rather than the ideal Al^{3+}, a complex anion of $AlCl^{4-}$ dominates the charge carrier system of IL electrolytes, which inevitably lowers the ion transfer efficiency in both the bulk electrolytes and cathodic hosts (Figure 1b, e).[110, 111] Apparently, Al dendrites are topologically ramified, while the branches appear to be 2D structures. This moss-like dendrite is difficult to be addressed considering the complex topology and the inferior ion supply capability due to the sluggish ion diffusion kinetics of anion-type charge carriers such as $AlCl^{4-}$.[112, 113]

Zinc metal batteries (ZMBs) have inevitably encountered the dendrite issue.[114-118] These Janus-type traits are correlated to aqueous electrolytes: 1) Zn stripping/plating proceeds in aqueous media at a zenithally high yet electrochemically stable potential (-0.76 V vs the standard hydrogen electrode (SHE)), which hence addresses the safety concerns and ensures a high power density owing to the fast ion diffusion kinetics;[113-121] 2) microcosmical irregular ion motions such as turbulence and convection can cause uneven ion distribution and consequently trigger dendrite formation.[122, 123] Under the same category of dendrites, the Zn dendrite is distinct from its Li and Al counterparts. Zn dendrites forming in neutral/mildly acidic electrolytes were verified to be 2D hexagonal platelets (a result of a hexagonal close-packed (hcp) crystalline structure) with varied edge sizes according to the adopted cycling conditions and electrolytes (Figure 1c, f). [97, 124, 125] It should be noted that Zn "dendrites" in different electrolytes exhibit different morphologies that will be discussed in detail later herein. The invasive ramified and 1D topologies that are commonly seen in Li and Al dendrites are absent in Zn dendrites in neutral/mildly acidic media, which remarkably weakens the destructiveness in piercing separators that usually causes battery failure. Zn-based batteries working in aqueous electrolytes undergo pH change as a result of the anodic hydrogen evolution, which is thought to promote the formation of inert zincate on Zn anodes and aggravate the Zn dendrite issue. Other metal anodes usually plate and strip in organic electrolytes, where SEI will form as a natural protective layer to mediate the ion flow to attain uniform diffusion.[126, 127] Regarding the formation of dendrites, another pronounced advantage of the Zn anode against its Li and Al competitors is its higher critical overpotential [111] (η) for dendrite nucleation, which can be numerically described as follows where n represents the electron transfer number, D stands for the diffusion coefficient, i0 is the exchange current density, δ is the thickness of the diffusion layer, F is the Faraday constant, R denotes the gas constant, T is the temperature, α is the charge transfer coefficient, and C0 refers to the ion concentration of the bulk electrolyte. This logarithmic relationship can be explained as follows: 1) The superb Zn ion diffusion (D = 3.3 × 10-6 cm2 s-1, orders of magnitudes higher than Li, Na, Mg, and Al, as shown in Figure 2) in aqueous electrolytes

can directly elevate η due to the depletion of the kinetic hysteresis between ion consumption (reduction at the electrode/ electrolyte interface) and ion supply (migration from the bulk electrolyte);[128-132] 2) the multiple electron transfer (n = 2) of the Zn/Zn2+ redox couple can also raise η by increasing the limiting current density; 3) hydrated zinc ions tend to exhibit a thin diffusion layer compared with all other metals in organic/ ionic liquid media due to the gigantic solvation sheaths.[133-137] Therefore, considering the unique topology and high dendrite nucleation overpotential, it is of great scientific interest to systematically investigate the issue of Zn dendrites.

Metallic Zn, which has a moderate redox potential (-0.76 V vs SHE) in neutral aqueous electrolytes, has been directly utilized for anodes as Zn foils or electrodeposited Zn nanostructures.[139, 163, 198] The removal of hydroxyl in neutral electrolytes has addressed the notorious corrosion and Zn passivation issues, which diverts the attention of researchers toward cathodes and electrolytes. However, the frequent sudden failures of current neutral electrolyte-based ZMBs that usually happen during the charging procedure (corresponding to Zn plating) have vigorously evidenced the existence of Zn dendrites, thus forcing a reconsideration of the dendrite issues of ZMBs.[125]

2.3.3.1 Electrolytes and Zn Dendrites

There are remarkable differences among Zn dendrites in different electrolytes. In a strict sense, the Zn dendrites in mild electrolytes are not dendrites because they do not have a ramification texture, and the Zn dendrites in alkaline electrolytes are not even Zn (they are usually zinc oxides). For simplification, we will use “dendrites” to represent all structures formed on the Zn anode in any type of Zn battery and specify their different morphologies and compositions if necessary. Zn dendrites in alkaline systems are related to the instability of $Zn(OH)_4^{2-}$, the special form of the zinc ion in alkaline electrolytes, which easily decomposes into an inert ZnO layer and blocks uniform ion diffusion and deposition.[202] In addition, the

rapid corrosion of the Zn anode that leads to the apparent shape change also aggravates dendrite formation.[203, 204] These alkaline Zn dendrites show a 1D ramified cone-like topology, which is likely to easily pierce the separators (Figure 5a,b).[125] They can form even under moderate conditions of low capacity and current density, implying that their origin lies in thermodynamic instability. In contrast, Zn dendrites in neutral/mildly acidic electrolytes seem to be negligible in moderate conditions, while they are significant in extreme conditions (large capacity and current density) (Figure 5c). This correlates the cause of neutral Zn dendrites with the kinetics factor of zinc ion diffusion. Neutral Zn dendrites were observed to show a 2D hexagonal morphology without ramification, remarkably weakening their piercing capability and enabling relatively facile dendrite protection along the physical shielding approach (Figure 5d). ZMBs using high concentration-salt electrolytes (HCSEs) and organic electrolytes are free from dendrite issues due to the formation of SEIs and the absence of free water molecules, respectively (Figure 5e, f).

2.3.3.2 Accumulation Effect

The accumulation effect is defined here as the dynamically gradual growth of Zn dendrites in both edge size and dendrite layer thickness during long-term stripping/plating. Zn dendrite formation undergoes a dynamic and irreversible process. [205, 206]

Specifically, the electrochemical stripping proceeds not only at the dendrite sites but also at the Zn metal substrate, generating a partially stripped state of the as-formed Zn dendrites.[207] The subsequent plating step tends to preferentially occur at the residual Zn dendrite sites where the large curvature radius will strengthen the localized electric field.[208] This repeated stripping-plating process results in the apparent accumulation of Zn dendrites (Figure 6).[209] This accumulation effect is proposed to originate from the irreversibility of the Zn plating and stripping procedures. In detail, Zn plating involves ion diffusion directed by the electric field, which proceeds at the electrode–electrolyte interface, while Zn stripping refers to the intrinsically uniform electron loss at both the flat substrate and the dendrite sites

(Figure 6). To eliminate the accumulation effect, more effort should be devoted to the homogenization of ionic flow, which is necessary to ensure uniform Zn deposition.

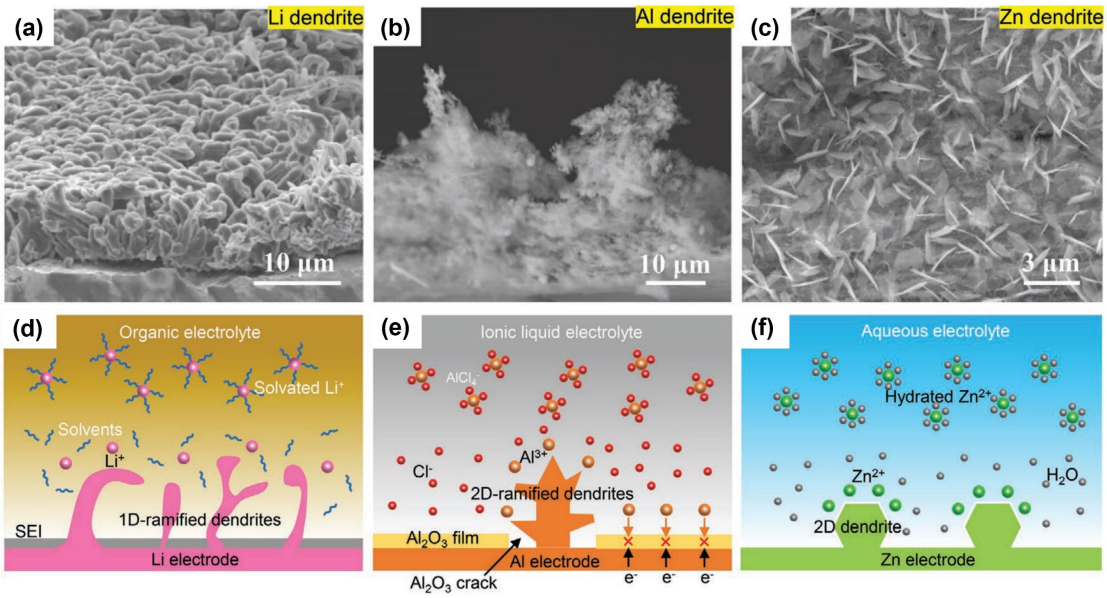

Figure 2.9 The contrast of topologies and ion environments between Zn dendrite and its counterparts (Li, Al). (a) SEM image of Li dendrite. (b) SEM observation of Al dendrite. c) SEM image of Zn dendrite prepared by this work. (d-f) Schematic diagrams showing the topologies of dendrites and the related ion environments for Li, Al, and Zn, respectively.

2.3.4 Advancements in Zn Dendrite Protection

2.3.4.1 Artificial Interface Layer

The artificial interface layer plays a significant role in dendrite protection, mainly according to two strategies: spatial shielding [214] and multimode-guided ion homogeneous diffusion.[215] A direct approach to physical shielding involves using the interface layer to block dendrite growth, which in turn calls for robust mechanical properties in the protective interface. The other method refers to guiding the uniform migration process of Zn^{2+} through multiple steps, such as ion tunnel restraint, chemical adsorption, and electrostatic interaction. Generally speaking, physical shielding functions after Zn plating, while homogeneous

guiding happens during the Zn2+ diffusion process. It is important to identify the desirable traits for an ideal interface layer. After summarizing recent advances, we will scrutinize four crucial factors: conductivity, hydrophily, structure stability, and pore network. As for conductivity, semiconductors or insulators are preferable for the interface layer because they help to avoid surface Zn deposition and ensure that Zn^{2+} transfers through the artificial interface before it is reduced. From the aspect of hydrophily, good hydrophilicity quantified by contact angle (<90°) is beneficial because it lowers the ion interface transfer resistance and thus decreases the overpotential or voltage polarization during Zn plating.[216, 217] Structure stability pertains to the porous network and morphology and is another key factor influencing long-term cycling performance, which compactly depends on the adoption of a binder in the coating layer [218] and powerful enough chemical bonds (such as covalent and H bonds) [219] and cross-linking degrees [220] for an all-in-one film. Later, the pore structure dispersed among the interface layer serves as an ion migration tunnel with its forceful repression on the ion inhomogeneous diffusion driven by the nonuniform electric field. The goal for pore structure design may be directed at the concept of the molecule-level channel, which is thought to exert enormous impacts on the future of dendrite protection in metal-based batteries.

2.3.4.2 Inorganic Interface Layer

Inorganic interface layers were initially grafted onto the Zn electrode through the doctor blade coating method.[221, 222] This interface fabrication technique features a simple process and low cost with heavy dependence on binders (such as poly(vinylidene fluoride)). For example, a nanoscale $CaCO_3$ coating layer with a developed pore structure was reported to favor position-selected Zn deposition and thus improved the symmetric cell lifespan by sevenfold (Figure 8).[223] However, its low areal capacity of only 0.05 mAh cm^{-2} needs further improvement with the consideration of the tens of micrometers-level thickness. In addition, a similarly coated active carbon interface was observed to suppress Zn dendrites

well in both Zn–Na dual-ion and pure Zn-ion electrolytes.[224, 225] Nevertheless, this carbon coating layer demonstrates remarkable dependence on thickness. In addition, high conductivity may also encourage the surface formation of Zn dendrites and thus poses an underlying threat to long-term cycling. Overall, the doctor blade coating strategy still has two major challenges: one refers to lowering the interface layer thickness to improve the volume energy density, and the other involves strengthening the deep coupling between inorganics and binders to avoid structure pulverization. Regarding thickness manipulation and structure maintenance, atomic layer deposition (ALD) represents a next generation technique to simultaneously complete nanoscale film fabrication with ultra-accurate thickness control and atom-level compactness.[226] In this respect, a TiO_2 interface layer was reported to have been deposited onto a Zn electrode with both a super-low thickness of only 8 nm and a regular texture along the 2D solid-solid interface (Figure 9).[227] This excellent ALD interface layer is thus compact enough that it can decrease the exchange current density in aqueous electrolytes, sustain a relatively pH-stable medium, and allow for homogeneous deposition during the repeated cycling process. Despite these advantages, the ALD approach is still challenged by the high cost. A cheap in situ chemically formed Pb film based on the interface replacement reaction of Zn electrodes was proposed to tackle the dendrite issue.[228] This Pb protective interface could polarize the hydrogen evolution side reaction and further prohibit the corrosion of Zn electrodes, even in alkaline electrolytes. Anchoring deposition active sites on Zn electrodes or current collectors is also an attractive method for addressing the dendrite issue by decreasing the nucleation energy and thus guiding uniform Zn deposition. For instance, isolated Au nanoparticles were employed as nucleation seeds to allow for dendrite-free Zn deposition.[229] Interface deposition sites are a promising direction for dendrite restraint that require further profound study ranging from the grafting method to the type of deposition site (such as nanocrystals and functional groups).

2.3.4.3 Organic Interface Layer

The organic interface layer is distinct from its inorganic counterpart. Specifically, the organic interface is usually prepared by spin-coating and it is an all-in-one film compared with the noncompact doctor blade-coating inorganic layer.[230] Rather than adopting binders to sustain integrality, organic interfaces established on the robust covalent cross-linking network demonstrate outstanding structure stability and thus are more likely to avoid destructive structure pulverization during repeated cycling.[231] In addition, the highly reversible shape change associated with their excellent viscoelasticity enables organic interfaces to effectively direct the transverse (parallel to the separator) Zn deposition.[232] Furthermore, the subtle interface coupling between the organic layer and Zn electrode enabled by the rich surface chemistries can remarkably lower the ion interface transfer resistance.[233] Various hydrophilic polymers have been utilized as organic artificial interface layers to address the Zn dendrite issue. For example, an all-in-one polyamide (PA) membrane made using a solving-casting-drying method was recently reported to reach a high coulombic efficiency of 95% for Zn utilization and stable cycling up to 1000 times for a Zn–MnO2 battery (Figure 10).[234] This was attributed to the ion immobility effect in which zinc ions are prevented from free transverse diffusion along the electrode surface by the spatial interaction of the PA network. In addition, this PA interface contributed to the de-solvation of hydrated zinc ions and thus suppressed the side reaction of water splitting. The ion immobility effect was also confirmed in the interface modification of the Zn electrode by poly (ethylene glycol) (PEG). The PEG linear molecular backbones serve as nanofences to block ion migration, as reflected by the apparently modulated exchange current densities.[235] These works present us with an experimental direction with which we can feasibly tackle the Zn dendrite issue by interdicting ion mobility on or near the electrode surface. Interface chemistry has also been found to strengthen the dendrite protection of the Zn electrode. In this respect, polyacrylonitrile (PAN) membranes cross-linked by Li_2S_3 introduced extra S-containing groups to guide the homogeneous ionic flow to attain dendrite-free Zn

deposition.[239] Nevertheless, the ultra large thickness of 500 μm of this screen-printed PAN interface needs to be decreased in comparison with the tens of micrometers-level Zn electrode.

The SEI, a crucial protective layer for LIB anodes, also plays a significant role in solving the Zn dendrite issue. The SEI protection strategy originated from the use of HCSEs with organic anions in Zn hybrid batteries and underwent further development in recent years. Preliminarily, the HSCEs of $Zn(TFSI)_2$ were reported to permit highly reversible Zn stripping/plating as reflected by ideal cyclic voltammetry (CV) curves.[175] In addition, the deposited Zn was also observed to be free from the hexagonal nanosheet topology exclusively demonstrated by Zn plated in normal aqueous electrolytes. These highly desirable traits were subsequently shown to benefit from the formation of a SEI consisting of fluorides and sulfides, which originates from the decomposition of organic anion-type electrolyte.[128] Under SEI protection, the as-assembled symmetrical cells deliver excellent cycling lifespans without being affected by increased current densities despite the slightly increased voltage hysteresis. More recently, a quasi-SEI interface was reported to be formed based on the electrostatic interaction between the deprotonized carboxyls of sodium polyacrylate and positively charged zinc ions (Figure 11).[240] This quasi-SEI promotes the localized nucleation growth behavior of Zn deposition and thus eliminates the formation of Zn dendrites. Currently, SEI layers form indirectly, according to the mutual effect between the Zn electrode and electrolytes directly grafting like other interfaces mentioned previously.[241] In general, despite the outstanding dendrite suppression capability permitted by their structural and chemical stability, organic interface layers retain significant dependence on toxic volatile solvents during the solving-casting-drying process. The use of these toxic solvents poses a great threat to the green aqueous ZMBs. [242–244] In addition, the current thickness (30-500 μm) of the interface layers needs to be decreased to less than that of the Zn anode with consideration of the whole volume energy density. Combining the artificially grafted polymer interface with the indirectly formed SEI appears to be a good choice for achieving overall dendrite protection. Considering the trade-off between the cycling lifespan and rate capability,

it is desirable to optimize the thickness to effectively guide Zn^{2+} flow and lower the diffusion resistance as much as possible. Currently, several methods, including atomic layer deposition (ALD), doctor-blade coating, spin-coating, and in situ interface synthesis, have been developed to integrate different materials (inorganic metal oxides, organic polymers, etc.) with the Zn anode. The optimal thicknesses are quite different in different methods. For ALD, the atomic matrix is dense, so it is best if the thickness is less than dozens of nanometers. Artificial interface layers prepared using other methods are thought to require a thickness of less than 1 μm considering the porous structures of the layers.

2.3.4.4 Electrolyte Modification

The electrolyte modification strategy refers to adopting organic/inorganic additives, designing gel, or all-solid-state electrolytes, and developing wholly organic electrolytes or HCSEs to functionalize and substitute current dendrite permitted aqueous electrolytes. These approaches enable the modified electrolytes to regulate ion migration in both bulk electrolytes and the microspace near the electrolyte-electrode interface to attain homogeneous distribution before Zn plating. After that, modified electrolytes can also supply spatial shielding to mechanically guide the growth direction of Zn deposition. In addition, the modification methods mentioned previously exhibit good compatibility with current cathodes: for example, organic electrolytes benefit PBA-type cathodes, while they are bad for Mn-based cathodes. This involves subtle H+ storage and desolvation behaviors that will be discussed in detail in the following sections. Electrolyte modification with both bulk and interface interaction is thus thought to demonstrate enormous potential in effectively solving Zn dendrite issues.

2.3.4.5 Additives

Electrolyte additives devoted to attaining efficient dendrite protection without changing the specific solvation sheath and H+ storage behavior are significant for maintaining the advantages of high energy density and superior rate capability of aqueous ZMBs. The additive family mainly consists of organic molecules, inorganic salts, organic cations, and organic anions, with distinct dendrite suppressed mechanisms. [245, 246] Inorganic additives usually depend on their high-redox-potential cations to electrostatically screen zinc ions at the dendrite sites to realize even Zn deposition. In comparison, slight organic additives can remarkably improve the interface wettability of aqueous electrolytes on lyophobic Zn metal anodes and thus encourage uniform dispersion along the whole 2D electrode surface. Another advantage of utilizing additives is to lower the freezing point of electrolytes to endow the battery devices with antifreezing functionality. [203, 247]

Diethyl ether was adopted as an organic additive in a dendrite-free Zn–MnO2 system with both long lifespan and high capacity (near 300 mAh g^{-1}).[192] This excellent performance is attributed to the molecule screening of additives at the metallic Zn anode as well as the unchanged dual-ion (Zn^{2+} and H^{+}) storage at the MnO2 cathode. As described in Figure 12a, however, diethyl ether is only adsorbed onto the dendrite sites rather than the adjacent plate regions, which is thought to be a difficult process without any special stimuli. Inorganic additives can easily address this concern by replacing molecule screening with electrostatic shielding. For instance, ordinary Na_2SO_4 was added to aqueous electrolytes to eliminate Zn dendrites based on the electrostatic shielding effect (Figure 12b).[248] This electrostatic interaction utilizes high-redox-potential Na+, which is anchored on dendrite sites triggered by the locally enhanced electric field intensity, to repel zinc ions so they transversely move to the adjacent planar substrate to attain homogeneous deposition. This inorganic additive was also asserted to inhibit the dissolution of the V-based cathode. Similar to its inorganic counterpart, the organic cation is another electrolyte additive exploiting the electrostatic shielding interaction to tackle the Zn dendrite issue. 1-Methyl-pyrrolidinium

bromide, which was initially used as a bromine complex agent in a zinc-bromide flow battery, was reported to exhibit desirable dendrite suppression even in alkaline electrolytes due to organic cation-driven electrostatic shielding.[249]

Electrolyte additives can improve the intrinsic Zn deposition behavior by mediating the crystallographic orientation. Specifically, the organic anion-type additive sodium dodecyl benzene sulfonate (SDBS) was reported to strengthen the (100) lattice plane in comparison with the (002) lattice plane.[250] This artificially directed change in Zn deposition behavior transforms the loose hexagonal nanosheet topology into a compact smooth one. Additionally, along this crystallographic orientation manipulation approach, other electrolyte additives such as boric acid, indium sulfate, and tin oxide were also investigated to widen the additive family.[251] However, a completely contrary hypothesis was proposed: Zn deposition toward the (002) lattice plane is intensified to suppress the Zn dendrite, as evidenced by X-ray powder diffraction (XRD) and scanning electron microscopy (SEM) observation. Despite this conflict, using electrolyte additives to regulate crystallographic orientation represents a promising method for inhibiting Zn dendrites, while the typical lattice plane associated with the profound mechanism still needs further investigation.

Actually, during the Zn deposition process, the previously generated Zn nuclei also form a large local electric field to affect subsequent nucleation and growth. Therefore, adjusting the initial nucleation site is of great significance for realizing a dendrite-free anode. According to the Sand's time model (Equation 24), we could modify and regulate the configuration of electrolyte to suppress the formation of dendrite.

$$\tau = \pi D \frac{\mathrm{e}C_0(u_\mathrm{a} + u_\mathrm{c})^2}{2Ju_\mathrm{a}} \tag{24}$$

τ : dendrite formation time, e: electronic charge, D: diffusion constant, C_0: initial concentration of the electrolyte, J: effective current density, u_a: anionic mobility, u_c: cationic mobility.

To extend the dendrite formation time τ, the goal is to enable the high initial concentration of C_0, increasement of the diffusion constant D, improvement of the anionic mobility u_a, abatement of cationic mobility u_c and decrease of the effective current density J. Besides, Reza Shahbazian-Yassar have demonstrated non-dendritic Zn electrodeposition process can be achieved by zincophilic monolayer graphene layer substrates with a strong affinity to Zn (binding energy of 4.41 eV).

As present above, the organic molecules really show their significant roles in suppressing the Zn dendrites. Uniform surface energy, electrical field, and ionic flux is ideal state to eliminate the Zn dendrites. However, the irreversible stripping and deposition process is potential to bring about the uneven surface after several cycles of deposition/stripping.[252] So, the kinetic process should be tuned to guarantee more and smaller uniform nucleus in the initial step of deposition, and planar deposits is highly desired. With the organic molecules chemically adsorbed on the Zn surface, the enhanced zincophilicity increases the driving force for nucleation to yield a uniform distribution of small metal nuclei. Based on this, compact and uniform depositions form.[253, 254] For the solvation tuning, the incorporation of organic molecules strengthens the Zn-organic interactions, and the high adsorption energy of the organic molecules improves the interfacial Zn metal-organic molecule-Zn^{2+} charge carriers bonding, the both enhanced ionic transfer and electron transport significantly promoted the uniform nucleation and growth.[255] However, charge-transfer barrier usually gets aggravated due to the high de-solvation energy (bond cleavage of Zn-organic), although the higher resistance can slow down the deposition process to smooth the deposits.[256] Note that the output voltage will be accordingly lowered especially at a high current density. So, it is advocated to build SEI to facilitate the de-solvation, and meanwhile this in situ formed Zn^{2+}-selectively conductive, hydrophobic, and electrical insulated SEI can further tune the ionic flux and homogenize the nucleation sites.[257]

References

[1] Q. Yang, Q. Li, Z. Liu, D. Wang, Y. Guo, X. Li, Y. Tang, H. Li, B. Dong, C. Zhi, *Adv. Mater.* **2020**, 2001854.

[2] D. Wang, Q. Li, Y. Zhao, H. Hong, H. Li, Z. Huang, G. Liang, Q. Yang, and C. Zhi, *Adv. Energy Mater.* **2022**, 2102707.

[3] H. Li, L. Ma, C. Han, Z. Wang, Z. Liu, Z. Tang, C. Zhi, *Nano Energy* 62 (**2019**) 550–587.

[4] D. Chao, S. Qiao, *Joule*, **2020**, 4, 1846-1851.

[5] T. Zhang, Y. Tang, S. Guo, X. Cao, A. Pan, G. Fang, J. Zhou and S. Liang. *Energy Environ. Sci.*, **2020**,13, 4625-4665.

[6] H. Li, L. Ma, C. Han, Z. Wang, Z. Liu, Z. Tang, C. Zhi, *Nano Energy* 62 (**2019**) 550–587.

[7] J. Xiao, *Science* **2019**, 366, 426.

[8] T. Zhang, Y. Tang, S. Guo, X. Cao, A. Pan, G. Fang, J. Zhou and S. Liang. *Energy Environ. Sci.*, **2020**,13, 4625-4665.

[9] Y. Liang, H. Dong, D. Aurbach and Y. Yao, *Nat. Energy*, **2020**, 5, 646–656.

[10] J. Ming, J. Guo, C. Xia, W. Wang and H. N. Alshareef, *Mater. Sci. Eng.*, **2019**, 135, 58–84.

[11] L. Zhang, Y. Pan, Y. Chen, M. Li, P. Liu, C. Wang, P. Wang and H. Lu, *Chem. Commun.*, **2019**, 55, 4258–4261.

[12] O. Ellabban, H. Abu-Rub and F. Blaabjerg, *Renew. Sust. Energ. Rev.*, **2014**, 39, 748-764.

[13] P. Yu, Y. Zeng, H. Zhang, M. Yu, Y. Tong, X. Lu, *Small* 15 (**2019**) 1804760.

[14] D. Lin, Y. Liu and Y. Cui, *Nat. Nanotechnol.*, **2017**, 12, 194– 206.

[15] D. Larcher and J. M. Tarascon, *Nat. Chem.*, **2015**, 7, 19–29.

[16] J. Hao, X. Li, X. Zeng, D. Li, J. Mao and Z. Guo, *Energy Environ. Sci.*, **2020**, 13, 3917–3949.

[17] L. E. Blanc, D. Kundu and L. F. Nazar, *Joule*, **2020**, 4, 771– 799.

[18] P. He, Q. Chen, M. Yan, X. Xu, L. Zhou, L. Mai and C.-W. Nan, *EnergyChem*, **2019**, 1, 100022.

[19] T. Wang, C. Li, X. Xie, B. Lu, Z. He, S. Liang and J. Zhou, *ACS Nano*, **2020**, 14, 16321–16347.

[20] M. Armand and J. M. Tarascon, *Nature*, **2008**, 451, 652–657.

[21] V. Etacheri, R. Marom, R. Elazari, G. Salitra and D. Aurbach, *Energy Environ. Sci.*, **2011**, 4, 3243–3262.

[22] J. M. Tarascon and M. Armand, *Nature*, **2001**, 414, 359–367.

[23] S. Huang, J. Zhu, J. Tian and Z. Niu, *Chem.–Eur. J.*, **2019**, 25, 14480–14494.

[24] M. Rashad, M. Asif, Y. Wang, Z. He and I. Ahmed, *Energy Stor. Mater.*, **2020**, 25, 342–375.

[25] C. Xu, B. Li, H. Du and F. Kang, *Angew. Chem., Int. Ed.*, **2012**, 51, 933–935.

[26] M.-C. Lin, M. Gong, B. Lu, Y. Wu, D.-Y. Wang, M. Guan, M. Angell, C. Chen, J. Yang, B.-J. Hwang and H. Dai, *Nature*, **2015**, 520, 324–328.

[27] M. Mao, T. Gao, S. Hou and C. Wang, *Chem. Soc. Rev.*, **2018**, 47, 8804–8841.

[28] B. Tang, L. Shan, S. Liang and J. Zhou, *Energy Environ. Sci.*, **2019**, 12, 3288–3304.

[29] E. Hu and X.-Q. Yang, *Nat. Mater.*, **2018**, 17, 480–481.

[30] K. Wang, P. Pei, Z. Ma, H. Chen, H. Xu, D. Chen and X. Wang, *J. Mater. Chem. A*, **2015**, 3, 22648–22655.

[31] W. Lu, C. Xie, H. Zhang and X. Li, *ChemSusChem*, **2018**, 11, 3996–4006.

[32] L. Chen, Y. Ruan, G. Zhang, Q. Wei, Y. Jiang, T. Xiong, P. He, W. Yang, M. Yan, Q. An and L. Mai, *Chem. Mater.*, **2019**, 31, 699–706.

[33] J. Li, K. McColl, X. Lu, S. Sathasivam, H. Dong, L. Kang, Z. Li, S. Zhao, A. G. Kafizas, R. Wang, D. J. L. Brett, P. R. Shearing, F. Corà, G. He, C. J. Carmalt and I. P. Parkin, *Adv. Energy Mater.*, **2020**, 10, 2000058.

[34] T. Liu, X. Cheng, H. Yu, H. Zhu, N. Peng, R. Zheng, J. Zhang, M. Shui, Y. Cui and J. Shu, *Energy Stor. Mater.*, **2019**, 18, 68–91.

[35] W. Zhang, X. Zhai, Y. Zhang, H. Wei, J. Ma, J. Wang, L. Liang, Y. Liu, G. Wang, F. Ren, S. Wei, *Front. Energy Res.* **2020**, 8, 585795.

[36] T. Xiong, Y. Zhang, W. S. V. Lee, J. Xue, *Adv. Energy Mater.* **2020**, 10, 2001769.

[37] M.H. Alfaruqi, V. Mathew, J. Gim, S. Kim, J. Song, J.P. Baboo, S.H. Choi, J. Kim, *Chem. Mater.* 27 (**2015**) 3609-3620.

[38] W. Sun, F. Wang, S. Hou, C. Yang, X. Fan, Z. Ma, T. Gao, F. Han, R. Hu, M. Zhu, C. Wang, *J. Am. Chem. Soc.* **2017**, 139, 9775.

[39] G. Z. Fang, C. Y. Zhu, M. H. Chen, J. Zhou, B. Y. Tang, X. X. Cao, X. S. Zheng, A. Q. Pan and S. Q. Liang, *Adv Funct Mater.*, **2019**, 29, 1808375.

[40] N. Zhang, F. Cheng, Y. Liu, Q. Zhao, K. Lei, C. Chen, X. Liu and J. Chen, *J Am Chem Soc*, **2016**, 138, 12894-12901.

[41] Y. Jin, L. Zou, L. Liu, M. H. Engelhard, R. L. Patel, Z. Nie, K. S. Han, Y. Shao, C. Wang, J. Zhu, H. Pan and J. Liu, *Adv. Mater.* **2019**, 31, 1900567.

[42] F. Wang, O. Borodin, T. Gao, X. Fan, W. Sun, F. Han, A. Faraone, J. A. Dura, K. Xu and C. Wang, *Nat. Mater.*, **2018**, 17, 543-549.

[43] W. Ling, P. Wang, Z. Chen, H. Wang, J. Wang, Z. Ji, J. Fei, Z. Ma, N. He and Y. Huang, *ChemElectroChem*, **2020**, 7, 2957–2978.

[44] T. C. Li, D. Fang, J. Zhang, M. E. Pam, Z. Y. Leong, J. Yu, X. L. Li, D. Yan and H. Y. Yang, *J. Mater. Chem. A*, **2021**, 9, 6013–6028.

[45] G. Fang, J. Zhou, A. Pan and S. Liang, *ACS Energy Lett.*, **2018**, 3, 2480–2501.

[46] H. Li, L. Ma, C. Han, Z. Wang, Z. Liu, Z. Tang and C. Zhi, *Nano Energy*, **2019**, 62, 550–587.

[47] B. Lee, C. S. Yoon, H. R. Lee, K. Y. Chung, B. W. Cho, S. H. Oh, *Sci. Rep.* **2014**, 4, 6066.

[48] S. Guo, S. Liang, B. Zhang, G. Fang, D. Ma, J. Zhou, *ACS Nano*, **2019**, 13, 13456–13464.

[49] C. Xia, J. Guo, P. Li, X. Zhang, H.N. Alshareef, *Angew. Chem. Int. Ed.* **2018**, 57, 3943–3948.

[50] Y. Yang, Y. Tang, G. Fang, L. Shan, J. Guo, W. Zhang, C. Wang, L. Wang, J. Zhou, S. Liang, *Energy Environ. Sci.* **2018**, 11, 3157–3162.

[51] S. Guo, L. Qin, T. Zhang, M. Zhou, J. Zhou, G. Fang, S. Liang, *Energy Stor. Mater.* **2021**, 34, 545.

[52] G. Li, Z. Huang, J. Chen, F. Yao, J. Liu, O.L. Li, S. Sun, Z. Shi, *J. Mater. Chem. A*, **2020**, 8, 1975–1985.

[53] V. Soundharrajan, B. Sambandam, S. Kim, S. Islam, J. Jo, S. Kim, V. Mathew, Y.-k. Sun, J. Kim, *Energy Stor. Mater.* **2020**, 28, 407.

[54] M. Li, Q. He, Z. Li, Q. Li, Y. Zhang, J. Meng, X. Liu, S. Li, B. Wu, L. Chen, Z. Liu, W. Luo, C. Han, L. Mai, *Adv. Energy Mater.* **2019**, 9, 1901469.

[55] D. Chao, W. Zhou, C. Ye, Q. Zhang, Y. Chen, L. Gu, K. Davey, S.-Z. Qiao, *Angew. Chem., Int. Ed.* **2019**, 58, 7823.

[56] D. Chao, C. Ye, F. Xie, W. Zhou, Q. Zhang, Q. Gu, K. Davey, L. Gu and S. Z. Qiao, *Adv. Mater*, **2020**, 32, 2001894.

[57] G. G. Yadav, D. Turney, J. C. Huang, X. Wei and S. Banerjee, *ACS Energy Lett.*, **2019**, 4, 2144-2146.

[58] B.Y. Tang, L.T. Shan, S.Q. Liang, J. Zhou, *Energy Environ. Sci.* **2019**, 12, 3288–3304.

[59] J. Wang, J.-G. Wang, H. Liu, C. Wei and F. Kang, *J. Mater. Chem. A*, **2019**, 7, 13727–13735.

[60] T. Sun, Q. Nian, S. Zheng, J. Shi and Z. Tao, *Small*, **2020**, 16, 2000597.

[61] G. G. Yadav, J. W. Gallaway, D. E. Turney, M. Nyce, J. Huang, X. Wei and S. Banerjee, *Nat. Commun.*, **2017**, 8, 14424.

[62] G. Fang, C. Zhu, M. Chen, J. Zhou, B. Tang, X. Cao, X. Zheng, A. Pan and S. Liang, *Adv. Funct. Mater.*, **2019**, 29, 1808375.

[63] T. Zhang, Y. Tang, G. Fang, C. Zhang, H. Zhang, X. Guo, X. Cao, J. Zhou, A. Pan, S. Liang, *Adv. Funct. Mater.* **2020**, 30, 2002711.

[64] N. Zhang, F. Cheng, Y. Liu, Q. Zhao, K. Lei, C. Chen, X. Liu, J. Chen, *J. Am. Chem. Soc.* **2016**, 138, 12894.

[65] a) J. Wang, Y. Yang, Y. Zhang, Y. Li, R. Sun, Z. Wang, H. Wang, *Energy Stor. Mater.* **2021**, 35, 19; b) Z. Ye, Z. Cao, M. O. Lam Chee, P. Dong, P. M. Ajayan, J. Shen, M. Ye, *Energy Storage Mater.* **2020**, 32, 290.

[66] M. S. Ding, L. Ma, M. A. Schroeder, K. Xu, *J. Phys. Chem. C* **2020**, 124, 25249.

[67] T. Zhang, Y. Tang, S. Guo, X. Cao, A. Pan, G. Fang, J. Zhou, S. Liang, *Energy Environ. Sci.* **2020**, 13, 4625.

[68] M. S. Ding, A. von Cresce, K. Xu, *J. Phys. Chem. C* **2017**, 121, 2149.

[69] L. Wang, Y. Zhang, H. Hu, H.-Y. Shi, Y. Song, D. Guo, X.-X. Liu, X. Sun, *ACS Appl. Mater. Interfaces* **2019**, 11, 42000.

[70] D. Li, L. Cao, T. Deng, S. Liu, C. Wang, *Angew. Chem., Int. Ed.* **2021**, 60, 13035.

[71] L. Suo, O. Borodin, T. Gao, M. Olguin, J. Ho, X. Fan, C. Luo, C. Wang, K. Xu, *Science* **2015**, 350, 938.

[72] C. Yan, H.-R. Li, X. Chen, X.-Q. Zhang, X.-B. Cheng, R. Xu, J.-Q. Huang, Q. Zhang, *J. Am. Chem. Soc.* **2019**, 141, 9422.

[73] X. Guo, Z. Zhang, J. Li, N. Luo, G.-L. Chai, T. S. Miller, F. Lai, P. Shearing, D. J. L. Brett, D. Han, Z. Weng, G. He, I. P. Parkin, *ACS Energy Lett.* **2021**, 6, 395.

[74] C. Zhang, J. Holoubek, X. Wu, A. Daniyar, L. Zhu, C. Chen, D. P. Leonard, I. A. Rodríguez-Pérez, J.-X. Jiang, C. Fang, X. Ji, *Chem. Commun.* **2018**, 54, 14097.

[75] W. Yang, X. Du, J. Zhao, Z. Chen, J. Li, J. Xie, Y. Zhang, Z. Cui, Q. Kong, Z. Zhao, C. Wang, Q. Zhang, G. Cui, *Joule* **2020**, 4, 1557.

[76] T. Sun, X. Yuan, K. Wang, S. Zheng, J. Shi, Q. Zhang, W. Cai, J. Liang, Z. Tao, *J. Mater. Chem. A* **2021**, 9, 7042.

[77] A. Moezzi, M. Cortie, A. M. McDonagh, Eur. *J. Inorg. Chem.* **2013**, 2013, 1326.

[78] Z. Liu, Y. Huang, Y. Huang, Q. Yang, X. Li, Z. Huang, C. Zhi, *Chem. Soc. Rev.* **2020**, 49, 180.

[79] D. Chao, S.-Z. Qiao, *Joule* **2020**, 4, 1846.

[80] L. E. Blanc, D. Kundu, L. F. Nazar, *Joule* **2020**, 4, 771.

[81] V. Verma, S. Kumar, W. Manalastas, M. Srinivasan, *ACS Energy Lett.* **2021**, 6, 1773.

[82] Q. Yang, Y. Guo, B. Yan, C. Wang, Z. Liu, Z. Huang, Y. Wang, Y. Li, H. Li, L. Song, J. Fan, C. Zhi, *Adv. Mater.* **2020**, 32, 2001755.

[83] J. Hao, X. Li, S. Zhang, F. Yang, X. Zeng, S. Zhang, G. Bo, C. Wang, Z. Guo, *Adv. Funct. Mater.* **2020**, 30, 2001263.

[84] a) Z. Wang, J. Huang, Z. Guo, X. Dong, Y. Liu, Y. Wang, Y. Xia, *Joule* **2019**, 3, 1289; b) Y. Zeng, X. Zhang, R. Qin, X. Liu, P. Fang, D. Zheng, Y. Tong, X. Lu, *Adv. Mater.* **2019**, 31, 1903675; c) Q. Li, Y. Wang, F. Mo, D. Wang, G. Liang, Y. Zhao, Q. Yang, Z. Huang, C. Zhi, *Adv. Energy Mater.* **2021**, 11, 2003931.

[85] a) S.-B. Wang, Q. Ran, R.-Q. Yao, H. Shi, Z. Wen, M. Zhao, X.-Y. Lang, Q. Jiang, *Nat. Commun.* **2020**, 11, 1634; b) H. Tian, Z. Li, G. Feng, Z. Yang, D. Fox, M. Wang, H. Zhou, L. Zhai, A. Kushima, Y. Du, Z. Feng, X. Shan, Y. Yang, *Nat. Commun.* **2021**, 12, 237.

[86] F. Wang, O. Borodin, T. Gao, X. Fan, W. Sun, F. Han, A. Faraone, J. A. Dura, K. Xu, C. Wang, *Nat. Mater.* **2018**, 17, 543.

[87] L. Zhang, I. A. Rodríguez-Pérez, H. Jiang, C. Zhang, D. P. Leonard, Q. Guo, W. Wang, S. Han, L. Wang, X. Ji, *Adv. Funct. Mater.* **2019**, 29, 1902653.

[88] J. Hao, L. Yuan, C. Ye, D. Chao, K. Davey, Z. Guo, S. Z. Qiao, *Angew. Chem., Int. Ed. Engl.* **2021**, 60, 7366.

[89] P. Sun, L. Ma, W. Zhou, M. Qiu, Z. Wang, D. Chao, W. Mai, *Angew. Chem., Int. Ed. Engl.* **2021**, 60, 18247.

[90] W. Xu, K. Zhao, W. Huo, Y. Wang, G. Yao, X. Gu, H. Cheng, L. Mai, C. Hu, X. Wang, *Nano Energy* **2019**, 62, 275.

[91] J. Song, K. Xu, N. Liu, D. Reed, X. Li, *Mater. Today* **2021**, 45, 191.

[92] S. Guo, L. Qin, T. Zhang, M. Zhou, J. Zhou, G. Fang, S. Liang, *Energy Stor. Mater.* **2021**, 34, 545.

[93] H. Qiu, X. Du, J. Zhao, Y. Wang, J. Ju, Z. Chen, Z. Hu, D. Yan, X. Zhou, G. Cui, *Nat. Commun.* **2019**, 10, 5374.

[94] C. Zhang, J. Holoubek, X. Wu, A. Daniyar, L. Zhu, *Chem. Commun.* **2018**, 54 (100), 14097–14099.

[95] J. F. Parker, C. N. Chervin, I. R. Pala, M. Machler, M. F. Burz, J. W. Long, D. R. Rolison, *Science* **2010**, 356, 415.

[96] D. Lin, Y. Liu, Y. Cui, *Nat. Nanotechnol.* **2017**, 12, 194.

[97] M.-C. Lin, M. Gong, B. Lu, Y. Wu, D.-Y. Wang, M. Guan, M. Angell, C. Chen, J. Yang, B.-J. Hwang, H. Dai, *Nature* **2015**, 520, 324.

[98] X.-B. Cheng, R. Zhang, C.-Z. Zhao, Q. Zhang, *Chem. Rev.* **2017**, 117, 10403.

[99] H. Yang, H. Li, J. Li, Z. Sun, K. He, H.-M. Cheng, F. Li, *Angew. Chem., Int. Ed.* **2019**, 131, 12104.

[100] J. Zheng, Q. Zhao, T. Tang, J. Yin, C. D. Quilty, G. D. Renderos, X. Liu, Y. Deng, L. Wang, D. C. Bock, C. Jaye, D. Zhang, E. S. Takeuchi, K. J. Takeuchi, A. C. Marschilok, L. A. Archer, *Science* **2019**, 366, 645.

[101] M. Mao, T. Gao, S. Hou, C. Wang, *Chem. Soc. Rev.* **2018**, 47, 8804.

[102] C. A. Swenson, *J. Phys. Chem. Solids* **1966**, 27, 33.

[103] M. D. Tikekar, S. Choudhury, Z. Tu, L. A. Archer, *Nat. Energy* **2016**, 1, 16114.

[104] X. Cao, X. Ren, L. Zou, M. H. Engelhard, W. Huang, H. Wang, B. E. Matthews, H. Lee, C. Niu, B. W. Arey, Y. Cui, C. Wang, J. Xiao, J. Liu, W. Xu, J.-G. Zhang, *Nat. Energy* **2019**, 4, 796.

[105] C.-S. Yang, J.-J. Kim, T. S. Kim, P. Y. Lee, S. Y. Kim, H.-M. Lee, D.-M. Shin, L. T. Nguyen, M.-S. Lee, H. S. Jin, K.-K. Kim, C.-H. Lee, M. H. Kim, S. G. Park, J.-M. Kim, H.-S. Choi, E.-K. Jo, *Nat. Commun.* **2015**, 6, 6115.

[106] Y. Gu, W.-W. Wang, Y.-J. Li, Q.-H. Wu, S. Tang, J.-W. Yan, M.-S. Zheng, D.-Y. Wu, C.-H. Fan, W.-Q. Hu, Z.-B. Chen, Y. Fang, Q.-H. Zhang, Q.-F. Dong, B.-W. Mao, *Nat. Commun.* **2018**, 9, 1339.

[107] G. Zheng, C. Wang, A. Pei, J. Lopez, F. Shi, Z. Chen, A. D. Sendek, H.-W. Lee, Z. Lu, H. Schneider, M. M. Safont-Sempere, S. Chu, Z. Bao, Y. Cui, *ACS Energy Lett.* **2016**, 1, 1247.

[108] J. N. Chazalviel, *Phys. Rev. A* **1990**, 42, 7355.

[109] H. Chen, H. Xu, S. Wang, T. Huang, J. Xi, S. Cai, F. Guo, Z. Xu, W. Gao, C. Gao, *Sci. Adv.* **2017**, 3, eaao7233.

[110] H. Wang, S. Gu, Y. Bai, S. Chen, F. Wu, C. Wu, *ACS Appl. Mater. Interfaces* **2016**, 8, 27444.

[111] Q. Li, H. A. Hjuler, R. W. Berg, N. J. Bjerrum, *J. Electrochem. Soc.* **1990**, 137, 1184.

[112] H. Chen, H. Xu, S. Wang, T. Huang, J. Xi, S. Cai, F. Guo, Z. Xu, W. Gao, C. Gao, *ACS Appl. Mater. Interfaces* **2017**, 9, 22628.

[113] D. J. Kim, D.-J. Yoo, M. T. Otley, A. Prokofjevs, C. Pezzato, M. Owczarek, S. J. Lee, J. W. Choi, J. F. Stoddart, *Nat. Energy* **2019**, 4, 51.

[114] D. Pradhan, D. Mantha, R. G. Reddy, *Metall. Mater. Trans. B* **2012**, 43, 519.

[115] M. Walter, K. V. Kravchyk, C. Böfer, R. Widmer, M. V. Kovalenko, *Adv. Mater.* **2018**, 30, 1705644.

[116] S. Wang, Z. Yu, J. Tu, J. Wang, D. Tian, Y. Liu, S. Jiao, *Adv. Energy Mater*. **2016**, 6, 1600137.

[117] C. Xu, B. Li, H. Du, F. Kang, *Angew. Chem., Int. Ed.* **2012**, 51, 933.

[118] D. Kundu, B. D. Adams, V. Duffort, S. H. Vajargah, L. F. Nazar, *Nat. Energy* **2016**, 1, 16119.

[119] B. Tang, L. Shan, S. Liang, J. Zhou, *Energy Environ. Sci.* **2019**, 12, 3288.

[120] M. Song, H. Tan, D. Chao, H. J. Fan, *Adv. Funct. Mater.* **2018**, 28, 1802564.

[121] Y. Zeng, X. Zhang, Y. Meng, M. Yu, J. Yi, Y. Wu, X. Lu, Y. Tong, *Adv. Mater.* **2017**, 29, 1700274.

[122] Z. Liu, Y. Huang, Y. Huang, Q. Yang, X. Li, Z. Huang, C. Zhi, *Chem. Soc. Rev.* **2020**, 49, 180.

[123] Z. Liu, Q. Yang, D. Wang, G. Liang, Y. Zhu, F. Mo, Z. Huang, X. Li, L. Ma, T. Tang, Z. Lu, C. Zhi, *Adv. Energy Mater.* **2019**, 9, 1902473.

[124] C. Xie, T. Li, C. Deng, Y. Song, H. Zhang, X. Li, *Energy Environ. Sci.* **2020**, 13, 135

[125] X.-B. Cheng, T.-Z. Hou, R. Zhang, H.-J. Peng, C.-Z. Zhao, J.-Q. Huang, Q. Zhang, *Adv. Mater.* **2016**, 28, 2888.

[126] H. S. Yang, J. H. Park, H. W. Ra, C.-S. Jin, J. H. Yang, *J. Power Sources* **2016**, 325, 446.

[127] G. Wang, B. Kohn, U. Scheler, F. Wang, S. Oswald, M. Löffler, D. Tan, P. Zhang, J. Zhang, X. Feng, *Adv. Mater.* **2020**, 32, 1905681.

[128] Q. Yang, G. Liang, Y. Guo, Z. Liu, B. Yan, D. Wang, Z. Huang, X. Li, J. Fan, C. Zhi, *Adv. Mater.* **2019**, 31, 1903778.

[129] Y. Liu, Q. Liu, L. Xin, Y. Liu, F. Yang, E. A. Stach, J. Xie, *Nat. Energy* **2017**, 2, 17083.

[130] R. Xu, X.-Q. Zhang, X.-B. Cheng, H.-J. Peng, C.-Z. Zhao, C. Yan, J.-Q. Huang, *Adv. Funct. Mater.* **2018**, 28, 1705838.

[131] H. Li, L. Ma, C. Han, Z. Wang, Z. Liu, Z. Tang, C. Zhi, *Nano Energy* **2019**, 62, 550.

[132] M. Ue, S. Mori, *J. Electrochem. Soc.* **1995**, 142, 2577.

[133] A. Ponrouch, R. Dedryvère, D. Monti, A. E. Demet, J. M. A. Mba, L. Croguennec, C. Masquelier, P. Johansson, M. R. Palacín, *Energy Environ. Sci.* **2013**, 6, 2361.

[134] K. Xu, *Chem. Rev.* **2004**, 104, 4303.

[135] J. Luo, S. He, T. L. Liu, *ACS Energy Lett.* **2017**, 2, 1197.

[136] D. Kundu, S. H. Vajargah, L. Wan, B. Adams, D. Prendergast, L. F. Nazar, *Energy Environ. Sci.* **2018,** 11, 881.

[137] M. He, K. C. Lau, X. Ren, N. Xiao, W. D. McCulloch, L. A. Curtiss, Y. Wu, *Angew. Chem.* **2016**, 55, 15310.

[138] C. M. Burke, V. Pande, A. Khetan, V. Viswanathan, B. D. McCloskey, *Proc. Natl. Acad. Sci. USA* **2015**, 112, 9293.

[139] G. Kamath, B. Narayanan, S. K. R. S. Sankaranarayanan, *Phys. Chem. Chem. Phys.* **2014**, 16, 20387.

[140] Y. Cheng, R. M. Stolley, K. S. Han, Y. Shao, B. W. Arey, N. M. Washton, K. T. Mueller, M. L. Helm, V. L. Sprenkle, J. Liu, G. Li, *Phys. Chem. Chem. Phys.* **2015**, 17, 13307.

[145] H. Li, Q. Yang, F. Mo, G. Liang, Z. Liu, Z. Tang, L. Ma, J. Liu, Z. Shi, C. Zhi, *Energy Storage Mater.* **2019**, 19, 94.

[169] X. Li, L. Ma, Y. Zhao, Q. Yang, D. Wang, Z. Huang, G. Liang, F. Mo, Z. Liu, C. Zhi, *Mater. Today Energy* **2019**, 14, 100361.

[204] C. Xu, J. Liao, C. Yang, R. Wang, D. Wu, P. Zou, Z. Lin, B. Li, F. Kang, C.-P. Wong, *Nano Energy* **2016**, 30, 900.

[205] M. C. H. McKubre, D. D. Macdonald, *J. Electrochem. Soc.* **1981**, 128, 524.

[206] Y. Ein-Eli, M. Auinat, D. Starosvetsky, *J. Power Sources* **2003**, 114, 330.

[207] G. Davies, A. G. Hsieh, M. Hultmark, M. E. Mueller, D. A. Steingart, *J. Electrochem. Soc.* **2016**, 163, A1340.

[208] B. Chopard, H. J. Herrmann, T. Vicsek, *Nature* **2018**, 353, 409.

[209] N. Ageta-Ishihara, T. Miyata, C. Ohshima, M. Watanabe, Y. Sato, Y. Hamamura, T. Higashiyama, R. Mazitschek, H. Bito, M. Kinoshita, *Nat. Commun.* **2013**, 4, 2532.

[210] E. R. White, S. B. Singer, V. Augustyn, W. A. Hubbard, M. Mecklenburg, B. Dunn, B. C. Regan, *ACS Nano* **2012**, 6, 6308.

[211] C. Brissot, M. Rosso, J. N. Chazalviel, S. Lascaud, *J. Power Sources* **1999**, 81, 925.

[212] V. Yufit, F. Tariq, D. S. Eastwood, M. Biton, B. Wu, P. D. Lee, N. P. Brandon, *Joule* **2019**, 3, 485.

[217] J. Park, A. Papoutsi, R. T. Ash, M. A. Marin, P. Poirazi, S. M. Smirnakis, *Nat. Commun.* **2019**, 10, 5372.

[218] X. Shi, G. Xu, S. Liang, C. Li, S. Guo, X. Xie, X. Ma, J. Zhou, *ACS Sustainable Chem. Eng.* **2019**, 7, 17737.

[219] P. Tan, B. Chen, H. Xu, H. Zhang, W. Cai, M. Ni, M. Liu, Z. Shao, *Energy Environ. Sci.* **2017**, 10, 2056.

[220] P. Pei, K. Wang, Z. Ma, *Appl. Energy* **2014**, 128, 315.

[221] S. Guo, H. Li, Y. Li, Y. Han, K. Chen, G. Xu, Y. Zhu, X. Hu, *Adv. Energy Mater.* **2018**, 8, 1800434.

[222] J.-C. Lai, X.-Y. Jia, D.-P. Wang, Y.-B. Deng, P. Zheng, C.-H. Li, J.-L. Zuo, Z. Bao, *Nat. Commun.* **2010**, 10, 1164.

[223] L. Zhang, Q. Lu, X. Lv, L. Shen, B. Zhang, Z. An, *Macromolecules* **2017**, 50, 2165.

[224] Y. Tang, Z. Zhao, X. Hao, Y. Wang, Y. Liu, Y. Hou, Q. Yang, X. Wang, J. Qiu, *J. Mater. Chem. A* **2017**, 5, 13591.

[225] Q. Yang, Z. Zhao, Y. Dong, Y. Liu, X. Liu, Y. Tang, Y. Wang, X. Wang, J. Qiu, *ChemElectroChem* **2017**, 4, 102.

[226] L. Kang, M. Cui, F. Jiang, Y. Gao, H. Luo, J. Liu, W. Liang, C. Zhi, *Adv. Energy Mater.* **2018**, 8, 1801090.

[227] W. Li, K. Wang, M. Zhou, H. Zhan, S. Cheng, K. Jiang, *ACS Appl. Mater. Interfaces* **2018**, 10, 22059.

[228] W. Li, K. Wang, M. Zhou, H. Zhan, S. Cheng, K. Jiang, *ACS Appl. Mater. Interfaces* **2018**, 10, 22059.

[229] C. Zhao, C. Yu, M. N. Banis, Q. Sun, M. Zhang, X. Li, Y. Liu, Y. Zhao, H. Huang, S. Li, X. Han, B. Xiao, Z. Song, R. Li, J. Qiu, X. Sun, *Nano Energy* **2017**, 34, 399.

[230] K. Zhao, C. Wang, Y. Yu, M. Yan, Q. Wei, P. He, Y. Dong, Z. Zhang, X. Wang, L. Mai, *Adv. Mater. Interfaces* **2018**, 5, 1800848.

[231] J. Hu, J. Ding, Z. Du, H. Duan, S. Yang, *J. Colloid Interface Sci.* **2019**, 555, 174.

[232] M. Cui, Y. Xiao, L. Kang, W. Du, Y. Gao, X. Sun, Y. Zhou, X. Li, H. Li, F. Jiang, C. Zhi, *ACS Appl. Energy Mater.* **2019**, 2, 6490.

[233] S. Y. Chung, S. Kim, J.-H. Lee, K. Kim, S.-W. Kim, C.-Y. Kang, S.-J. Yoon, Y. S. Kim, *Adv. Mater.* **2012**, 24, 6022.

[234] Y. Huang, M. Zhong, Y. Huang, M. Zhu, Z. Pei, Z. Wang, Q. Xue, X. Xie, C. Zhi, *Nat. Commun.* **2015**, 6, 10310.

[235] K. Liu, A. Pei, H. R. Lee, B. Kong, N. Liu, D. Lin, Y. Liu, C. Liu, P.-C. Hsu, Z. Bao, Y. Cui, *J. Am. Chem. Soc.* **2017**, 139, 4815.

[236] Š. Komorsky-Lovrić, V. Mirčeski, C. Kabbe, F. Scholz, *J. Electrochem. Soc*. **2004**, 566, 371

[237] Z. Zhao, J. Zhao, Z. Hu, J. Li, J. Li, Y. Zhang, C. Wang, G. Cui, *Energy Environ. Sci.* **2019**, 12, 1938.

[238] A. Mitha, A. Z. Yazdi, M. Ahmed, P. Chen, *ChemElectroChem* **2018**, 5, 2409.

[239] B.-S. Lee, S. Cui, X. Xing, H. Liu, X. Yue, V. Petrova, H.-D. Lim, R. Chen, P. Liu, *ACS Appl. Mater. Interfaces* **2018**, 10, 38928.

[240] Y. Huang, Z. Li, Z. Pei, Z. Liu, H. Li, M. Zhu, J. Fan, Q. Dai, M. Zhang, L. Dai, C. Zhi, *Adv. Energy Mater.* **2018**, 8, 1802288.

[241] K. Tang, A. Du, S. Dong, Z. Cui, X. Liu, C. Lu, J. Zhao, X. Zhou, G. Cui, *Adv. Mater.* **2020**, 32, 1904987.

[242] K. Hanai, T. Maruyama, N. Imanishi, A. Hirano, Y. Takeda, O. Yamamoto, *J. Power Sources* **2008**, 178, 789.

[243] A. J. Blake, R. R. Kohlmeyer, J. O. Hardin, E. A. Carmona, B. Maruyama, J. D. Berrigan, H. Huang, M. F. Durstock, *Adv. Energy Mater.* **2017**, 7, 1602920.

[244] Z. Wang, Z. Wu, N. Bramnik, S. Mitra, *Adv. Mater.* **2014**, 26, 970.

[245] R. Demir-Cakan, M. R. Palacin, L. Croguennec, *J. Mater. Chem. A* **2019**, 7, 20519.

[246] L. Sharma, K. Nakamoto, S. Okada, P. Barpanda, *J. Power Sources* **2019**, 429, 17.

[247] F. Mo, G. Liang, Q. Meng, Z. Liu, H. Li, J. Fan, C. Zhi, *Energy Environ. Sci.* **2019**, 12, 706.

[248] F. Wan, L. Zhang, X. Dai, X. Wang, Z. Niu, J. Chen, *Nat. Commun.* **2018**, 9, 1656.

[249] M. Kim, D. Yun, J. Jeon, *J. Power Sources* **2019**, 438, 227020.

[250] J. Hao, J. Long, B. Li, X. Li, S. Zhang, F. Yang, X. Zeng, Z. Yang, W. K. Pang, Z. Guo, *Adv. Funct. Mater.* **2019**, 29, 1903605.

[251] K. E. K. Sun, T. K. A. Hoang, T. N. L. Doan, Y. Yu, P. Chen, *Chem. Eur. J.* **2018**, 24, 1667.

[252] Q. Yang, Q. Li, Z. Liu, D. Wang, Y. Guo, X. Li, Y. Tang, H. Li, B. Dong, C. Zhi, *Adv. Mater.* **2020**, 32, 2001854.

[253] J. Zheng, D. C. Bock, T. Tang, Q. Zhao, J. Yin, K. R. Tallman, G. Wheeler, X. Liu, Y. Deng, S. Jin, A. C. Marschilok, E. S. Takeuchi, K. J. Takeuchi, L. A. Archer, *Nat. Energy* **2021**, 6, 398.

[254] Q. Zhang, J. Luan, L. Fu, S. Wu, Y. Tang, X. Ji, H. Wang, *Angew. Chem., Int. Ed.* **2019**, 58, 15841.

[255] L. Cao, D. Li, E. Hu, J. Xu, T. Deng, L. Ma, Y. Wang, X.-Q. Yang, C. Wang, *J. Am. Chem. Soc.* **2020**, 142, 21404.

[256] W. Yang, X. Du, J. Zhao, Z. Chen, J. Li, J. Xie, Y. Zhang, Z. Cui, Q. Kong, Z. Zhao, C. Wang, Q. Zhang, G. Cui, *Joule* **2020**, 4, 1557.

[257] Q. Zhao, S. Stalin, L. A. Archer, *Joule* **2021**, 5, 1119.

CHAPTER 3 Experimental Sections

3.1 Overview

The advanced techniques to characterize Zn dendrites and the structural features of the electrodes before and after battery operation were characterized by numerous techniques,

including X-ray diffraction technique (XRD), scanning electron microscopy (SEM). The structure features of the electrolytes were characterized by Fourier transform infrared (FTIR), Raman spectroscopy, nuclear magnetic resonance spectra. The electrochemcial performance was measured for the Zn electrode in AZIBs by Cyclic voltammetry, charge-discharge and electrochemcial impedance spectroscopy (EIS).

In-situ characterizations such as *Operando* synchrotron XRD and *in-situ* optical microscope were also conducted to investigate the structural changes of cathode and Zn dendrite growth during electrochemical cycling. Advanced techniques to characterize Zn dendrites and the as proposed protective approaches are important in obtaining insight into the inherent dendrite behaviors and assessing dendrite suppression performance. These advances are related to investigating the internal crystal and chemical structures of artificial interface layers and modified separators/electrolytes to detect structural stability when running the battery over long periods.

Visualization techniques such as optical microscopes vividly exhibit the topological evolution of Zn anodes. In addition, micromechanical properties are effective in measuring the tolerance of interface protections by physically shielding Zn dendrites. Furthermore, in contrast with organic and ionic liquid electrolytes, aqueous electrolytes are faced with the issue of pH change, which affects the surface properties of the Zn anode and the deposition behavior of Zn^{2+}. The pH change comes from hydrogen evolution at the surface of the metallic Zn anode. The generated OH^- reacts with Zn^{2+} and SO_4^{2-} to form inert ZHS, which attaches to the Zn anode and blocks the effective diffusion of Zn^{2+}. Hence, it is important to in

situ monitor the pH value of the aqueous electrolytes and develop protective strategies to sustain the pH stability of the electrochemical microenvironment.

The crystal and chemical structures of the material matrices are usually evaluated in a reversible or irreversible way because of repeated ion shuttles. Generally, prohibiting Zn dendrites requires mediating the ionic flow through spatial, electrostatic, or chemical interactions within the protective layers (interface layers, electrolytes, or separators). The possible distortion of crystal structures accompanies this ionic flow mediation because of spatial squeezing on the pore networks or directly on the crystalline matrixes. Once the threshold values have been surpassed, the originally robust chemical bonds will break down irreversibly. In the following section, we will discuss the use of advanced techniques, including operando/in situ XRD, Fourier transform infrared (FTIR) spectroscopy, Raman spectroscopy, X-ray photoelectron spectroscopy (XPS), and X-ray absorption fine structure (XAFS) in the field of dendrite protection.

Recent theoretical investigations into Zn dendrite protection mainly focus on simulating the electric field distribution and calculating the chemical adsorption energy of zinc atoms on substrates. These theoretical studies endeavor to reveal the origin of Zn dendrites from the perspective of inhomogeneous electric fields, which has been accepted as a basic theory. For further dendrite suppression, chemical adsorption computed by density functional theory (DFT) indicates the delicate approach of surface functionalization. Despite existing advancements, the only simulation of an electric field cannot directly reveal the fundamental issue behind the inhomogeneous distribution of Zn ions, which implies a future direction for the simulation methodology. Molecular dynamics (MD) are conducted to study the solvation

sheath of zinc ions and the diffusion pathway at the electrolyte–cathode interface, while applications emulating the ion diffusion process are still required.

3.2 Chemicals and materials

The chemicals and materials used in this work are listed in Table 3.1.

Table 3.1 Chemicals and materials used in this work.

Chemicals	Formula	Purity	Supplier
2-Pyrrolidinone	C_4H_7NO	99.9%	Adams
Acetylene black	C	Super P	TIMICAL
Copper foil	Cu	99.99%	Alfa Aesar
Gamma-butyrrolactone	$C_4H_6O_2$	99.9%	Adams
Titanium foil	Ti	99.99%	Alfa Aesar
Manganese (II) Sulfate Monohydrate	$MnSO_4 \cdot H_2O$	99.0%	Adams
Methyl sulfone	$C_2H_6O_2S$	99.9%	Adams
Sodium alginate	$C_5H_7O_4COONa$	99.9%	Adams
Zinc foil	Zn	99.99%	Alfa Aesar
Zinc sulfate heptahydrate	$ZnSO_4 \cdot 7H_2O$	99.0%	Adams

3.3 Material preparations

Preparation of Electrolyte: 2M $ZnSO_4$ aqueous electrolyte was prepared using $ZnSO_4 \cdot 7H_2O$ and DI based on molar ratio. GBL additive was introduced into the $ZnSO_4$ electrolyte at volume ratios of additive to water. For example, $ZnSO_4$-GBL electrolyte with volume ratio of 99:1, 97:3, and 95:5 were denoted as, respectively, 2MG1, 2MG3, and 2MG5. Similarly, the same additive content for GBL (GBL: H_2O = 99:1 vol/vol) with different concentration of zinc sulfate were prepared and denoted as yMG1 (y = 0.25, 0.5, 1 and 2). For electrolytes used in the full batteries, 0.5 M $MnSO_4$ was added to suppress dissolution of MnO_2.

Synthesis of β-MnO_2 [1]**:** 7.9 mg of $KMnO_4$ in 20 mL DI water and 50.7 mg of $MnSO_4 \cdot H_2O$ in 10 mL DI water were mixed under stirring for 60 min at room temperature (22 ^{O}C). The mixture was transferred into a 40 mL Teflon-lined autoclave and maintained at 140 °C for 24 h. The sediment was centrifuged, and washed thoroughly using water and/or ethanol several times before vacuum drying overnight (24 h).

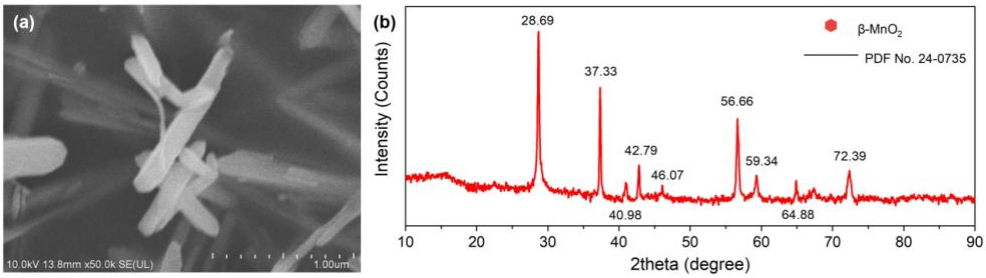

Figure 3.1 (a) SEM image and (b) XRD pattern of β-MnO_2 as synthesized.

Preparation of binder [2]**:** The binder was prepared with $CaCl_2$ and sodium alginate (SA). First, $CaCl_2$ was dissolved in deionized water to form a solution of 0.26 g L^{-1}. Then sodium alginate (SA) with a mass of 100 times of $CaCl_2$ was added and magnetic stirred overnight at room temperature. Then the binder was dried in a vacuum oven at 80°C for 12 h.

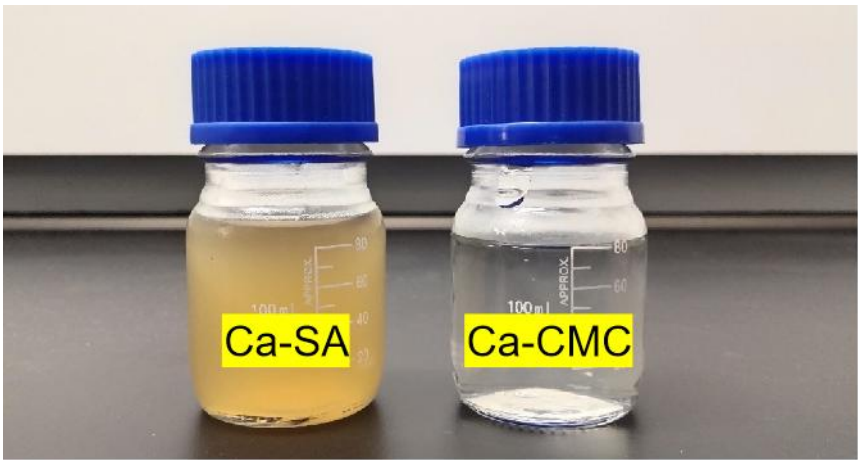

Figure 3.2 Image capture of binder samples: Ca-SA and Ca-CMC.

Cell configuration: Electrochemical performance was determined in CR2032-type coin cells and three-electrode devices. Cyclic voltammetry (CV) curves were tested with voltage range 0.95 to 1.85 V at a scan rate 1 mV s^{-1}. Electrochemical impedance spectra (EIS) were analyzed over frequency range 106 Hz to 10-2 Hz. Linear sweep voltammetry (LSV) was performed at a scan rate 1 mV s-1 using a three-electrode electrochemical cell. Electrochemical tests were conducted on an electrochemical workstation from CH Instruments, Inc. Zn cycling tests were performed on Zn||Zn symmetric cells in electrolytes with and without GBL additive. Coulombic efficiency (CE) was determined on Zn||Cu asymmetric cells. Practical application was evaluated by full cells based on MnO2 electrode and Zn-foil. Electrolyte was controlled at 150 μL. Symmetric and asymmetric tests were determined on the LAND battery testing system CT3001A from Wuhan LAND Electronic Co., Ltd.

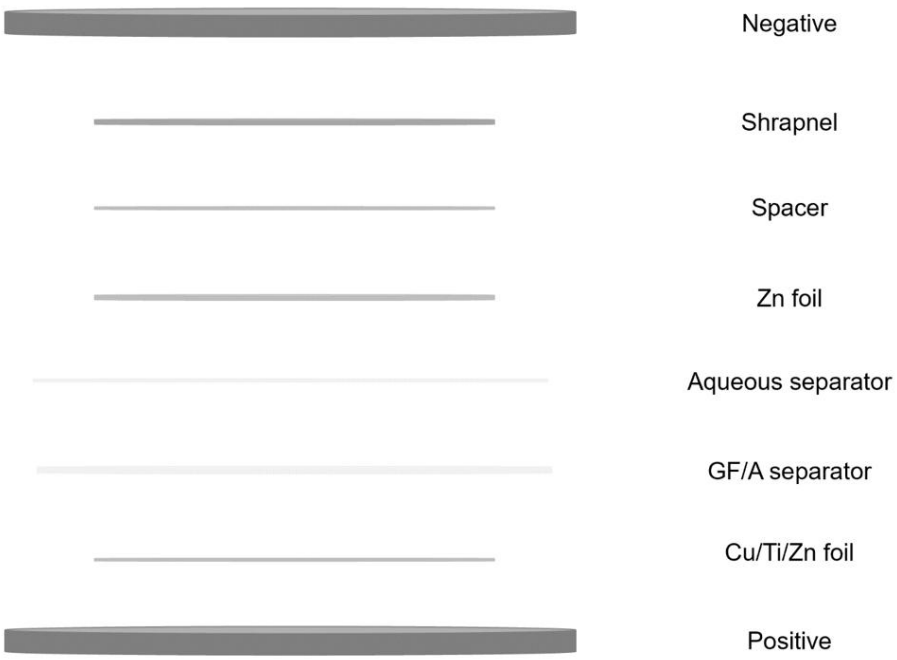

Figure 3.3 The components structure of Zn symmetric, half and full cells.

3.4 Characterizations

3.4.1 Fourier-transform Infrared spectroscopy (FT-IR)

FTIR spectroscopy based on the fingerprint adsorption of infrared signals due to certain vibrations of covalent bonds can effectively reveal information about chemical structures. FTIR is usually conducted at the external surface of electrodes or separators where the electrochemical processes are more active or intensive and the signal loss is reduced compared to the bulk phase. For dendrites, FTIR spectra at different discharging/charging states can provide information about the adsorbent species and intermediate products at the interface of the electrodes and electrolytes. [3, 4] Interface reactions such as gas generation (generally in neutral electrolytes) and electrolyte decomposition (e.g., HCSEs) in Zn batteries were determined by FTIR analysis to dramatically affect dendrite formation. [5-7] In addition, FTIR was used to probe the dendrite alleviation of PEG as an electrolyte additive. By observing the transmission intensity change during discharging/charging process, they found that the PEG molecules adsorb on the Zn surface during charging and desorb during discharging. This process is partially reversible with PEG accumulation during cycling. FTIR spectra can also detect the aggregation manner of water molecules among the HCSEs, where Zn plating proceeds in a dendrite-free way. The peak attributed to the hydrogen bond gradually fades away with the salt concentration increase and almost disappears at a salt concentration of 10 m. In another case, FTIR spectra were employed to characterize the chemical binding between ZnO and PVA/PDDA networks.[8] This composite anode remained the crosslink framework of PVA/PDDA with intensity changes in most functional bonds, while some other bonds exhibited a slight shift. In summary, FTIR spectroscopy is a serviceable tool for investigating the chemical interaction occurring on electrode/electrolyte interfaces at a molecular level. To be specific, interface engineering for electrode coating and electrolyte optimization can be profoundly understood using FTIR spectroscopy.

3.4.2 Raman spectroscopy

Raman spectroscopy, established based on the Raman effect between lasers and chemical bonds, reveals the chemical environments of materials. Both the chemical composition evolution within the electrodes and chemical interaction between electrolytes and electrodes can be monitored by the Raman spectroscopy.[9] Furthermore, Raman mapping, together with operando spectra records, enables visualization of the 2D distribution of chemical bonds along electrode surfaces.[10] With the sensitivity of the chemical bonds and composition, Raman is also a good option to comprehend the electrode and interface activities in optimizing the Zn anode. Typically, the leaf-like Zn dendrite was found to demonstrate apparent Raman shifts attributed to ZnO (E2, 436 cm-1) and surface optical phonons (502 cm-1).[11] In addition, Raman spectroscopy was also used to verify the role of PAM as an electrolyte additive to suppress dendrites.[12] It was found that acyl groups of PAM polymer chains were adsorbed on Zn electrodes, which showed a more intensive Raman signal due to surface-enhanced scattering. This surface-enhanced Raman technology was also applied for evaluating the triethyl phosphate electrolyte, which demonstrates that the deposits in aqueous electrolytes mainly contain Zn3(PO4)2 as a template for Zn uniform nucleation.[13] Raman spectroscopy is essential for detecting chemical composition evolution and physical adsorption behavior when studying the surface modification of a Zn anode.

3.4.3 ^{2}H nuclear magnetic resonance (NMR)

^{2}H nuclear magnetic resonance could be applied to the study of the environment of electrolyte system. The hydrogen bonding is analyzed by the ppm shift revealing the activity of water. Reflecting the relatives between water and Zn, we could deduce that the free water state and the evolution of [Zn^{2+}-6H_2O] solvation structure.

3.4.4 X-ray diffraction (XRD)

XRD is frequently applied to analyze the crystal structure of solid-state electrolytes, which are also developed to address the dendrite issues faced by metal batteries.[14] In contrast to previous ex situ ones, in situ XRD is established as a next-generation technique for monitoring the crystal structure transformation happening among in-service cells. It was initiated by detecting the structure/phase transformation of electrode materials and was recently extended to investigate dendrite suppression such as electrolyte additives and interphase engineering.[15, 16] In aqueous Zn batteries, Zn anodes are more easily studied than Li anodes in ambient conditions without the typical protection. These XRD-assisted studies imply a relationship between crystal transformation and dendrite morphology. Typically, operando XRD was reported to monitor the evolution of Zn sponge anodes coated with anion-exchange ionomers.[17] It revealed the gradual increase of the ZnO (002) peak, which suggests apparent phase transformation behavior. When capillary-type cell was used, in situ XRD recorded the real-time changes in the intensities of Zn (102) and ZnO (002) for different depths of anodes below the interface. The depletion or transformation of the Zn anode proceeded gradually from the surface to the bulk, while the reverse procedure of ZnO transformation happened in a similar way. Furthermore, computed tomography (CT) scanning was integrated into in situ XRD to study the transformation behavior of a leaflike Zn dendrite during the discharging/charging cycles.[18] As shown in Figures 5 and 17d, the (112) and (201) planes of the hexagonal Zn anode were drawn into an intensity-degree map in which the ZnO signal appears and then disappears during the redox process with high rechargeability. Despite intensive research using XRD to investigate the Zn/ZnO phase transformation, efforts devoted to the relationship between the crystal phase and dendrite morphology have thus far been insufficient. Many previous works suggest that the intensification of different crystallographic planes can serve as signals for distinct dendrite behaviors, enabling an indirect view of the surface morphology.

3.4.5 Scanning electron microscope (SEM)

Scanning electron microscope (SEM) is usually analyzed by observing the morphology of the active materials and the structure of the electrode. We usually could directly see the change of the surface or cross-section area of anode and cathode before and after cycling performance of symmetric, half and full batteries. Through this, we could conclude that the binder or the electrode structure could endure metal corrosion or strong mechanical strength during the electrochemical reaction if the structure was maintained even at high current density. Sometimes, SEM is co-used with element mapping or tunnel electron microscope (TEM) to confirm the inner structure and the element distribution.

3.4.6 In situ optical microscopy

The optical microscope, which performs magnification using visible light, is the oldest form of microscope. By simply constructing planar glass cells in ambient conditions, an operando optical microscope can monitor color and morphology evolution in situ at the micrometer scale at a low cost. This includes Zn dendrite growth and gas generation.[19, 20, 21] For instance, in confirming the protection of the GBL interface on the Zn anode, operando optical microscopy demonstrated outright that Zn protrusions appeared in an unprotected state after 15 min deposition, while the GBL-protected electrode maintained a smooth surface throughout a 30 min deposition.[22] In addition to the solid-state interface strategy, an optical microscope was also applied to analyze electrolyte modification by additives.[23] The operando optical microscope is the most accessible technique for the direct observation of the shape changes on the Zn metal surface at a micrometer scale. It provides long-range information instead of local morphology, which may change from location to location.

3.4.7 Contacting angle measurements

Contact angle measurement is used to affirm the distribution of the liquid phase on the surface of electrode. Sometimes, it is hydrophobic or zincophobic, because the terminal

groups are most of hydrogen or alkyl chains. Another side, if the terminal groups are most of oxygen or other polar functional groups, the surface or binding energy would be changed, contributing to the interface modification of electrolyte electrode interphase.

3.5 Theoretical calculations

3.5.1 Ab-initio (VASP) simulations

The computations for molecules adsorb on Zn-slab were carried out *via* Vienna *ab-initio* simulation package (VASP) with projector augmented wave (PAW) potential for electrons and GGA for exchange and correlation functional of Perdew-Burke-Ernzerhof (PBE) form [24]. An energy cut-off of 450 eV was used for the plane wave expansion of valence electron wave functions. The simulated Zn supercell of 5 × 5 × 1 and Brillouin zone was sampled using a k-point mesh of Γ-centered 2 × 2 × 1 for structure optimization. A vacuum layer of 30 Å was introduced to avoid periodic interactions. The structures were relaxed with the atoms allowed to move until the force on each was < 0.03 eV/Å.

The chemisorption interaction between Zn atom and substrate functions as an antagonistic factor of the inhomogeneous electric field to realize an even state for a Zn ion concentration field.

The corresponding quantification of chemisorption is based on adsorption energy computation using the DFT method. This chemisorption computation can effectively depict the diffusion pathway and the accompanied energy-barrier distribution of zinc ions migrating in the matrix of solid-state electrolytes and the artificial interface layer. [25, 26] Distinct from the electric field simulation proceeding after the zinc nucleation step, chemisorption computation is mainly employed at the ion diffusion stage before plating, at which point the diffusion direction can be subtly guided. Recently, chemisorption energy calculations were conducted to screen out appropriate conductive substrates from copper, $CuZn_5$ alloy, brass, nickel, graphene nanoribbon, zinc, and PAM chains for dendrite-free substrate design.[27] The weak interaction between Zn atoms and the Zn substrate was determined to be as low as

-0.68 eV, which was proposed to be one of the origins for dendrite formation. Despite being different from previous hypotheses regarding lattice mismatch, this weak chemisorption drives us to rethink the primary cause for Zn dendrite formation.[28] Different crystal planes of the same substrates, including Zn metal, are thought to exhibit distinct chemisorption for Zn atoms.[29, 30] In addition, the intensive chemisorption (-1.25 eV) from acyl groups of PAM inspired us to mediate the zinc ion flow via introducing polar functional groups onto the interface layer, Zn anode, or current collector.[31] Pure CFs were revealed by DFT calculation to be unsuitable as Zn plating substrates owing to a limited binding energy of only -0.34 eV.[32] This issue was addressed by heteroatom doping, which can regulate the electronic structure and supply active sites for Zn nucleation.[33, 34] Specifically, CFs were treated with concentrated nitric acid at 80 °C to functionalize the surface with N- and O-containing functional groups to tune the surface binding energy of Zn on CFs. Remarkably, the chemisorption energies were successfully increased up to 1.59 and 3.03 eV for N-doping and O-doping CFs, respectively. These improved chemisorption interactions are accompanied by the charge transfer between Zn atoms and the substrate atoms. Chemisorption energy computation clarifies the desired properties of Zn anodes and the conductive substrates, which indicates a clear route for designing advanced anodes of ZMBs.

3.5.2 Quantum Chemistry Calculations

Density functional theory (DFT) simulation was performed using Gaussian09 software package. $ZnSO_4$, organic molecules and H_2O molecules were using the B3LYP functional. Lanl2DZ basis set was used for Zn and 6-31+G(d, p) for other elements. HOMO and LUMO orbits and electrostatic surface potential (ESP) were rendered using GaussView software.

3.5.3 Molecular Dynamic (MD) Emulations

Molecular Dynamics (MD) emulation of the two electrolyte-systems was determined using Gromacs package.[35] OPLS-2009IL force field parameters were used for SO_4^{2-} and

$C_4H_6O_2$. [36], and a charge scaling of 0.8 was applied to mimic polarization. SPC/E force field was used for, respectively, water molecules, and amber force field parameter for Zn ions. The box-size for simulation was about 25×25×25 $Å^3$ and the ratio of $ZnSO_4$, $C_4H_6O_2$ and H_2O 300:15:5500, together with periodic boundary conditions that were applied in all directions. The structures were relaxed by energy minimizing simulation, particle-mesh Ewald method with a cut-off distance of 10 Å applied to treat electrostatic, and van der Waals, interactions. The velocity-rescale thermostat [37] was used to control temperature to 298.15 K. Berendsen's barostat was used at NPT ensemble to control pressure [38]. An MD simulation for a total time of 20 ns was performed with time-step set to 0.2 ps during simulation.

MD emulation exhibits enormous potential in simulating the ion diffusion process at the micrometer scale to investigate dendrite formation and search for protection strategies. By incorporating electric fields, force fields, spatial interactions, and electrostatic interactions into the emulation system, MD is able to improve the simulation accuracy. [39-41] The migration behavior of zinc ions emulated by MD thus represents vector interactions of spatial confinement (pore structure and crystal matrix), localized electrostatic repulsion/adsorption (surface charge), and external electric field (potential difference). Motivated by the above advantages, MD emulation is thought to offer new technique for understanding the zinc ion diffusion process across the electrolyte–artificial protective layer interface, the bulky artificial protective layer, and the artificial protective layer–electrode interface. For ZMBs, MD emulation initially focused on investigating the solvation sheath of zinc ions in the HCSEs to elucidate the reason behind the highly reversible Zn plating/stripping behavior.[42] The force-field-based MD simulations reveal the dynamic components of the solvation sheath of zinc ions, which is determined by the competition between bulky anions (TFSI-) and water when coordinating with zinc ions. Specifically, Zn2+ tends to coordinate with water molecules (rather than TFSI-) under low electrolyte concentration (<5 m), while $TFSI^-$ is the dominant component of the solvation sheath when dramatically increasing the electrolyte concentration to 20 m. This component evolution of solvation sheaths effectively illustrates the reversibility of the Zn anode. However, the detailed desolvation manner of Zn^{2+} before

being reduced is still unclear [43] regarding where and how the desolvation happens or the existence of any relationship between desolvation and the concentration distribution. MD emulation is thought to play a significant role in solving these issues.

MD simulation was also reported to elucidate ion diffusion behavior and its dependence on the solvents of Zn hybrid batteries.[44] The coordination process of water with ions is an inverse process of the desolvation of Zn^{2+}, which is an essential step before Zn deposition. Thus, researchers can utilize MD simulation to investigate desolvation behavior and get an insight into the dendrite-free Zn deposition. In addition, this MD simulation also provides new information about dendrite suppression using electrolyte additives.[45, 46] Despite the significant progress, the limited numbers of atoms in this MD simulation cannot efficiently reflect the group behavior of zinc ion diffusion. The high flux computation capability desired by researchers for MD simulations has been evidenced by our work regarding the water-holding capacity of gel electrolytes in ZMBs.[47] In addition, MD emulation can also visualize the ion diffusion driven by both localized electrostatic interactions and macroscopic electrical fields.[48] This enables researchers to explore the ion migration behavior among interconnected pores (positively/ negatively charged ion tunnels of gel electrolytes), adjacent nanolayers (2D nanomaterials), and interstitial voids (ion superconducting type materials).

3.6 Electrochemical measurements

3.6.1 Cyclic voltammetry (CV)

Cyclic voltammetry method is applied to detect the redox reaction and the reversible electrochemical reaction of various kinds of active materials such as MnO2 and V_2O_5 etc. Also we could get the specific capacitance (C_p, F g^{-1}) through the integrated absolute area of closed CV curves. By setting different scan rate (v, mV s^{-1}) or we know the kinetics transfer method, we could plot a series curves of CV curves which the position of redox peaks would be shifted because the charge transfer and diffusion kinetics are different for various kinds of

active materials. After linear fitting of peak currents and the square root of scan rates; log (i) vs. log (v) at different potentials; plot of $v^{1/2}$ vs. $I/v^{1/2}$ at different redox states for obtaining constant k_1 and k_2; capacitive and diffusion-controlled capacitive at different scan rate.

3.6.2 Galvanostatic charge/discharge curves

Galvanostatic charge/discharge curves is applied to affirm the electrode redox state or crystallization phase of materials in half or full cells that reflects the Coulombic efficiency, nucleation potential and also could modify the capacity through N/P ratio. To further study the electrochemical process, the battery test system could be used together with X-ray diffraction (XRD) (*in-situ* XRD) which could confirm the different crystalline phase corresponding to different potentials.

3.6.3 Linear Sweep voltammetry (LSV)

Linear sweep voltammetry (LSV) method is applied to test the HER part

3.6.4 Polarization curve test

The polarization curve is divided into four regions, the active dissolution region, the transition passivation region, the stable passivation region, and the overpassivated region. The polarization curve can be measured experimentally. Analyzing and studying the polarization curve is one of the basic methods to explain the behaviors of Zn metal corrosion, reveal the mechanism of metal corrosion and explore the control of corrosion pathways.

3.6.5 Electrochemical impedance spectroscopy (EIS)

Electrochemical impedance spectroscopy studies the mechanisms of electrode material, solid electrolyte, conductive polymer and corrosion protection by measuring the change of impedance with the frequency of the sine wave, and then analyzing the electrode process kinetics, double layer and diffusion.

References

[1] L. Cao, D. Li, T. Pollard, T. Deng, B. Zhang, C. Yang, L. Chen, J. Vatamanu, E. Hu, M.J. Hourwitz, L. Ma, M. Ding, Q. Li, S. Hou, K. Gaskell, J. T. Fourkas, X.-Q. Yang, K. Xu, Q. Borodin, C.S. Wang. *Nat. Nanotechnol.* **2021**, 8, 902-910.

[2] D. Xie, J. Zhao, Q. Jiang, H. Wang, H. Huang, P. Rao, J. Mao, *Chemphyschem*. **2022**.

[3] A. Vizintin, J. Bitenc, A. K. Lautar, K. Pirnat, J. Grdadolnik, J. Stare, A. Randon-Vitanova, R. Dominko, *Nat. Commun.* **2018**, 9, 661.

[4] J.-T. Li, Z.-Y. Zhou, I. Broadwell, S.-G. Sun, Acc. Chem. Res. 2012, 45, 485.

[5] Y. Yang, X. Liu, Z. Dai, F. Yuan, Y. Bando, D. Golberg, X. Wang, Adv. Mater. 2017, 29, 1606922.

[6] B. M. Koo, D. A. D. Corte, J.-N. Chazalviel, F. Maroun, M. Rosso, F. Ozanam, Adv. Energy Mater. 2018, 8, 1702568.

[7] Q. Zhao, W. Huang, Z. Luo, L. Liu, Y. Lu, Y. Li, L. Li, J. Hu, H. Ma, J. Chen, Sci. Adv. 2018, 4, eaao1761.

[8] W. Gan, D. Zhou, L. Zhou, Z. Zhang, J. Zhao, Electrochim. Acta 2015, 182, 430.

[9] L. Dong, W. Yang, W. Yang, H. Tian, Y. Huang, X. Wang, C. Xu, C. Wang, F. Kang, G. Wang, Chem. Eng. J. 2020, 384, 123355.

[10] E. Shangguan, P. Fu, S. Ning, C. Wu, J. Li, X. Cai, Z. Wang, M. Wang, X. Li, Q. Li, J. Power Sources 2019, 422, 145.

[11] P. K. Samanta, A. K. Bandyopadhyay, S. Basak, P. R. Chaudhuri, Optik 2011, 122, 1520.

[12] M. Li, Q. He, Z. Li, Q. Li, Y. Zhang, J. Meng, X. Liu, S. Li, B. Wu, L. Chen, Z. Liu, W. Luo, C. Han, L. Mai, Adv. Energy Mater. 2019, 9, 1901469.

[13] A. Naveed, H. Yang, J. Yang, Y. Nuli, J. Wang, Angew. Chem., Int. Ed. 2019, 131, 2786.

[14] F. Moser, F. Fourgeot, R. Rouget, O. Crosnier, T. Brousse, Electrochim. Acta 2013, 109, 110.

[15] D. Liu, Z. Shadike, R. Lin, K. Qian, H. Li, K. Li, S. Wang, Q. Yu, M. Liu, S. Ganapathy, X. Qin, Q.-H. Yang, M. Wagemaker, F. Kang, X.-Q. Yang, B. Li, Adv. Mater. 2019, 31, 1806620.

[16] S. Liu, M. Wang, X. Sun, N. Xu, J. Liu, Y. Wang, T. Qian, C. Yan, Adv. Mater. 2018, 30, 1704898.

[17] D. Stock, S. Dongmo, K. Miyazaki, T. Abe, J. Janek, D. Schröder, J. Power Sources 2018, 395, 195.

[18] A. Nakata, H. Murayama, K. Fukuda, T. Yamane, H. Arai, T. Hirai, Y. Uchimoto, J.-I. Yamaki, Z. Ogumi, Electrochim. Acta 2015, 166, 82.

[19] H. S. Yang, J. H. Park, H. W. Ra, C.-S. Jin, J. H. Yang, J. Power Sources 2016, 325, 446.

[20] M. Chamoun, B. J. Hertzberg, T. Gupta, D. Davies, S. Bhadra, B. Van Tassell, C. Erdonmez, D. A. Steingart, NPG Asia Mater. 2015, 7, e178.

[21] P.-C. Hsu, S.-K. Seol, T.-N. Lo, C.-J. Liu, C.-L. Wang, C.-S. Lin, Y. Hwu, C. H. Chen, L.-W. Chang, J. H. Je, G. Margaritondo, J. Electrochem. Soc. 2008, 155, D400.

[22] Z. Zhao, J. Zhao, Z. Hu, J. Li, J. Li, Y. Zhang, C. Wang, G. Cui, Energy Environ. Sci. 2019, 12, 1938.

[23] S. J. Banik, R. Akolkar, J. Electrochem. Soc. 2013, 160, D519.

[24] J. Zheng, Q. Zhao, T. Tang, J. Yin, C. D. Quilty, G. D. Renderos, X. Liu, Y. Deng, L. Wang, D. C. Bock, C. Jaye, D. Zhang, E. S. Takeuchi, K. J. Takeuchi, A. C. Marschilok, L. A. Archer, Science 2019, 366, 645

[25] F. Costanzo, P. L. Silvestrelli, F. Ancilotto, *J. Chem. Theory Comput.* **2012**, 8, 1288.

[26] Q. He, B. Yu, Z. Li, Y. Zhao, *Energy Environ. Mater.* **2019**, 2, 264.

[27] M. Li, Q. He, Z. Li, Q. Li, Y. Zhang, J. Meng, X. Liu, S. Li, B. Wu, L. Chen, Z. Liu, W. Luo, C. Han, L. Mai, *Adv. Energy Mater.* **2019**, 9, 1901469.

[28] K. E. K. Sun, T. K. A. Hoang, T. N. L. Doan, Y. Yu, P. Chen, *Chem. Eur. J.* **2018**, 24, 1667.

[29] Y. Zhou, D. E. Doronkin, M. Chen, S. Wei, J.-D. Grunwaldt, *ACS Catal.*, 6, 7799.

[30] W. Zou, B. Deng, X. Hu, Y. Zhou, Y. Pu, S. Yu, K. Ma, J. Sun, H. Wan, L. Dong, *Appl. Catal.*, **B** 2018, 238, 111.

[31] T. Greber, Ž. Šljivančanin, R. Schillinger, J. Wider, B. Hammer, *Phys. Rev. Lett.* **2006**, 96, 056103. Adv. Energy Mater 2019, 9, 19013434343

[32] Q. Guan, Y. Li, X. Bi, J. Yang, J. Zhou, X. Li, J. Cheng, Z. Wang, B. Wang, J. Lu, Adv. Energy Mater. 2019, 9, 1901434.

[33] Z. Pei, H. Li, Y. Huang, Q. Xue, Y. Huang, M. Zhu, Z. Wang, C. Zhi, Energy Environ. Sci. **2017,** 10, 742.

[34] Y. Lu, Z. Li, Z. Bai, H. Mi, C. Ji, H. Pang, C. Yu, J. Qiu, *Nano Energy* **2019**, 66, 104132.

[35] A. Bernardi, R. Faller, D. Reith, K. N. Kirschner, *Softwarex* **2019**, *10*, 100241.

[36] a) W. L. Jorgensen, J. Tirado-Rives, *Proc. Natl. Acad. Sci. U.S.A.* **2005**, *102*, 6665;

b) L. S. Dodda, J. Z. Vilseck, J. Tirado-Rives, W. L. Jorgensen, *J. Phys. Chem. B* **2017**, *121*, 3864-3870.

[37] G. Bussi, D. Donadio, M. Parrinello, *J. Chem. Phys.* **2007**, *126*, 014101.

[38] H. J. C. Berendsen, J. P. M. Postma, W. F. van Gunsteren, A. DiNola, J. R. Haak, *J. Chem. Phys.* **1984**, *81*, 3684-3690.

[39] a) P. E. Blöchl, *Phys. Rev. B* **1994**, *50*, 17953-17979; b) B. Hammer, L. B. Hansen, J. K. Nørskov, *Phys. Rev. B* **1999**, *59*, 7413-7421; c) G. Kresse, D. Joubert, *Phys. Rev. B* **1999**, *59*, 1758-1775; d) J. Tao, J. P. Perdew, V. N. Staroverov, G. E. Scuseria, Phys. Rev. Lett. **2003**, *91*, 146401; e) S. Lebègue, O. Eriksson, *Phys. Rev. B* **2009**, *79*, 115409.

[39] Y.-L. Zhu, Z.-Y. Lu, G. Milano, A.-C. Shi, Z.-Y. Sun, Phys. Chem. Chem. Phys. **2016**, 18, 9799.

[40] F. Song, B. Ma, J. Fan, Q. Chen, B. Q. Li, Langmuir 2019, 35, 9753.

[41] K. Yoshida, D. Kuroda, M. Kiyoshi, M. Nakakido, S. Nagatoishi, S. Soga, H. Shirai, K. Tsumoto, *Sci. Rep.* **2019**, 9, 4482.

[42] F. Wang, O. Borodin, T. Gao, X. Fan, W. Sun, F. Han, A. Faraone, J. A. Dura, K. Xu, C. Wang, *Nat. Mater.* **2018**, 17, 543.

[43] J. Xiao, *Science* **2019**, 366, 426.

[44] J. Hao, J. Long, B. Li, X. Li, S. Zhang, F. Yang, X. Zeng, Z. Yang, W. K. Pang, Z. Guo, *Adv. Funct. Mater.* **2019**, 29, 1903605.

[45] N. Li, W. Wei, K. Xie, J. Tan, L. Zhang, X. Luo, K. Yuan, Q. Song, H. Li, C. Shen, E. M. Ryan, L. Liu, B. Wei, *Nano Lett.* **2018**, 18, 2067.

[46] J. Zheng, M. H. Engelhard, D. Mei, S. Jiao, B. J. Polzin, J.-G. Zhang, W. Xu, *Nat. Energy* **2017**, 2, 17012.

[47] Y. Huang, Z. Li, Z. Pei, Z. Liu, H. Li, M. Zhu, J. Fan, Q. Dai, M. Zhang, L. Dai, C. Zhi, *Adv. Energy Mater.* **2018**, 8, 1802288.

[48] F. Ding, W. Xu, G. L. Graff, J. Zhang, M. L. Sushko, X. Chen, Y. Shao, M. H. Engelhard, Z. Nie, J. Xiao, X. Liu, P. V. Sushko, J. Liu, J. Zhang, *J. Am. Chem. Soc.* **2013**, 135, 4450.

CHAPTER 4 MSM as Electrolyte Additives for aqueous Zn-ion Batteries

4.1 Introduction

To achieve the target of carbon neutrality by 2050, it requires the massive deployment of all available clean energy technologies – such as renewables, EVs and energy efficient building retrofits. Energy storage plays a key role across almost all the energy sectors, from consume electronics, transport and smart grid to industry. Li-ion batteries have dominated in the energy storage field, but still suffers the high cost and low safety.[1,2] Aqueous rechargeable zinc batteries (AZIBs) have recently attracted strong attention for large-scale energy storage due to their advantages of high safety, low toxicity, abundance of materials, and the unique features of zinc: low redox potential (-0.7626 V vs. standard hydrogen electrode), high gravimetric capacity (820 mA h g-1) and high volumetric capacity (5585 mAh cm-3).[3-6] However, there are still critical issues related to Zn metal anodes, such as Zn dendrites, corrosion, by-product and H2 evolution should be overcome to achieve high reversibility and stability.

The electrochemical behavior of Zn metal is largely determined by the properties of aqueous electrolytes and electrode-electrolyte interfaces, which are closely related to the solvation structures of hydrated Zn2+ ions, anions, and hydrogen bonding network. Therefore, simultaneously reconstructing the chemical bonding network and solvation structures of cations and anions in aqueous electrolyte and optimizing the electrode-electrolyte interface on Zn metal surface is an effective strategy to regulate the performance of Zn anodes. Several electrolyte formulations including high concentration, [7-9] water-in-eutectic, [10-14] and aqueous/organic hybrid electrolytes [15-18] have been proposed to tune the solvation structure of electrolyte and improve the reversibility of Zn anodes. However, new problems arise from these electrolytes including a high cost, low ionic conductivity and high viscosity.

In contrast, the introduce of organic additive has been considered as a promising approach, because the organic species (liquids, solids) could interact with Zn2+ and H_2O molecules to modulate the solvated structure of Zn hydration and the hydrogen bonding network without high concentration of slats or solvents.[19-29] However, the electrochemical performance of Zn anodes in these reports still remains poor especially under the harsh condition of high current density/capacity up to 10 mA cm^{-2} and 10 mAh cm^{-2}. In addition, some organic molecules are highly flammable. Although the nonflammable nature of water undergirds the overall safety of AZIBs, the hydrogen evolution reaction (HER) or oxygen evolution reaction (OER) of water during battery cycling or idling not only lowers the Coulombic efficiency (CE) and cycle life but also causes serious safety concerns over explosion. The solutions for AZIBs must effectively suppress these parasitic reactions to the extent and do not cause a safety concern. Therefore, seeking a nonflammable or low vapour pressure solvent is highly recommended to regulate the solvation structure and interface for improving the reversibility and stability of Zn anode under harsh test conditions.

Because methylsulfonylmethane (MSM) has a high boiling and flash temperature, respectively, T_b = 240.9 ± 8.0 °C and T_f = 143.3 ± 0.0 °C, and a high dielectric constant e = 47.39 and dipole moment 4.44 D, it is practically attractive as an electrolyte additive for rechargeable batteries. MSM-based electrolytes have in fact been used in Li-ion batteries over a range of temperature. [30,31]

Here MSM was adopted as a new electrolyte additive to $ZnSO_4$ electrolyte. It was postulated that through adjusting the mole ratio of MSM in MSM-based electrolytes, 0.9M MSM (maximum of the solubility which was stirred at room temperature), in 2 M $ZnSO_4$ would significantly boost Zn plating/stripping performance under different current density. Experiment and theoretical computation confirmed that the functional MSM additive weakens the bonding strength between Zn^{2+} ion and solvated H_2O and rearranges the 'Zn^{2+}−H_2O−SO_4^{2-}−MSM' bonding-network to reduce water activity and suppress corrosion and generation of by-product. The Zn metal surface absorbs MSM rather than H_2O which restricts uncontrollable 2D diffusion and gives rise to uniform deposition. Thus, the Zn-MnO_2

full cells using $ZnSO_4$-MSM electrolyte exhibited superior performance to that using MSM-free electrolyte. Importantly, because 2 M $ZnSO_4$-MSM electrolyte is nonflammable it makes AZIBs practically promising for large-scale application.

4.2 Results and Discussion

4.2.1 Stability of the Zn Electrode

The stability of the Zn electrode in aqueous electrolyte with and without MSM was compared in Zn||Zn symmetric cells, Figure 4.1a-c (Figure 4.2). MSM addition resulted in excellent stability of Zn in Zn||Zn in normal to harsh condition. With an optimized electrolyte of 2 M $Zn(SO_4)_2$ with 0.9M MSM in amount (2MS0.9), the Zn symmetrical cell exhibited highly stable cycling performance for over 1200 h at a current density of 1 mA cm^{-2} and an areal capacity of 1 mA h cm^{-2}, significantly however, the 2M $ZnSO_4$ electrolyte failed following 700 h, Figure 1a. Under harsh conditions of 5 mA cm^{-2} and 5 mA h cm^{-2}, the Zn electrode with 2MS0.9 electrolyte remained stable and exhibited reversible Zn plating/stripping for 456 h. Importantly, this is significantly longer than that in the blank electrolyte of 70 h. These findings strongly evidence the significant boost in reversibility and stability of the Zn anodes resulting from MSM addition.

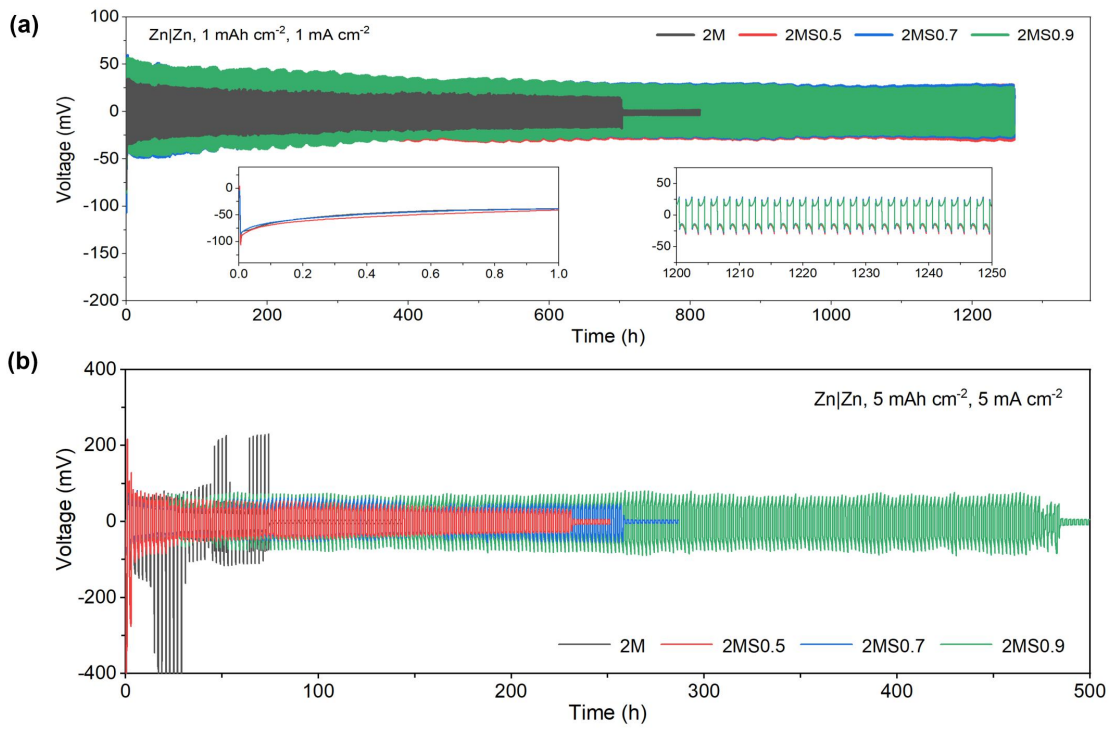

Figure 4.1 Zn|Zn symmetric cells containing 2M $ZnSO_4$ with different amount of MSM at the areal capacity and current density of (a) 1 mAh cm^{-2} at 1 mA cm^{-2}; (b) 5 mAh cm^{-2} at 5 mA cm^{-2}.

4.2.2 Reversibility of the Zn Electrode

Reversibility of the Zn electrode in aqueous electrolyte with and without MSM was compared in Zn||Cu asymmetric cells, Figure 4.2a-e. It was found that there are marginal differences in the initial Coulombic efficiency, that increases with increasing $ZnSO_4$ concentration i.e. 2MS0.9 > 2MS0.7 > 2MS0.5 > 2M (Figure 4.2). The addition of less MSM, reduced the initial Coulombic efficiency. The presence of 0.9M MSM boosted the initial Coulombic efficiency to 98 % at 1 mA cm^{-2} and 1 mA h cm^{-2}, and the average CE increased to 99.9 % for over 900 cycles (1800 h), Figure 4.2a. In comparison, the 2 M $ZnSO_4$ electrolyte exhibited a low initial Coulombic efficiency of 91.1 % and an average CE of 99.6 %, noticeably failing at the 222th cycle, Figures 4.2d, 4.2e.

Addition of MSM concomitantly tuned Zn deposition morphology and suppressed corrosion. The **scanning electron microscopy (SEM)** images confirmed that following 50

cycles with Zn||Cu cells, the Zn surface in the $ZnSO_4$ electrolyte become an apparent scattered microporous structure, Figure 4.2b, whilst there remained a plain stage structure on the Zn surface in the $ZnSO_4$-MSM electrolyte; this formed a uniform planar stage for dendrite formation, Figure 4.2c. A reduced hydrogen and oxygen evolution current obtained from linear sweep voltammetry (LSV) curves confirm the impact on boosting reversibility and stability *via* controlled manipulation with MSM additive (Figure 4.3).

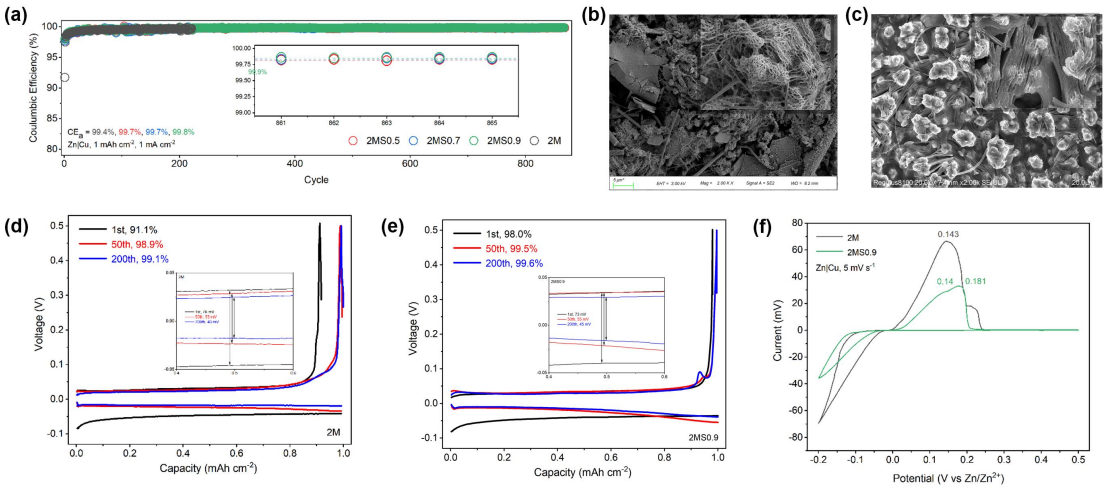

Figure 4.2 Zn|Cu half cells performance and properties. (a) Coulombic efficiency of the cells in 2 M $ZnSO_4$ electrolytes with different amount of MSM. The half cells after 50 cycles at 1 mAh cm^{-2} at 1 mA cm^{-2}. SEM images of the Zn foils in (b) 2M and (c) 2MS0.9 electrolytes for half cells after 50 cycles. Charge/discharge voltage profiles of half cells with (d) 2M and (e) 2MS0.9 electrolytes at 1st, 50th and 200th cycles with magnified views of corresponding cycles in the potential range between 0.4 and 0.6 V at a current density of 1 mA cm^{-2}. (f) Cyclic voltammetry at 5 mV s^{-1}.

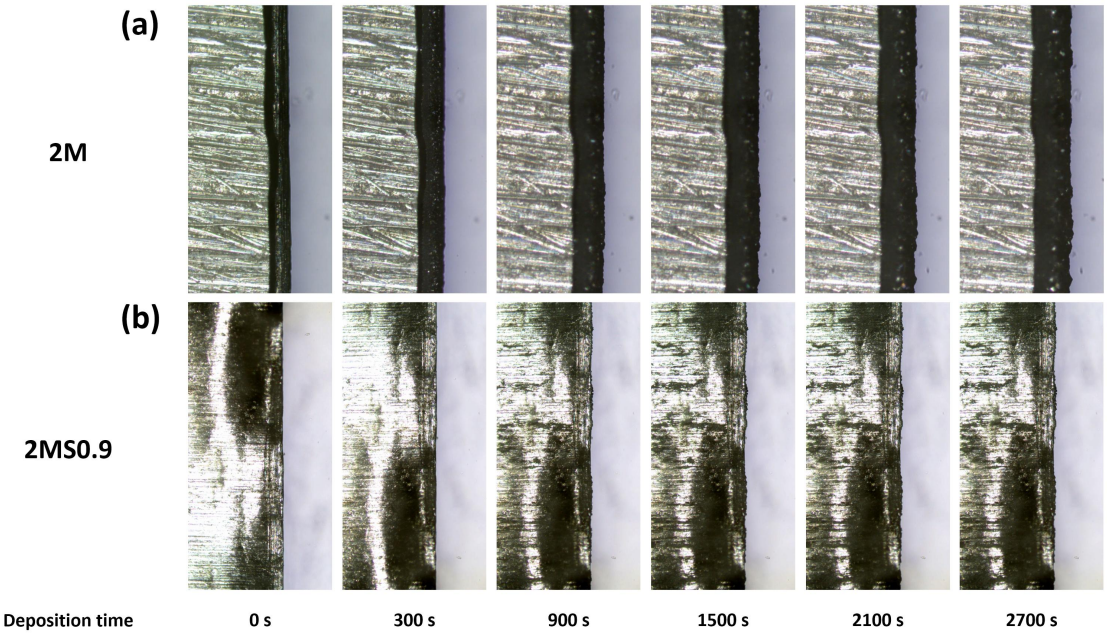

Figure 4.3 *In-situ* optical microscopic images for Zn deposition process at the current density of 5 mA cm^{-2}.

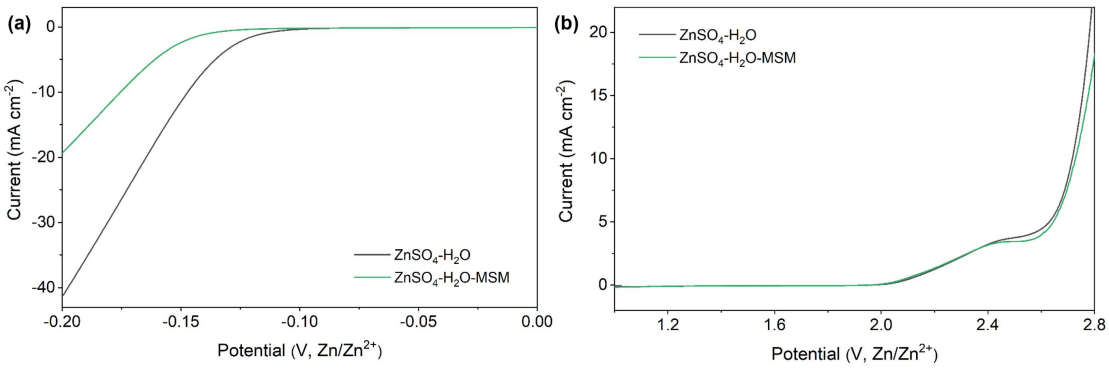

Figure 4.4 (a) Anodic and (b) cathodic LSV response curves for aqueous $ZnSO_4$ and $ZnSO_4$-MSM electrolyte at 1 mV s^{-1}.

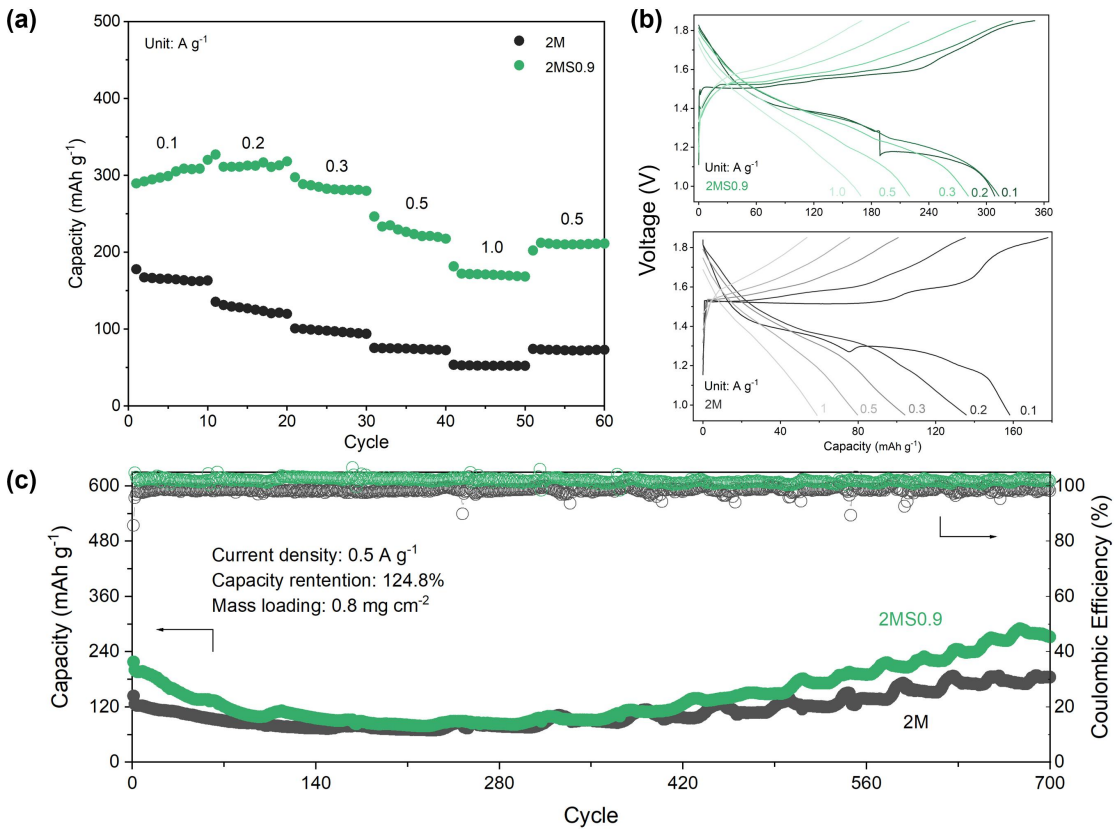

Figure 4.5 Zn|MnO_2 full cells performance. (a) Rate capability at 0.1, 0.2, 0.3, 0.5, 1 A g^{-1} and back to 0.5 A g^{-1}; (b) Galvanostatic Charge Discharge (GCD) profiles at different current density 0.1, 0.2, 0.3, 0.5 and 1 A g^{-1}; and (c) Cycle performance at 0.5 A g^{-1}.

4.2.3 Chemical and physical properties of electrolytes

Judiciously combined experimental characterizations including Fourier transform infrared spectroscopy (FTIR) and Raman spectroscopy were used to determine the underlying mechanism for Zn metal in $ZnSO_4$-MSM. The addition of MSM weakens the solvation coordination between Zn^{2+} and water. This finding was confirmed *via* FTIR (Figure 4.7) and Raman (Figure 4.8) results. Compared with pure MSM, the C-H stretching moves to lower wave number in $ZnSO_4$-MSM caused by interaction between MSM and water.

Figure 4.6 Image captures of 1M / 2M $ZnSO_4$ with different amount of MSM.

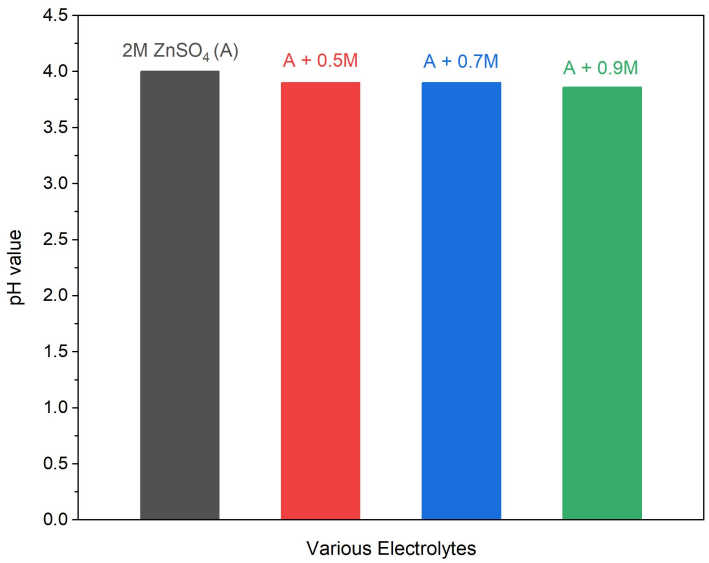

Figure 4.7 pH value of 2M, 2MS0.5, 2MS0.7 and 2MS0.9 electrolytes.

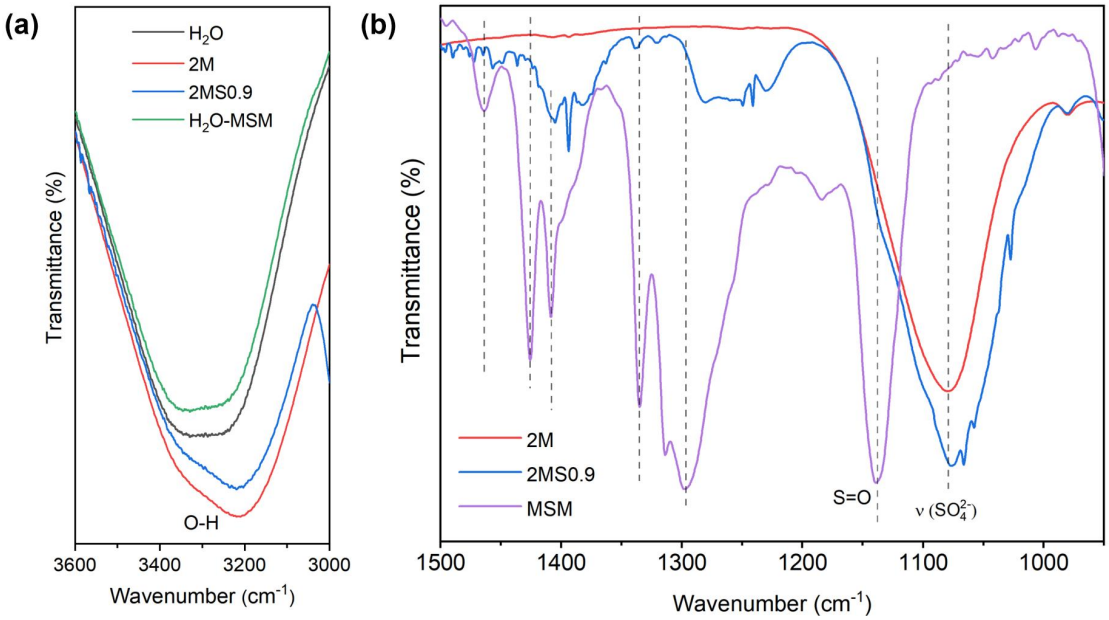

Figure 4.8 FT-IR spectra of 2 M $ZnSO_4$ electrolytes without and with different amount of MSM at ATR mode. (a) OH stretching (3600 - 3000 cm^{-1}) and (b) S=O, ν (SO_4^{2-}) (1500 - 950 cm^{-1})

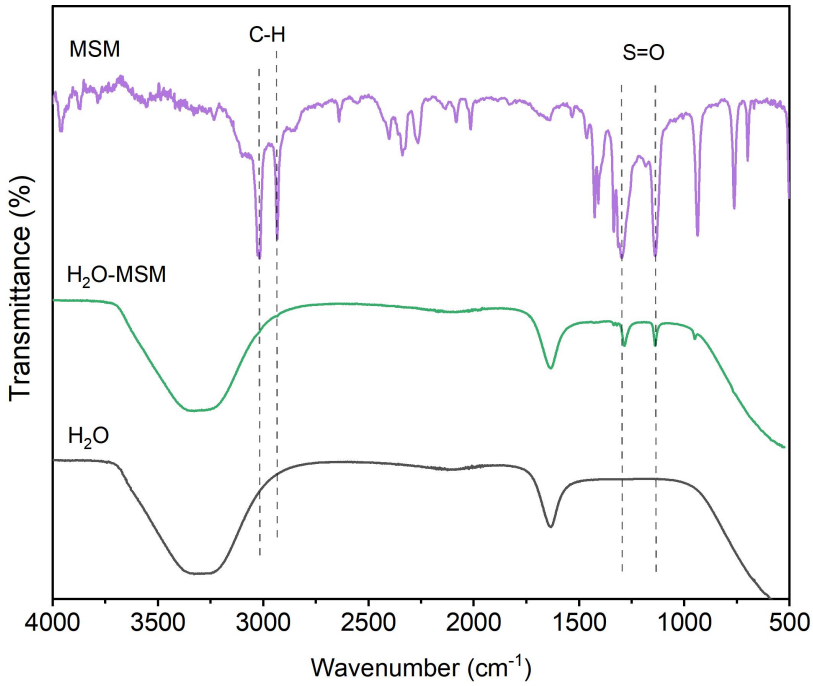

Figure 4.9 FTIR spectroscopy for H_2O, H_2O-MSM and MSM.

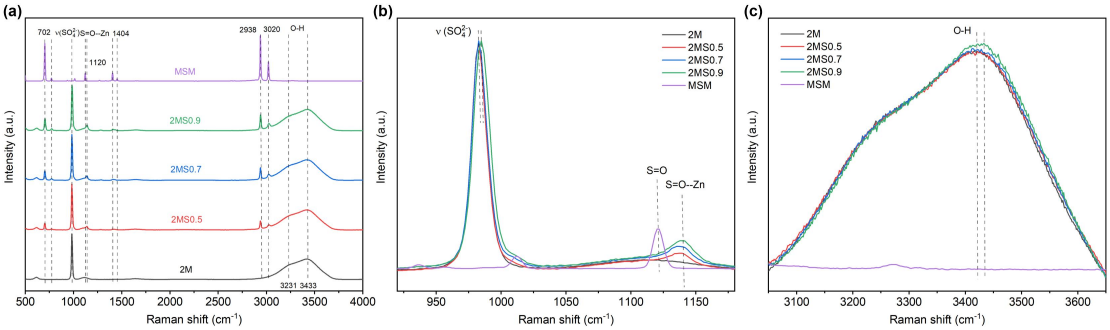

Figure 4.10 Raman spectra of 2 M $ZnSO_4$ electrolytes without and with different amount of MSM. (a) 500-4000 cm^{-1} (b) 920-1180 cm^{-1} and (c) 3050-3650 cm^{-1}.

The strong interaction between MSM and H_2O without interference of Zn^{2+} was evidenced *via* findings from FTIR, Figure 4.7. It can be seen in the figure that compared with $ZnSO_4$ electrolyte, the ν (SO_4^{2-}) vibration is shifted in 2MS0.9, Figure 4.8. This shift vibration is evidenced in the Raman spectra, Figure 4.9, and is attributed to the impaired electrostatic coupling between Zn^{2+} and SO_4^{2-} because of the presence of MSM.

The contact angle of the Zn electrode in $ZnSO_4$-MSM was determined as 69.0°, less than that in $ZnSO_4$ of 75.0°, Figure 4.10. This difference aids practically in a uniform electric distribution and production of homogeneous plating of Zn. The uniform deposition and suppressed corrosion result in high reversibility and stability of Zn chemistry.

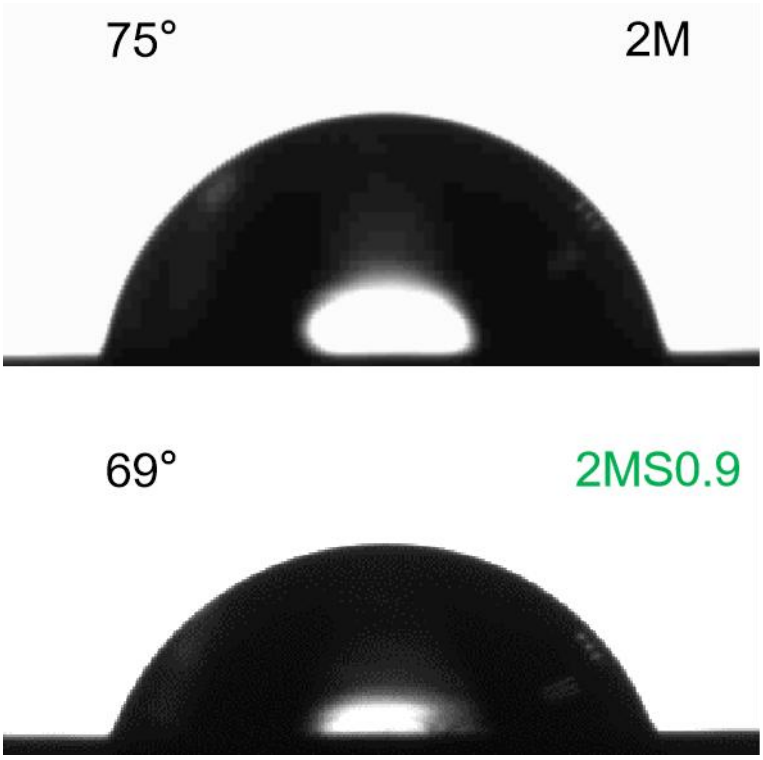

Figure 4.11 Contact angle of 2M and 2MS0.9 electrolytes with Zn foil.

4.2.4 Theoretical Calculation

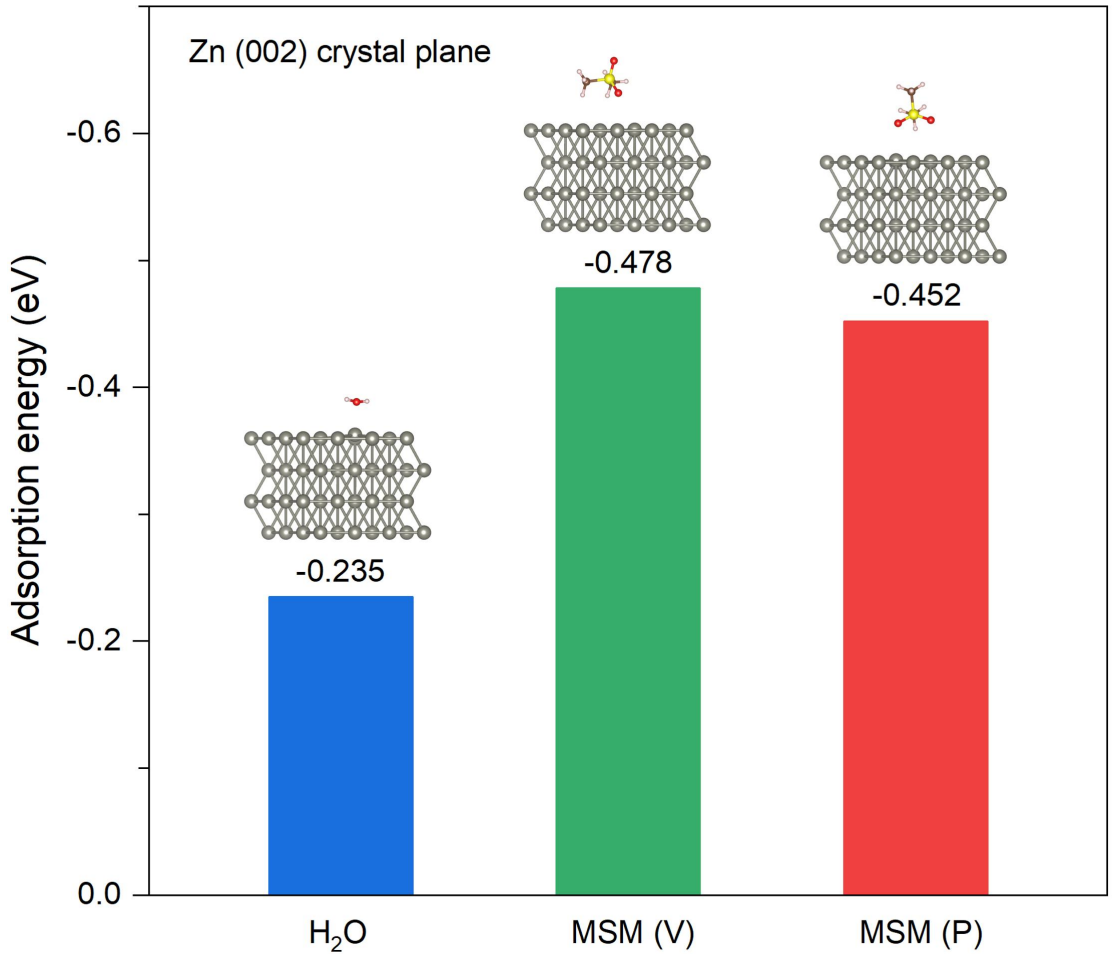

Figure 4.12 Comparison of adsorption energy of H_2O and MSM molecules on Zn (002) crystal plane, vertically and parallelly. Inset shows corresponding absorbed model.

4.2.5 Mechanism Analysis

During Zn deposition, the hydrated $[Zn(H_2O)_n]^{2+}$ in pure $ZnSO_4$ electrolyte brings significant numbers of H_2O molecules that are reduced to release H_2. The increase in local pH because of H_2 evolution promotes formation of Zn^{2+}-insulating hydroxide zinc-salt passivation on the Zn surface and reduces Zn utilization and cycle life, and promotes Zn dendrite growth. In comparison with addition of MSM, the average coordination number of Zn-H_2O in the primary hydration layer is reduced, and the bonding strength between Zn^{2+} ion and solvated H_2O is weakened. This additional interaction amongst MSM, Zn^{2+}, SO_4^{2-} and H_2O rearranges the 'Zn^{2+}–H_2O–SO_4^{2-}–MSM' bonding-network, reduces water activity and generation of by-product

$(Zn(OH)_2)_3(ZnSO_4)(H_2O)_3$. Moreover, MSM molecules absorb on the Zn surface, regulating the homogeneous distribution of Zn^{2+} flux and restricting uncontrolled 2D diffusion that results in uniform and compact Zn deposition. Because of function in both electrolyte structure, and at the electrode-electrolyte interface, the MSM additive boosts reversibility and cycling stability of Zn anodes. Importantly, because $ZnSO_4$-MSM electrolyte is non-flammable (Figure 5.21), it is practically attractive for large-scale applications. Its high boiling and flash point contribute to safety and reduced risk of explosion including, in electrolyte leakage and thermal runaway.

4.3 Conclusion

Relatively low content organic molecules, (MSM) can be used to controllably manipulate typical $ZnSO_4$ electrolyte to give a highly stable and reversible aqueous zinc-ion battery (AZIB). Combined experiment, including FTIR and Raman analyzes reveals that the functional MSM manipulates the electrolyte structure by rearranging the 'Zn^{2+}−H_2O−SO_4^{2-}—MSM' bonding-network and altering Zn anode-electrolyte interface via absorbtion of MSM on the Zn surface. This reduces the water activity, suppresses corrosion and generation of by-product, and gives a uniform compact Zn deposit. The anode ran over 900 cycles (1800 h) with an average CE of 99.9 % under 1 mA cm^{-2} and 1 mA h cm^{-2}, and; exhibited stable and reversible Zn plating/stripping cycling for 460 h under testing conditions of 5 mA cm^{-2} and 5 mA h cm^{-2}. The reversibility and stability of the Zn anode was improved outperformed that using $ZnSO_4$ electrolyte. The Zn-MnO_2 full cells using $ZnSO_4$-MSM electrolyte exhibited a high capacity of 272 mAh g^{-1} at 0.5 A g^{-1} and an improved cycling stability (125 % capacity retention following 700 cycles). These findings offer a quantitative engineering strategy to boost reversibility and stability of Zn anodes in rechargeable AZIBs. Importantly, because the 2 M $ZnSO_4$-MSM electrolyte is nonflammable, it makes AZIBs advantageous for large-scale and low-cost application in electrical-grid storage and clean energy storage.

References

[1] M. Li, J. Lu, Z. Chen, K. Amine, *Adv. Mater.* **2018**, *30*, 1800561.

[2] J. Wu, Y. Cao, H. Zhao, J. Mao, Z. Guo, *Carbon Energy* **2019**, *1*, 57-76.

[3] M. Song, H. Tan, D. Chao, H. J. Fan, *Adv. Funct. Mater.* **2018**, *28*, 1802564.

[4] T. Zhang, Y. Tang, S. Guo, X. Cao, A. Pan, G. Fang, J. Zhou, S. Liang, *Energy Environ. Sci.* **2020**, *13*, 4625-4665.

[5] S. L. Liu, R. Z. Zhang, J. F. Mao, Y. L. Zhao, Q. Cai, Z. P. Guo, *Science Advances*, **2022**, doi: 10.1126/sciadv.eabn5097.

[6] Y. Wang, Z. Wang, F. Yang, S. Liu, S. Zhang, J. Mao, Z. Guo, *Small* **2022**, doi: 10.1002/smll.202107033.

[7] F. Wang, O. Borodin, T. Gao, X. Fan, W. Sun, F. Han, A. Faraone, J. A. Dura, K. Xu, C. Wang, *Nat. Mater.* **2018**, *17*, 543-549.

[8] C. Zhang, J. Holoubek, X. Wu, A. Daniyar, L. Zhu, C. Chen, D. P. Leonard, I. A. Rodríguez-Pérez, J.-X. Jiang, C. Fang, X. Ji, *ChemComm* **2018**, *54*, 14097-14099.

[9] Y. Zhu, J. Yin, X. Zheng, A.-H. Emwas, Y. Lei, O. F. Mohammed, Y. Cui, H. N. Alshareef, *Energy Environ. Sci.* **2021**, *14*, 4463-4473.

[10] J. Zhao, J. Zhang, W. Yang, B. Chen, Z. Zhao, H. Qiu, S. Dong, X. Zhou, G. Cui, L. Chen, *Nano Energy* **2019**, *57*, 625-634.

[11] W. Yang, X. Du, J. Zhao, Z. Chen, J. Li, J. Xie, Y. Zhang, Z. Cui, Q. Kong, Z. Zhao, C. Wang, Q. Zhang, G. Cui, *Joule* **2020**, *4*, 1557-1574.

[12] J. Shi, T. Sun, J. Bao, S. Zheng, H. Du, L. Li, X. Yuan, T. Ma, Z. Tao, *Adv. Funct. Mater.* **2021**, *31*, 2102035.

[13] X. Lin, G. Zhou, M. J. Robson, J. Yu, S. C. T. Kwok, F. Ciucci, *Adv. Funct. Mater.* **2021**, *n/a*, 2109322.

[14] D. Han, C. Cui, K. Zhang, Z. Wang, J. Gao, Y. Guo, Z. Zhang, S. Wu, L. Yin, Z. Weng, F. Kang, Q.-H. Yang, *Nat. Sustain.* **2021**.

[15] S. Liu, J. Mao, W. K. Pang, J. Vongsvivut, X. Zeng, L. Thomsen, Y. Wang, J. Liu, D. Li, Z. Guo, *Adv. Funct. Mater.* **2021**, *31*, 2104281.

[16] J. Hao, L. Yuan, C. Ye, D. Chao, K. Davey, Z. Guo, S.-Z. Qiao, *Angew. Chem. Int. Ed.* **2021**, *60*, 7366-7375.

[17] N. Chang, T. Li, R. Li, S. Wang, Y. Yin, H. Zhang, X. Li, *Energy Environ. Sci.* **2020**, *13*, 3527-3535.

[18] J. Q. Huang, X. Y. Guo, X. Y. Lin, Y. Zhu, B. Zhang, *Research* **2019**, *2019*, 10.

[19] D. Wang, Q. Li, Y. Zhao, H. Hong, H. Li, Z. Huang, G. Liang, Q. Yang, C. Zhi, *Adv. Energy Mater.* **2022**, *n/a*, 2102707.

[20] H. Lu, X. Zhang, M. Luo, K. Cao, Y. Lu, B. B. Xu, H. Pan, K. Tao, Y. Jiang, *Adv. Funct. Mater.* **2021**, *31*, 2103514.

[21] J. Cui, X. Liu, Y. Xie, K. Wu, Y. Wang, Y. Liu, J. Zhang, J. Yi, Y. Xia, *Mater. Today Energy* **2020**, *18*, 100563.

[22] L. Cao, D. Li, E. Hu, J. Xu, T. Deng, L. Ma, Y. Wang, X.-Q. Yang, C. Wang, *J. Am. Chem. Soc.* **2020**, *142*, 21404-21409.

[23] P. Sun, L. Ma, W. Zhou, M. Qiu, Z. Wang, D. Chao, W. Mai, *Angew. Chem. Int. Ed.* **2021**, *60*, 18247-18255.

[24] L. Cao, D. Li, T. Pollard, T. Deng, B. Zhang, C. Yang, L. Chen, J. Vatamanu, E. Hu, M. J. Hourwitz, L. Ma, M. Ding, Q. Li, S. Hou, K. Gaskell, J. T. Fourkas, X.-Q. Yang, K. Xu, O. Borodin, C. Wang, *Nat. Nanotechnol.* **2021**, *16*, 902-910.

[25] L. Ma, T. P. Pollard, Y. Zhang, M. A. Schroeder, M. S. Ding, A. V. Cresce, R. Sun, D. R. Baker, B. A. Helms, E. J. Maginn, C. Wang, O. Borodin, K. Xu, *Angew. Chem. Int. Ed.* **2021**, *60*, 12438-12445.

[26] Q. Zhang, J. Luan, L. Fu, S. Wu, Y. Tang, X. Ji, H. Wang, *Angew. Chem. Int. Ed.* **2019**, *58*, 15841-15847.

[27] C. Huang, X. Zhao, S. Liu, Y. Hao, Q. Tang, A. Hu, Z. Liu, X. Chen, *Adv. Mater.* **2021**, *33*, 2100445.

[28] M. D. Yan, N. Dong, X. S. Zhao, Y. Sun, H. L. Pan, *ACS Energy Lett.* **2021**, *6*, 3236-3243.

[29] X. Zeng, K. Xie, S. Liu, S. Zhang, J. Hao, J. Liu, W. K. Pang, J. Liu, P. Rao, Q. Wang, J. Mao, Z. Guo, *Energy Environ. Sci.* **2021**, *14*, 5947-5957.

[30] M. Han, J. Huang, X. Xie, T. Li, J. Huang, S. Liang, J. Zhou, and H. Fan, *Adv. Funct. Mater.* **2022**, 2110957.

[31] P. Jiang, L. Chen, H. Shao, S. Huang, Q. Wang, Y. Su, X. Yan, X. Liang, J. Zhang, J. Feng, and Z. Liu, *ACS Energy Lett.* **2019**, 4, 1419-1426.

Table 4.1 Boiling point, flash point and solubility (25 ℃) of selected rganic additives in electrolyte of AZIBs.

Organic additive	**Boiling point (℃)**	**Flash point (℃)**	**Solubility in water (25 ℃)**	**Viscosity (mPa·s)**
AM (acrylamide)	231.7	79.0 ± 19.8	Soluble	
Amino acid Arg	367.6 ± 52	176.1 ± 30.7	Soluble	
AN (acetonitrile)	63.5	5.6	Soluble	0.325-0.375
DME (1,2-dimethoxyethane)	84.5	0.0	Soluble	1.1
DMSO (dimethyl sulfoxide)	189.0 ± 9.0	85.0	Miscible	1.1
Et (erythritol)	330.0	208.7 ± 21.1	Soluble	
EC (ethyl carbonate)	126.8	31.1	Insoluble	0.748-0.868
EMC (ethyl methyl carbonate)	107.5	26.7 ± 7.8	Immiscible	0.65
EG (ethylene glycol)	197.5	108.2 ± 13.0	Miscible	10.38-86.9
Glucose	527.1 ± 50.0	286.7± 26.6	Freely soluble	
Glycerol	290.0	160.0	Soluble	18-243

Maltose	667.9 ± 55.0	357.8 ± 31.5	Very soluble	
Methanol	48.1 ± 3.0	11.1	Miscible	0.5142-0.6405
Na_2EDTA	> 100	325.2	Miscible	
PAM (polyacrylamide)	231.7	79.0 ± 19.8	Soluble	
Sac (saccharin)	438.9 ± 28.0	219.3 ± 24.0	Slightly soluble	
SL (sulfolane)	285.6 ± 8.0	165.6	Soluble	10.286
SN (succinonitrile)	268.5 ± 13.0	141.1 ± 13.7	Slightly soluble	2.591
TEP (triethyl phosphate)	219.3 ± 8.0	115.6	Soluble	N/A
TFEP (tris(2,2,2-trifluoroethyl) phosphate)	176.2 ± 40.0	60.4 ± 27.3	N/A	N/A
TMP (trimethyl phosphate)	197.2	83.7 ± 38.8	Soluble	N/A
Urea	165.1 ± 23.0	53.7 ± 22.6	Soluble	
MSM (This work)	240.9 ± 8.0	143	Slightly soluble	N/A

Table 4.2 Comparison of accumulative plated capacity with current density of selected organic additives in electrolyte of AZIBs.

Organic additive	**Current density ($mA\ cm^{-2}$)**	**Accumulative plated capacity ($mAh\ cm^{-2}$)**	**Reference**
AM	10	900	7
	2	380	
	1	340	
Amino acid Arg	5	5500	8

	10	4500	
	1	1475	
AN	1	650	9
	2	600	
	0.5	250	
BIS-TRIS	5	1500	10
	1	625	
CT3G30	2	800	11
DME	2	375	12
DMSO	0.5	250	13
Et_2O	0.2	25	15
EG	2	135	16
Glucose	1	1000	17
	5	687.5	
Glycerol	2	900	18
	1	750	
ILZE	2	1500	19
Maltose	1	600	20
Methanol	1	450	21
$Me_3EtNOTF$	0.5	1500	1
Na_2EDTA	5	5000	22
	2	450	
P_{4441}-TFSI	0.5	1600	23
	1	400	
	2.5	350	
PAM	20	1100	24

	2	170	
	1	90	
PEG-400	2	8000	25
	1	4500	
	0.5	2000	
PEO-4000	1	600	26
PEO-100000	1	1500	27
Saccharin	10	2750	28
	40	1100	
SDBS	0.5	375	29
SL	0.5	200	30
SN	0.2	40	31
	0.05	20	
TBA_2SO_4	10	2000	32
	5	1125	
	2	300	
TC	5	1250	33
	1	1072.5	
	10	850	
TEP	1	750	34
TEP-PC	0.5	650	35
TFEP	0.5	175	36
TMP-DMC/DMF	1	2500	37
Trisodium citrate	5	100	38
Urea	0.1	120	39a
	1	350	39b

MSM	**5**	**1350**	**This work**
	1	**600**	

Table 4.3 Comparison of Coulombic efficiency (CE) and cumulaltive plated capacity for Zn half cells with selected organic additives in electrolyte of AZIBs.

Organic additive	**Cumulative plated capacity ($Ah\ cm^{-2}$)**	**CE (%)**	**Reference**
AM	0.04	N/A	7
Amino acid Arg	0.325	98.3[a]	8
AN	0.3	99.3[a]	9
BIS-TRIS	0.4	98.5[a]	10
DME	0.156	N/A	12
DMSO	0.2	99.5[a]	13
EG	0.12	98[a]	16
Glucose	0.1	97.3[a]	17
Glycerol	0.5	98.3[a]	18
ILZE	0.3	99.36[b]	19
Maltose	0.032	99.7[a]	20
Methanol	0.45	99.7[a]	21
$Me_3EtNOTF$	0.5	99.8[a]	1
Na_2EDTA	0.7	99.5[a]	22
P_{4441}-TFSI	N/A	98.1[a]	23
PEO-4000	0.35	98.7[b]	26
PEO-100000	1.5	99.5[b]	27
Saccharin	0.5	99.6[a]	28
SL	0.05	98[b]	30

SN	0.025	98.4[a]	31
TBA_2SO_4	N/A	98[b]	32
TC	750 cycles at 1 mA cm^{-2}	97.7[b]	33
TEP	0.126	99.5[a]	34
TEP-PC	N/A	97.7[b]	35
TFEP	0.175	99.1[a]	36
TMP	5	99.57[a]	37
Urea	N/A	96.2[b]	39a
MSM	**0.85**	**99.9[a]**	**This work**

[a] average CE, [b] reaches until stable CE, N/A: not available.[2]

References

[1] L. Cao, D. Li, T. Pollard, T. Deng, B. Zhang, C. Yang, L. Chen, J. Vatamanu, E. Hu, M. J. Hourwitz, L. Ma, M. Ding, Q. Li, S. Hou, K. Gaskell, J. T. Fourkas, X.-Q. Yang, K. Xu, O. Borodin, C. Wang, *Nat. Nanotechnol.* **2021**, *16*, 902-910.

[2] A. Bernardi, R. Faller, D. Reith, K. N. Kirschner, *Softwarex* **2019**, *10*, 100241.

[3] a) W. L. Jorgensen, J. Tirado-Rives, *Proc. Natl. Acad. Sci. U.S.A.* **2005**, *102*, 6665; b) L. S. Dodda, J. Z. Vilseck, J. Tirado-Rives, W. L. Jorgensen, *J. Phys. Chem. B* **2017**, *121*, 3864-3870.

[4] G. Bussi, D. Donadio, M. Parrinello, *J. Chem. Phys.* **2007**, *126*, 014101.

[5] H. J. C. Berendsen, J. P. M. Postma, W. F. van Gunsteren, A. DiNola, J. R. Haak, *J. Chem. Phys.* **1984**, *81*, 3684-3690.

[6] a) P. E. Blöchl, *Phys. Rev. B* **1994**, *50*, 17953-17979; b) B. Hammer, L. B. Hansen, J. K. Nørskov, *Phys. Rev. B* **1999**, *59*, 7413-7421; c) G. Kresse, D. Joubert, *Phys. Rev. B* **1999**, *59*, 1758-1775; d) J. Tao, J. P. Perdew, V. N. Staroverov, G. E. Scuseria, Phys. Rev. Lett. **2003**, *91*, 146401; e) S. Lebègue, O. Eriksson, *Phys. Rev. B* **2009**, *79*, 115409.

[7] X. Zeng, X. Meng, W. Jiang, M. Ling, L. Yan, C. Liang, *Electrochim. Acta* **2021**, *378*, 138106.

[8] H. Lu, X. Zhang, M. Luo, K. Cao, Y. Lu, B. B. Xu, H. Pan, K. Tao, Y. Jiang, *Adv. Funct. Mater.* **2021**, *31*, 2103514.

[9] J. Shi, K. Xia, L. Liu, C. Liu, Q. Zhang, L. Li, X. Zhou, J. Liang, Z. Tao, *Electrochim. Acta* **2020**, *358*, 136937.

[10] M. Luo, C. Wang, H. Lu, Y. Lu, B. B. Xu, W. Sun, H. Pan, M. Yan, Y. Jiang, *Energy Stor. Mater.* **2021**, *41*, 515-521.

[11] M. Chen, J. Chen, W. Zhou, X. Han, Y. Yao, C.-P. Wong, *Adv. Mater.* **2021**, *33*, 2007559.

[12] J. Cui, X. Liu, Y. Xie, K. Wu, Y. Wang, Y. Liu, J. Zhang, J. Yi, Y. Xia, *Mater. Today Energy* **2020**, *18*, 100563.

[13] L. Cao, D. Li, E. Hu, J. Xu, T. Deng, L. Ma, Y. Wang, X.-Q. Yang, C. Wang, *J. Am. Chem. Soc.* **2020**, *142*, 21404-21409.

[14] Z. Huang, T. Wang, X. Li, H. Cui, G. Liang, Q. Yang, Z. Chen, A. Chen, Y. Guo, J. Fan, C. Zhi, *Adv. Mater.* **2021**, *n/a*, 2106180.

[15] W. Xu, K. Zhao, W. Huo, Y. Wang, G. Yao, X. Gu, H. Cheng, L. Mai, C. Hu, X. Wang, *Nano Energy* **2019**, *62*, 275-281.

[16] N. Chang, T. Li, R. Li, S. Wang, Y. Yin, H. Zhang, X. Li, *Energy Environ. Sci.* **2020**, *13*, 3527-3535.

[17] P. Sun, L. Ma, W. Zhou, M. Qiu, Z. Wang, D. Chao, W. Mai, *Angew. Chem. Int. Ed.* **2021**, *60*, 18247-18255.

[18] Y. Zhang, M. Zhu, K. Wu, F. Yu, G. Wang, G. Xu, M. Wu, H.-K. Liu, S.-X. Dou, C. Wu, Journal of Materials Chemistry A **2021**, *9*, 4253-4261.

[19] L. Ma, S. Chen, N. Li, Z. Liu, Z. Tang, J. A. Zapien, S. Chen, J. Fan, C. Zhi, *Adv. Mater.* **2020**, *32*, 1908121.

[20] W. Chen, S. Guo, L. Qin, L. Li, X. Cao, J. Zhou, Z. Luo, G. Fang, S. Liang, *Adv. Funct. Mater.* **2022**, *n/a*, 2112609.

[21] J. Hao, L. Yuan, C. Ye, D. Chao, K. Davey, Z. Guo, S.-Z. Qiao, *Angew. Chem. Int. Ed.* **2021**, *60*, 7366-7375.

[22] S.-J. Zhang, J. Hao, D. Luo, P.-F. Zhang, B. Zhang, K. Davey, Z. Lin, S.-Z. Qiao, *Adv. Energy Mater.* **2021**, *11*, 2102010.

[23] L. Ma, T. P. Pollard, Y. Zhang, M. A. Schroeder, M. S. Ding, A. V. Cresce, R. Sun, D. R. Baker, B. A. Helms, E. J. Maginn, C. Wang, O. Borodin, K. Xu, *Angew. Chem. Int. Ed.* **2021**, *60*, 12438-12445.

[24] Q. Zhang, J. Luan, L. Fu, S. Wu, Y. Tang, X. Ji, H. Wang, *Angew. Chem. Int. Ed.* **2019**, *58*, 15841-15847.

[25] Y. Wu, Z. Zhu, D. Shen, L. Chen, T. Song, T. Kang, Z. Tong, Y. Tang, H. Wang, C. S. Lee, *Energy Stor. Mater.* **2022**, *45*, 1084-1091.

[26] M. Yan, C. Xu, Y. Sun, H. Pan, H. Li, *Nano Energy* **2021**, *82*, 105739.

[27] Y. Jin, K. S. Han, Y. Shao, M. L. Sushko, J. Xiao, H. Pan, J. Liu, *Adv. Funct. Mater.* **2020**, *30*, 2003932.

[28] C. Huang, X. Zhao, S. Liu, Y. Hao, Q. Tang, A. Hu, Z. Liu, X. Chen, *Adv. Mater.* **2021**, *33*, 2100445.

[29] J. Hao, J. Long, B. Li, X. Li, S. Zhang, F. Yang, X. Zeng, Z. Yang, W. K. Pang, Z. Guo, *Adv. Funct. Mater.* **2019**, *29*, 1903605.

[30] X. Lin, G. Zhou, M. J. Robson, J. Yu, S. C. T. Kwok, F. Ciucci, *Adv. Funct. Mater.* **2021**, *n/a*, 2109322.

[31] W. Yang, X. Du, J. Zhao, Z. Chen, J. Li, J. Xie, Y. Zhang, Z. Cui, Q. Kong, Z. Zhao, C. Wang, Q. Zhang, G. Cui, *Joule* **2020**, *4*, 1557-1574.

[32] A. Bayaguud, X. Luo, Y. Fu, C. Zhu, *ACS Energy Lett.* **2020**, *5*, 3012-3020.

[33] R. Yao, L. Qian, Y. Sui, G. Zhao, R. Guo, S. Hu, P. Liu, H. Zhu, F. Wang, C. Zhi, C. Yang, *Adv. Energy Mater.* **2022**, *12*, 2102780.

[34] S. Liu, J. Mao, W. K. Pang, J. Vongsvivut, X. Zeng, L. Thomsen, Y. Wang, J. Liu, D. Li, Z. Guo, *Adv. Funct. Mater.* **2021**, *31*, 2104281.

[35] X. Qiu, N. Wang, X. Dong, J. Xu, K. Zhou, W. Li, Y. Wang, *Angew. Chem. Int. Ed.* **2021**, *60*, 21025-21032.

[36] L. Cao, D. Li, E. Hu, J. Xu, T. Deng, L. Ma, Y. Wang, X.-Q. Yang, C. Wang, *J. Am. Chem. Soc.* **2020**, *142*, 21404-21409.

[37] A. Naveed, H. Yang, Y. Shao, J. Yang, N. Yanna, J. Liu, S. Shi, L. Zhang, A. Ye, B. He, J. Wang, *Adv. Mater.* **2019**, *31*, 1900668.

[38] N. Wang, S. Zhai, Y. Ma, X. Tan, K. Jiang, W. Zhong, W. Zhang, N. Chen, W. Chen, S. Li, G. Han, Z. Li, *Energy Stor. Mater.* **2021**, *43*, 585-594.

[39] a) J. Zhao, J. Zhang, W. Yang, B. Chen, Z. Zhao, H. Qiu, S. Dong, X. Zhou, G. Cui, L. Chen, *Nano Energy* **2019**, *57*, 625-634; b) Z. Hou, M. Dong, Y. Xiong, X. Zhang, H. Ao, M. Liu, Y. Zhu, Y. Qian, *Small* **2020**, *16*, 2001228.

CHAPTER 5 GBL as Electrolyte additives for aqueous Zn-ion batteries

5.1 Introduction

To achieve carbon neutrality by 2050, a significantly increased use of clean energy technologies including, electric vehicles (EVs) and energy efficient building retrofits, will be needed. Storage of energy is critical to underpinning sustainable consumer electronics, transport and industry smart-grids. Li-ion batteries have been dominant. However, significant drawbacks include relative high cost and low safety.[1,2] Aqueous rechargeable zinc-ion batteries (AZIBs) have attracted research attention for large-scale energy storage because of advantageous, high safety, low toxicity, abundance of materials and unique properties of zinc including, low redox potential (- 0.7626 V *vs*. standard hydrogen electrode), high gravimetric capacity (820 mA h g^{-1}), and high volumetric capacity (5585 mAh cm^{-3}).[3-6] Drawbacks however include, Zn dendrite formation, corrosion and by-product and H_2 evolution that mitigate against sufficiently high reversibility and stability.

Electrochemical behavior of Zn metal is determined principally by the properties of the aqueous electrolyte and electrode-electrolyte interface. These are closely related to the solvation structures of hydrated Zn^{2+} ions, anions, and hydrogen bonding-network. Therefore, a reconstruction of the chemical bonding-network and solvation structure of cations and anions in aqueous electrolyte, and optimization of the electrode-electrolyte interface can be used to practically regulate the performance of Zn anodes. Proposals to tune the solvation structure of electrolyte and boost reversibility of Zn anodes included, high concentration,[7-9] water-in-eutectic,[10-14] and aqueous/organic hybrid electrolytes[15-18]. Drawbacks from these electrolytes have included however, high cost, unwanted low ionic conductivity and high viscosity. The addition of organics has been reported because these species, as liquids or solids can interact with Zn^{2+} and H_2O molecules to change the solvated structure of Zn hydration and the hydrogen bonding-network without high concentration of slats or

solvents.[19-29] However, the electrochemical performance of these Zn anodes remains poor, especially under harsh condition of high current density/capacity of up to 10 mA cm^{-2} and 10 mAh cm^{-2}. Additionally, particular organic molecules are highly flammable. Although the nonflammable nature of water assures safety of AZIBs, the hydrogen evolution reaction (HER) and/or oxygen evolution reaction (OER) during battery cycling and/or idling, lowers the Coulombic efficiency (CE) and cycle life and may cause explosions. Any application to AZIBs must therefore suppress these reactions without reducing practical safety. A nonflammable and/or low vapor pressure solvent is necessarily required therefore to regulate solvation structure and interface so as to boost reversibility and stability of Zn anodes under harsh conditions.

Because gamma-butyrolactone (GBL) has a high boiling and flash temperature, respectively, T_b = 204 °C and T_f = 97 °C, relatively low viscosity = 1.73 cP at 25 °C, good ionic conductivity, and a high dielectric constant e = 39, it is practically attractive as a solvent/additive for rechargeable batteries. GBL-based electrolytes have in fact been used in Li-ion batteries over a range of temperature. [30,31]

Here GBL was adopted as a new electrolyte additive to $ZnSO_4$ electrolyte. It was postulated that through adjusting volume percent of GBL in GBL-based electrolytes a small volume, ~ 1% solvent, in 2 M $ZnSO_4$ would significantly boost Zn plating/stripping performance under different current density. Experiment and theoretical computation confirmed that the functional GBL additive weakens the bonding strength between Zn^{2+} ion and solvated H_2O and rearranges the 'Zn^{2+}–H_2O–SO_4^{2-}–GBL' bonding-network to reduce water activity and suppress corrosion and generation of by-product. The Zn metal surface absorbs GBL rather than H_2O which restricts uncontrollable 2D diffusion and gives rise to uniform deposition. Thus, the Zn-MnO_2 full cells using $ZnSO_4$-GBL electrolyte exhibited superior performance to that using GBL-free electrolyte. Importantly, because 2 M $ZnSO_4$-GBL electrolyte is nonflammable it makes AZIBs practically promising for large-scale application.

5.2 Results and Discussion

5.2.1 Stability of the Zn Electrode

The stability of the Zn electrode in aqueous electrolyte with and without GBL was compared in Zn||Zn symmetric cells, Figure 5.1a-c (Figure 5.2). GBL addition resulted in excellent stability of Zn in Zn||Zn in normal to harsh condition. With an optimized electrolyte of 2 M $Zn(SO_4)_2$ with 1% GBL in volume (2MG1), the Zn symmetrical cell exhibited highly stable cycling performance for over 4200 h at a current density of 1 mA cm^{-2} and an areal capacity of 1 mA h cm^{-2}, significantly however, the 2M $ZnSO_4$ electrolyte failed following 700 h, Figure 1a. Under harsh conditions of 10 mA cm^{-2} and 10 mA h cm^{-2}, the Zn electrode with 2MG1 electrolyte remained stable and exhibited reversible Zn plating/stripping for 1170 h. Importantly, this is significantly longer than that in the blank electrolyte of 70 h, Figure 1b. At a high 20 mA cm^{-2} and 20 mA h cm^{-2}, Figure 5.1c, the Zn electrode in the symmetrical cell with optimized electrolyte exhibited stable cycling for > 140 h, whilst the Zn electrode in the blank electrolyte exhibited a short-circuit in < 25 h. These findings strongly evidence the significant boost in reversibility and stability of the Zn anodes resulting from GBL addition. To confirm the highly significant impact of GBL addition, the cumulative plated capacity (CPC) was compared directly with selected, representative published data, Figure 5.1d (Table 5.1). Significantly, it is seen in the figure (and table) that the ultra-high CPC of 5.85 Ah cm^{-2} exhibited at current density 10 mA cm^{-2} for the $ZnSO_4$-GBL electrolyte exceeds that for many published electrolyte additives.

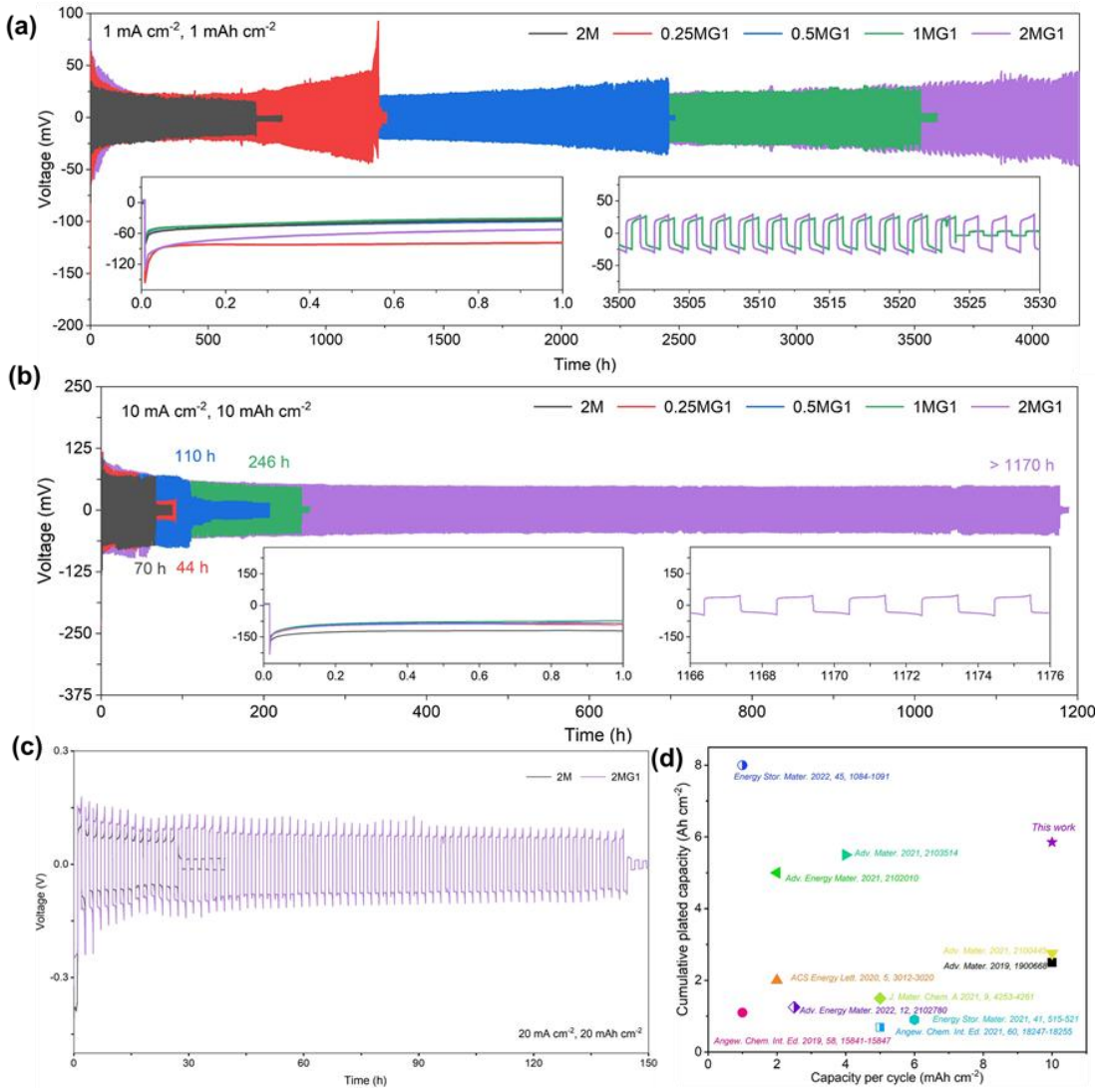

Figure 5.1 Zn||Zn plating/stripping and stability. Zn||Zn symmetric cells containing differing concentration of $ZnSO_4$ with same volume percent of additive at current density and areal capacity of a) 1 mA cm^{-2} at 1 mAh cm^{-2}, b) 10 mA cm^{-2} at 10 mAh cm^{-2} and c) 20 mA cm^{-2} at 20 mAh cm^{-2}. d) Cumulative plated capacity *vs.* capacity per cycle of 2MG1 electrolyte compared with selected others.

5.2.2 Reversibility of the Zn Electrode

Reversibility of the Zn electrode in aqueous electrolyte with and without GBL was compared in Zn||Cu asymmetric cells, Figure 5.3a-d (Figure 5.3 and 5.4). It was found that there are marginal differences in the initial Coulombic efficiency, that increases with increasing $ZnSO_4$ concentration i.e. 2MG1 > 2M > 1MG1 > 0.5MG1 > 0.25MG1 (Figure 5.3). The addition of less or more GBL, reduced the initial Coulombic efficiency (Figure 5.4). The presence of 1% GBL boosted the initial Coulombic efficiency to 92.1 % at 1 mA cm^{-2} and 1 mA h cm^{-2}, and the average CE increased to 99.9 % for over 2720 cycles (5440 h), Figure 5.3a. In comparison, the 2 M $ZnSO_4$ electrolyte exhibited a low initial Coulombic efficiency of 91.1 % and an average CE of 99.6 %, noticeably failing at the 222th cycle, Figures 5.5a, 5.5b. As is shown in Figure 5.5c and 5.5d, the addition of GBL increased the overpotential for Zn plating/stripping on the Cu surface at the first cycle, but reduced it following cycling; a finding due to increased, or reduced interphasic resistance as compared with blank electrolyte (Figure 5.5).

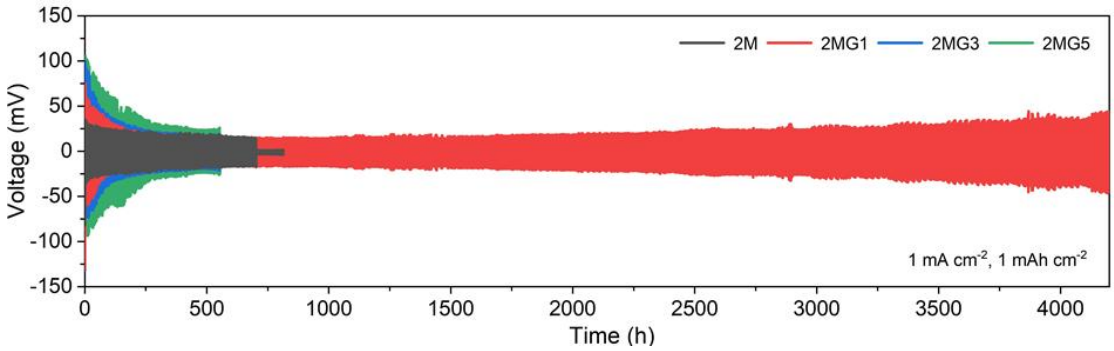

Figure 5.2 Additive effect: Cycle performance for Zn||Zn symmetric cells using 2M $ZnSO_4$ electrolyte with differing volume percent of GBL at 1 mA cm^{-2} and 1 mAh cm^{-2}.

5.2.3 Scanning Electron Microscope

Addition of GBL concomitantly tuned Zn deposition morphology and suppressed corrosion. The **scanning electron microscopy (SEM)** images confirmed that following 50 cycles with

Zn||Cu cells, the Zn surface in the $ZnSO_4$ electrolyte become an apparent scattered microporous structure, Figure 5.3e, whilst there remained a large-area connected vertical-arrangement of sheet structure on the Zn surface in the $ZnSO_4$-GBL electrolyte; this formed a densely integrated binding network, Figure 5.3f. XRD findings for the Zn electrode following cycling showed $Zn_4SO_4(OH)_6 \cdot 5H_2O$ by-product in the $ZnSO_4$ electrolyte. The peaks however for $Zn_4SO_4(OH)_6 \cdot 5H_2O$ were significantly reduced in $ZnSO_4$-GBL electrolyte, confirming that Zn electrode corrosion was significantly suppressed, Figure 5.3g. These findings were confirmed *via* a linear polarization test. As is seen in Figure 5.6a, the Zn electrode in $ZnSO_4$-GBL electrolyte exhibited a greater corrosion voltage of -0.933 V compared with that for pure $ZnSO_4$ electrolyte of -0.922 V. This finding evidences a lowered tendency for corrosion side reactions in $ZnSO_4$-GBL electrolyte. A reduced hydrogen and oxygen evolution current obtained from linear sweep voltammetry (LSV) curves confirm the impact on boosting reversibility and stability *via* controlled manipulation with GBL additive (Figure 5.7). The contact angle of the Zn electrode in $ZnSO_4$-GBL was determined as 64.0°, less than that in $ZnSO_4$ of 75.0°, Figure 5.6b. This difference aids practically in a uniform electric distribution and production of homogeneous plating of Zn. The uniform deposition and suppressed corrosion result in high reversibility and stability of Zn chemistry.

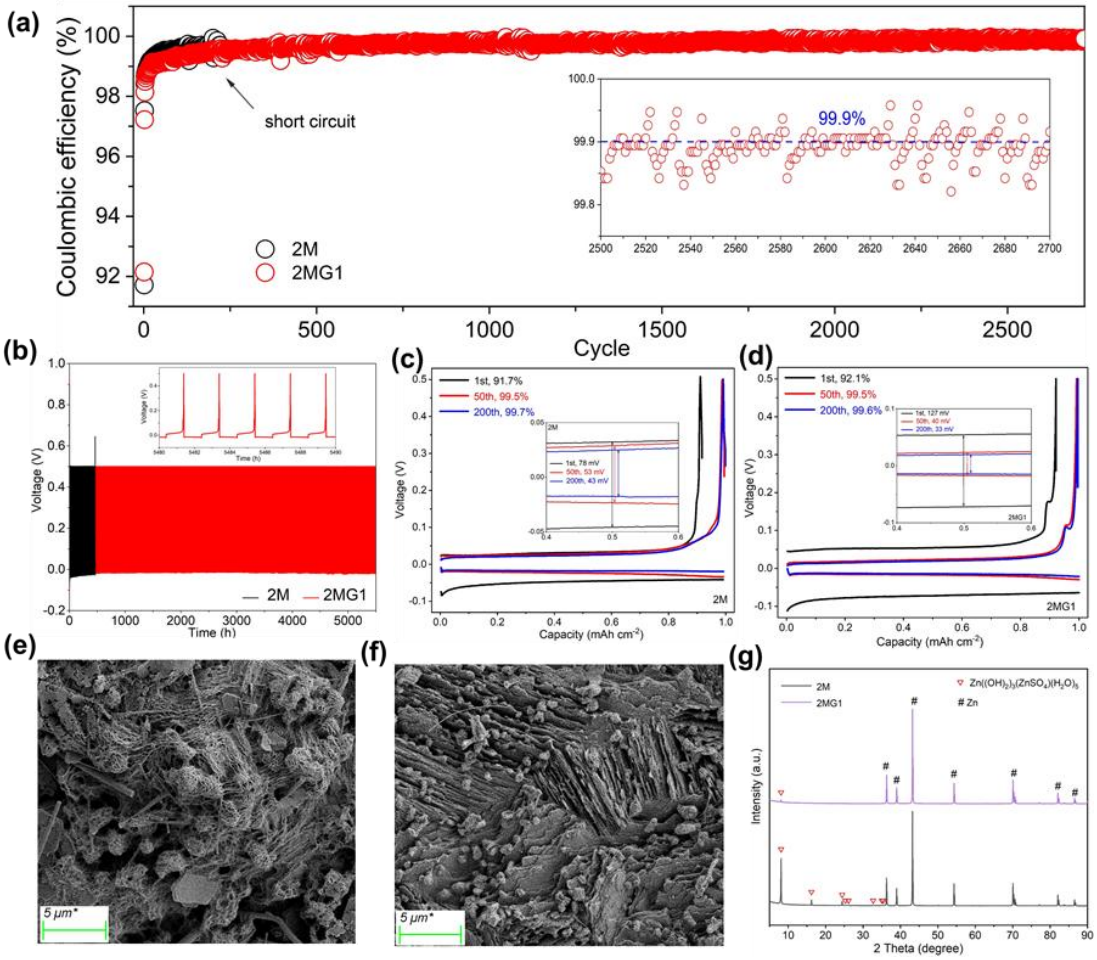

Figure 5.3 Zn||Cu half-cell performance and properties. a) Coulombic efficiency (CE) for cells in 2M $ZnSO_4$ electrolyte with (2MG1) and without (2M) 1% GBL. b) Time-voltage curves. Charge/discharge voltage profiles of half cell with c) 2M and d) 2MG1 electrolyte at 1st, 50th and 200th cycle with magnified view of corresponding cycles in potential range between 0.4 and 0.6 V at current density 1 mA cm^{-2}. SEM images of Zn-foil in e) 2M and f) 2MG1 electrolyte for half cells following 50 cycles. g) XRD spectra for Zn-foil in 2M and 2MG1 electrolyte for half cells following 50 cycles.

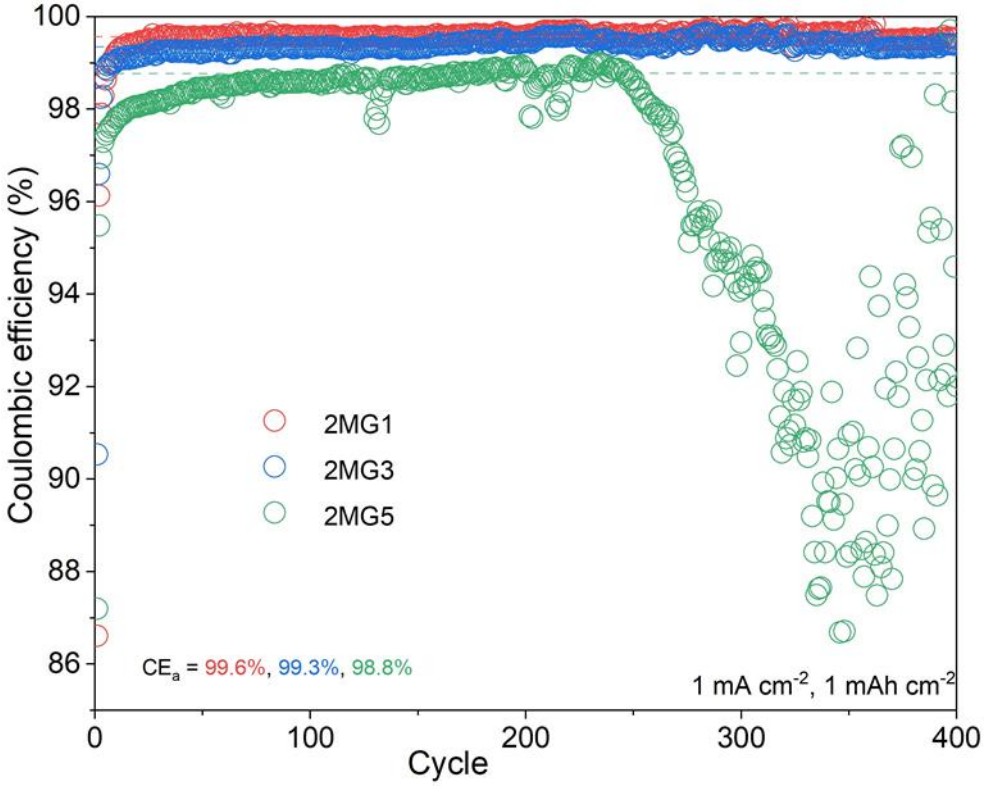

Figure 5.4 Coulombic efficiency for Zn||Cu half cells using 2M $ZnSO_4$ electrolyte with differing volume percent of GBL at 1 mA cm^{-2} and 1 mAh cm^{-2}.

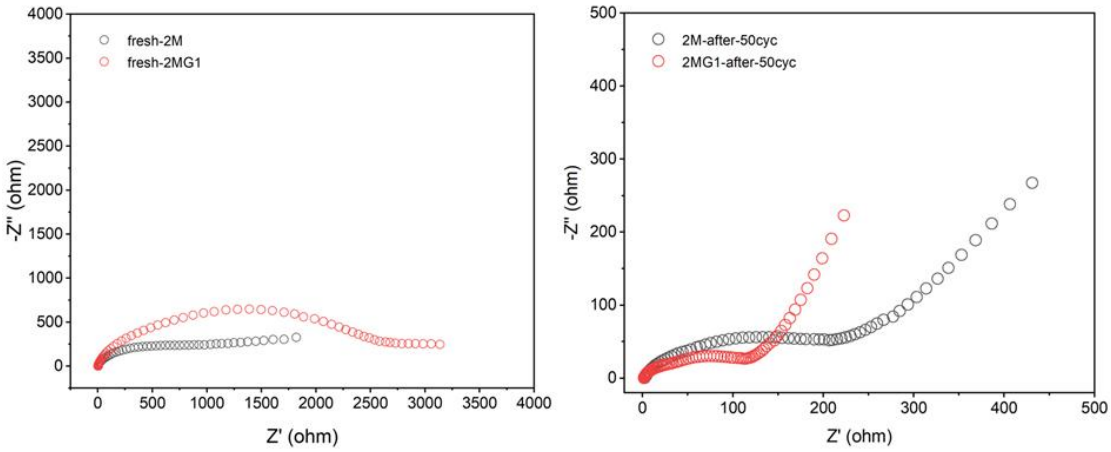

Figure 5.5 Nyquist plots between 2M and 2MG1 electrolytes of the cells before and following 50 cycles.

5.2.4 Chemical and physical properties of electrolytes

Judiciously combined experimental characterizations including, nuclear magnetic resonance (NMR), Fourier transform infrared spectroscopy (FTIR) and Raman spectroscopy, together with theoretical computations were used to determine the underlying mechanism for Zn metal in $ZnSO_4$-GBL. ^2H NMR spectra showed that the ^2H peak in the electrolyte shifted from 4.683 to 4.697 ppm following addition of GBL, Figure 5.6c, evidencing a decreased surrounding electronic density and a weakened shielding of protons in water because of interaction between GBL and D_2O. The addition of GBL weakens the solvation coordination between Zn^{2+} and water. This finding was confirmed *via* FTIR and Raman results. Compared with pure GBL, the C-H stretching moves to lower wave number in $ZnSO_4$-GBL caused by interaction between GBL and water, Figure 5.6d. The strong interaction between GBL and H_2O without interference of Zn^{2+} was evidenced *via* findings from FTIR, Figure 5.6d (Figure 5.8). It can be seen in the figure that compared with $ZnSO_4$ electrolyte, the ν (SO_4^{2-}) vibration is shifted in $ZnSO_4$-GBL, Figure 5.6e. This shift vibration is evidenced in the Raman spectra, Figure 5.8f, and is attributed to the impaired electrostatic coupling between Zn^{2+} and SO_4^{2-} because of the presence of GBL.

5.2.5 Molecular Dynamics (MD) Simulation

Molecular dynamics (MD) simulation was used to analyze the electrolyte structure of pure $ZnSO_4$ and $ZnSO_4$-GBL. In Zn aqueous electrolyte, Zn^{2+} is typically coordinated by 4-6 H_2O molecules, whereas SO_4^{2-} anions mainly coordinate with hydrated Zn^{2+} through the hydrogen bonding-network formed by H_2O molecules (Figure 5.9). There are additional interactions amongst GBL, Zn^{2+}, SO_4^2 and H_2O that are present in the $ZnSO_4$-GBL electrolyte, Figure 5.8g. Corresponding radial distribution functions (RDFs) and average coordination number (ACN) were obtained, Figure 5.6h (Figure 5.10). With addition of GBL, the peak for Zn-O pair in the RDF curve shifted from 1.95 to 1.85 Å, evidencing that GBL has a significant impact on constraining water. The average coordination number for Zn-H_2O in the first hydration layer was reduced from 5.2 in $ZnSO_4$ to 3.9 for $ZnSO_4$-GBL as shown by short dashed-line in Figure 5.8h, confirming that

the interaction of GBL and H_2O weakened the preferred coordination between Zn^{2+} and H_2O was in aqueous electrolyte. Combined, the experimental findings from NMR, FTIR and Raman, together with those from MD simulations, confirm that the GBL additive tunes the electrolyte structure by rearranging the 'Zn^{2+}-H_2O-SO_4^{2-}-GBL' bonding-network as a result of the additional interactions amongst GBL, anions, and cations in $ZnSO_4$ aqueous electrolyte, with GBL additive.

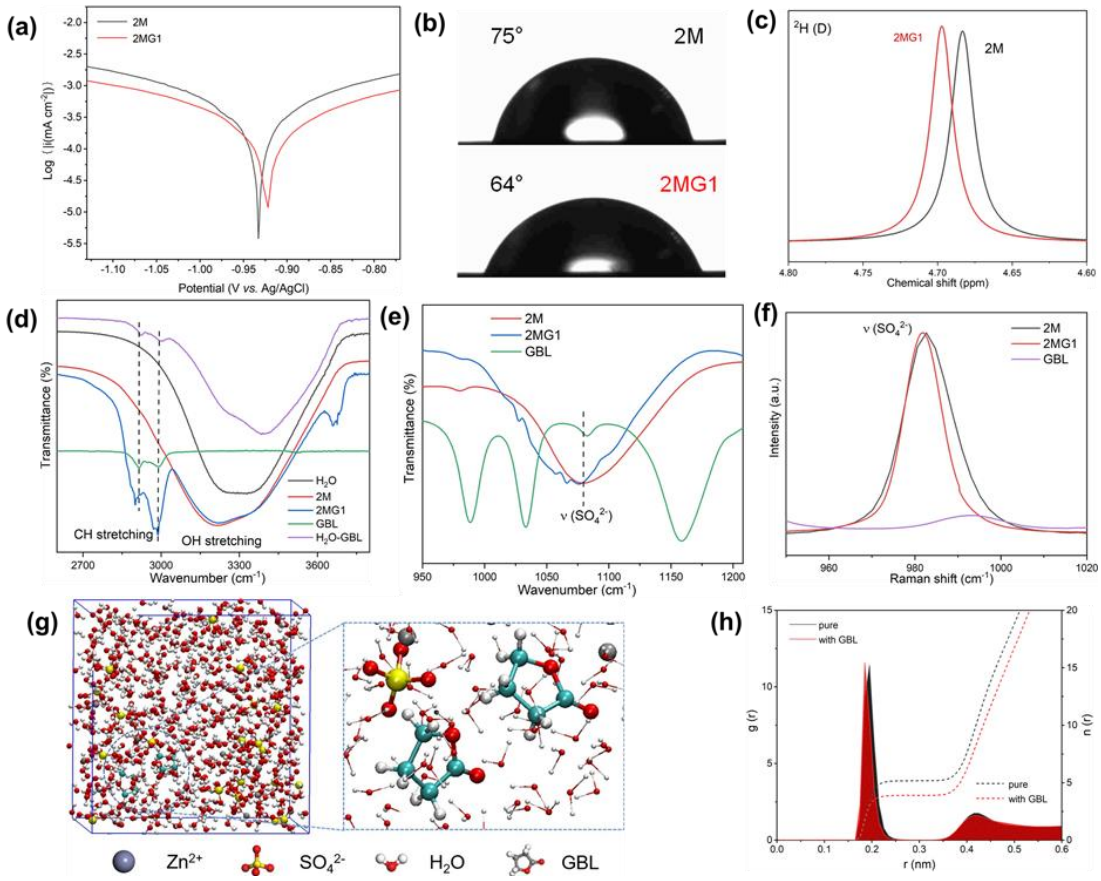

Figure 5.6 Chemical and physical properties of electrolytes. a) Polarization of corrosion curve, b) Contact angle capure of electrolytes with Zn-foil and c) ^2H NMR spectra for 2M and 2MG1 electrolyte. FT-IR spectra for H_2O, H_2O-GBL, GBL, 2M and 2MG1. d) CH- and OH-stretching, e) ν (SO_4^{2-}). f) Raman spectra for 2M, 2MG1 and GBL. g) 3D snapshot with enlarged area of $ZnSO_4$-GBL and h) RDF and coordination number for Zn^{2+}-O (H_2O) from MD simulations.

5.2.6 Quantum Chemistry Computation

The interaction amongst Zn^{2+} ion, H_2O and GBL molecules was assessed *via* quantum chemistry computation. Based on the **binding energy** results of Figure 5.11a, GBL molecules are more preferred to Zn ions than H_2O. The binding energies of both Zn^{2+}-GBL and Zn^{2+}-H_2O are greater than for GBL-H_2O. This finding is consistent with that for the electrolyte structure simulated by MD. Figure 5.11b highlights that following replacing one H_2O molecule with one GBL molecule in the primary solvation shell of Zn^{2+}-H_2O, the regional value of the partial electrostatic potential (ESP) decreases. This evidences that electrostatic repulsion around Zn^{2+} is impacted to give rapid transmission. This finding agreed with that from mean-squared displacement *vs*. time where the diffusion coefficient for Zn^{2+} was increased following addition of GBL (Figure 5.12).

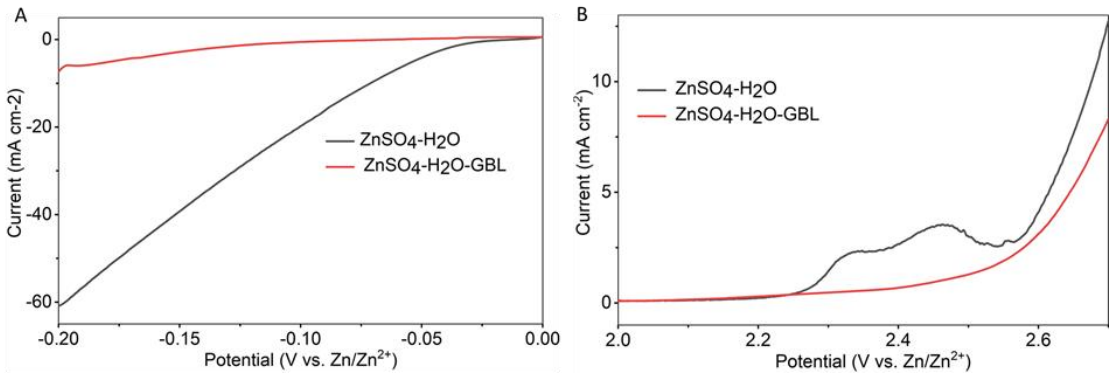

Figure 5.7 (a) Anodic and (b) cathodic LSV response curves for aqueous $ZnSO_4$ and $ZnSO_4$-GBL electrolyte at 1 mV s^{-1}.

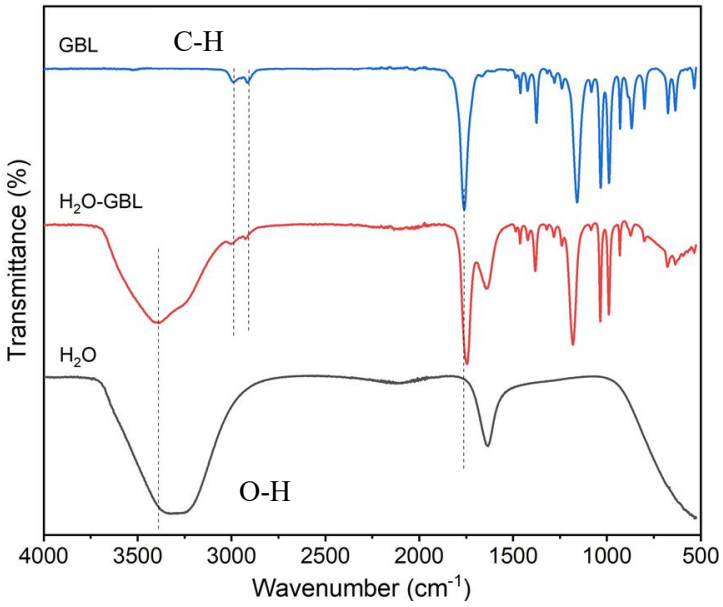

Figure 5.8 FTIR spectroscopy for H_2O, H_2O-GBL and GBL.

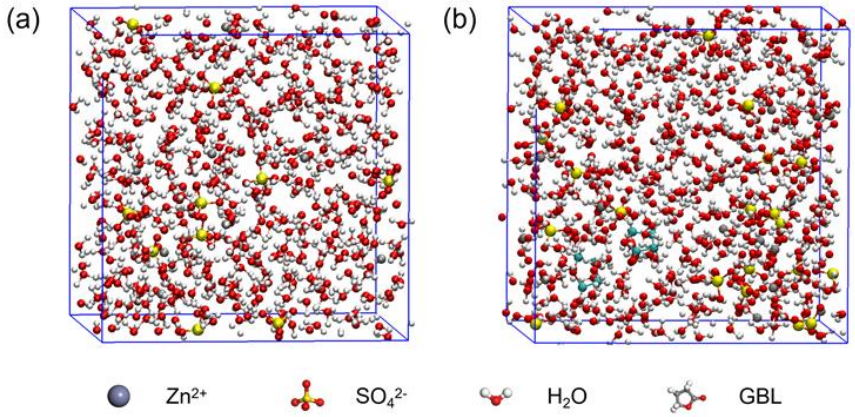

Figure 5.9 3D snapshot for (a) $ZnSO_4$ and (b) $ZnSO_4$-GBL determined from molecular dynamics (MD) simulation.

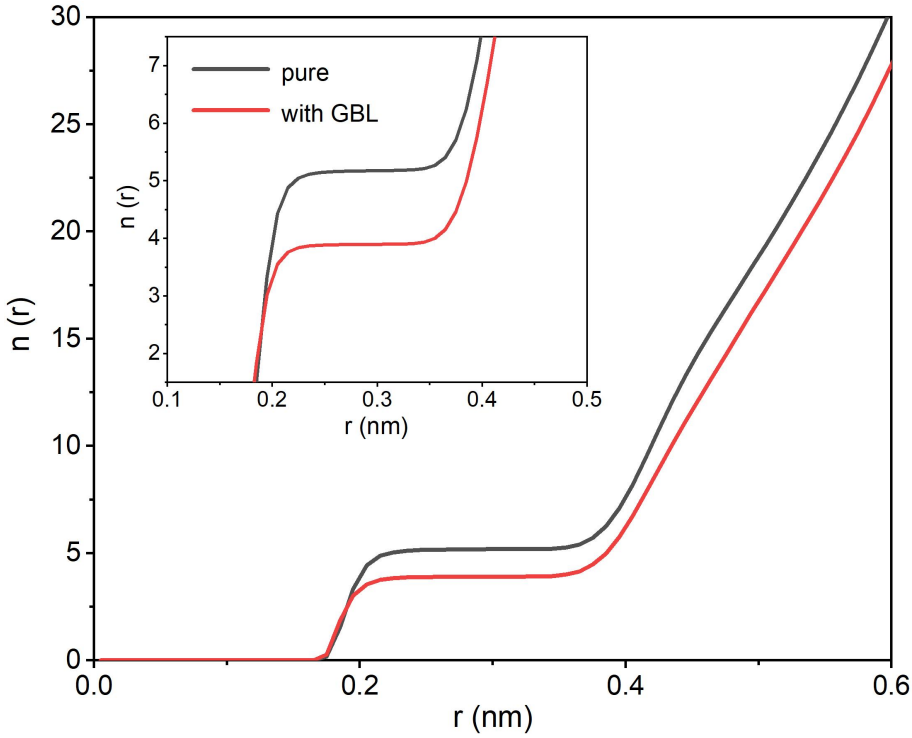

Figure 5.10 Comparison of coordination number of H_2O molecules for Zn^{2+} *vs.* distance in $ZnSO_4$ and $ZnSO_4$-GBL electrolyte from MD simulation. Inset shows comparison at low value of distance.

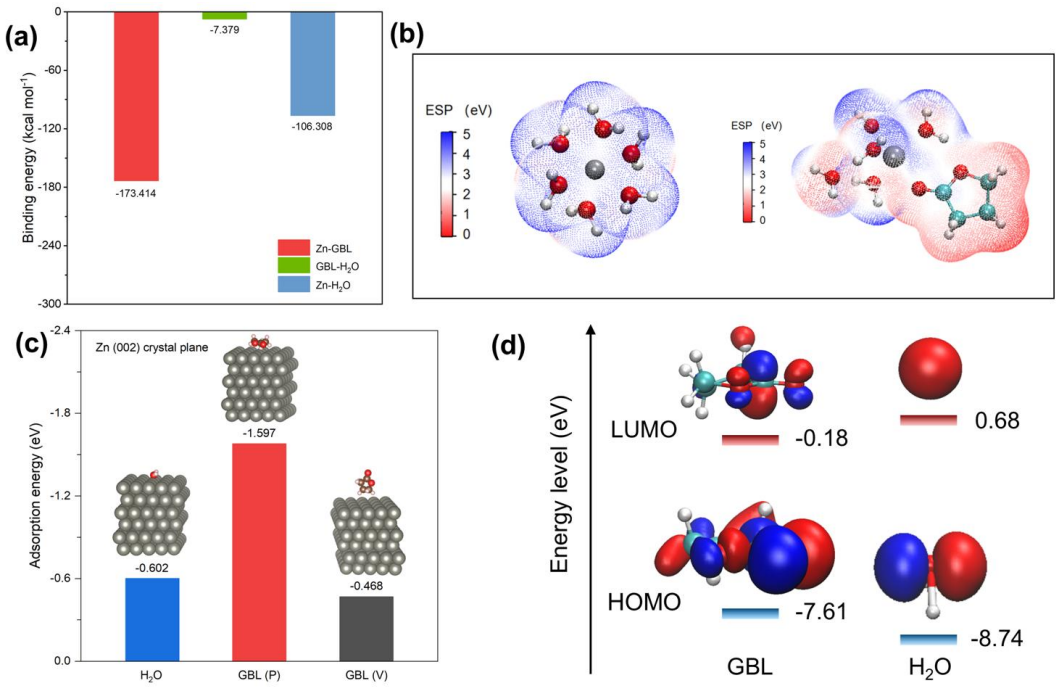

Figure 5.11 Theoretical computations for $ZnSO_4$-GBL electrolyte. (a) Binding energy for Zn^{2+} with differing compounds from DFT computation. (b) Electrostatic potential mapping of

original Zn^{2+}-$6H_2O$ (Left) and Zn^{2+}-$5H_2O$-GBL (Right) solvation structures. (c) Comparison of adsorption energy of H_2O and GBL molecules on Zn (002) crystal plane. Inset shows corresponding absorbed model. (d) LUMO and HOMO iso-surface (iso-value = 0.02 a.u.) of H_2O (Right) and GBL (Left) molecules.

5.2.7 Ab-initio theoretical calculation

The adsorption ability between Zn slab and GBL or H_2O in $ZnSO_4$-GBL electrolyte was studied and compared *via ab-initio* computation. The adsorption of H_2O on the Zn slab ((002) or (101) crystal plane) at possible sites was found to be relatively weak as is shown in Figure 5.11c (Figure 5.13). There exists therefore stronger interplay between Zn and GBL on a parallel position along the Zn surface (GBL (P)). These findings confirm that the GLB molecules are absorbed on the surface of Zn so as to be parallel and to inhibit uncontrolled 2D diffusion and facilitate uniform and compact Zn deposition as was seen in the SEM images. Following addition of GBL the nucleation overpotential increased from 130.86 to 165.03 mV (Figure 5.14), underscoring a slow zinc deposition. The Nyquist plots confirm that there is greater charge transfer resistance, Figure 5.5, as is in agreement with the findings from theoretical computation. Electron gain and loss of absorbed molecules on the Zn surface will impact the deposition behavior of zinc. As is seen in Figure 5.11d, because GBL has a greater highest occupied molecular orbital (HOMO) than that for H_2O, respectively, -7.61 *vs*. -8.74 eV, electrons in GBL are more readily lost when absorbing on the Zn surface. It is apparent from the 3D iso-surface models (Figure 5.15 for ZSC-002 and Figure 5.16 for ZSC-101), together with corresponding 2D contours (Figure 5.17 for ZSC-002 and Figure 5.18 for ZSC-101), that electrons transfer from GBL to Zn *via* adsorption, therefore confirming strong chemical adsorption of GBL.

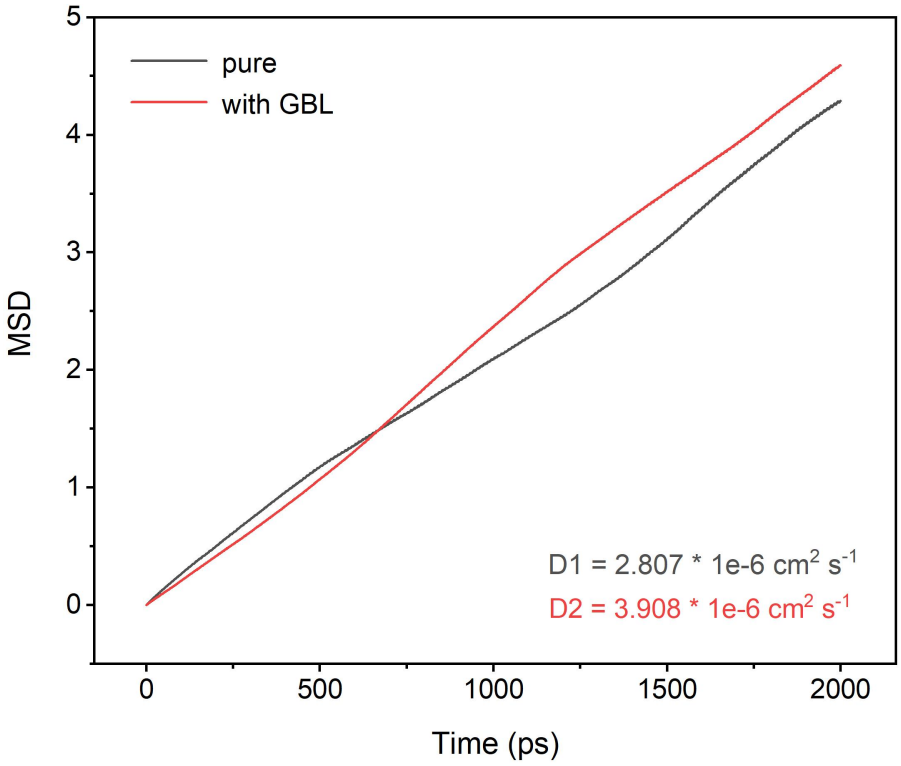

Figure 5.12 MSD as a function of time under $ZnSO_4$ and $ZnSO_4$-GBL electrolyte.

5.2.8 Mechanism Analysis

The overall mechanism postulated for boosted Zn anodes *via* addition of GBL is given in Figure 5.19. During Zn deposition, the hydrated $[Zn(H_2O)_n]^{2+}$ in pure $ZnSO_4$ electrolyte brings significant numbers of H_2O molecules that are reduced to release H_2. The increase in local pH because of H_2 evolution promotes formation of Zn^{2+}-insulating hydroxide zinc-salt passivation on the Zn surface and reduces Zn utilization and cycle life, and promotes Zn dendrite growth. In comparison with addition of GBL, the average coordination number of Zn-H_2O in the primary hydration layer is reduced, and the bonding strength between Zn^{2+} ion and solvated H_2O is weakened. This additional interaction amongst GBL, Zn^{2+}, SO_4^{2-} and H_2O rearranges the 'Zn^{2+}–H_2O–SO_4^{2-}–GBL' bonding-network, reduces water activity and generation of by-product $(Zn(OH)_2)_3(ZnSO_4)(H_2O)_3$. Moreover, GBL molecules absorb on the Zn surface, regulating the homogeneous distribution of Zn^{2+} flux and restricting uncontrolled 2D diffusion that results in uniform and compact Zn deposition. Because of function in both electrolyte structure, and at the electrode-electrolyte interface, the GBL additive boosts reversibility and cycling stability of Zn

anodes. Importantly, because $ZnSO_4$-GBL electrolyte is non-flammable (Figure 5.20), it is practically attractive for large-scale applications. Its high boiling and flash point contribute to safety and reduced risk of explosion including, in electrolyte leakage and thermal runaway.

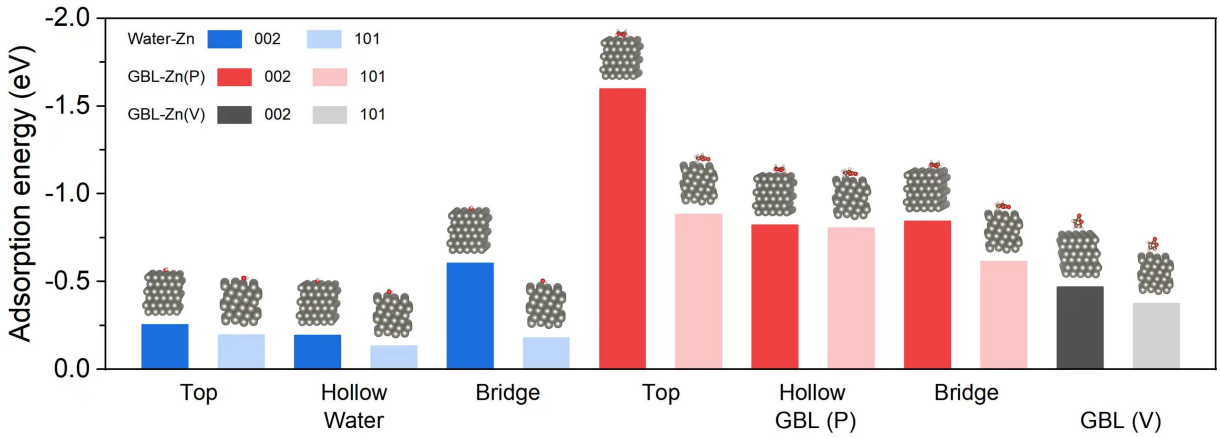

Figure 5.13 Comparison of absorption energy for H_2O and GBL on Zn (002) and Zn (101) crystal plane (more possible absorbed sites for GBL in a parallel direction). Insets show corresponding absorbed models.

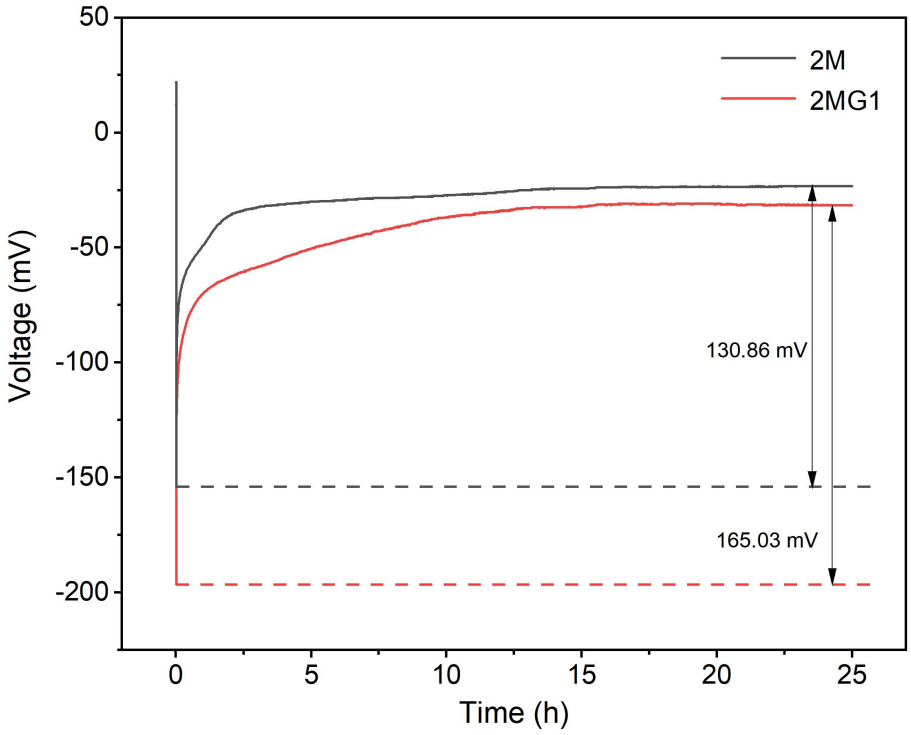

Figure 5.14 Nucleation overpotential curve for Zn|Zn symmetric cells 2M and 2MG1 $ZnSO_4$ electrolyte.

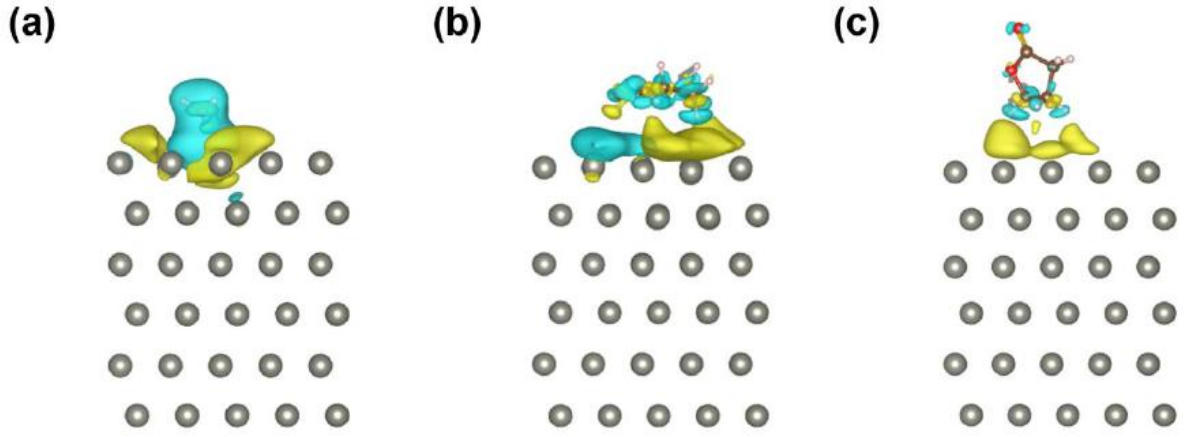

Figure 5.15 Iso-surface model of charge density difference for ZSC-002 with (a) one H_2O, (b) one GBL in a parallel direction and (c) one GBL vertically (iso-value = 2.5 x 10^{-4} e $Bohr^{-3}$).

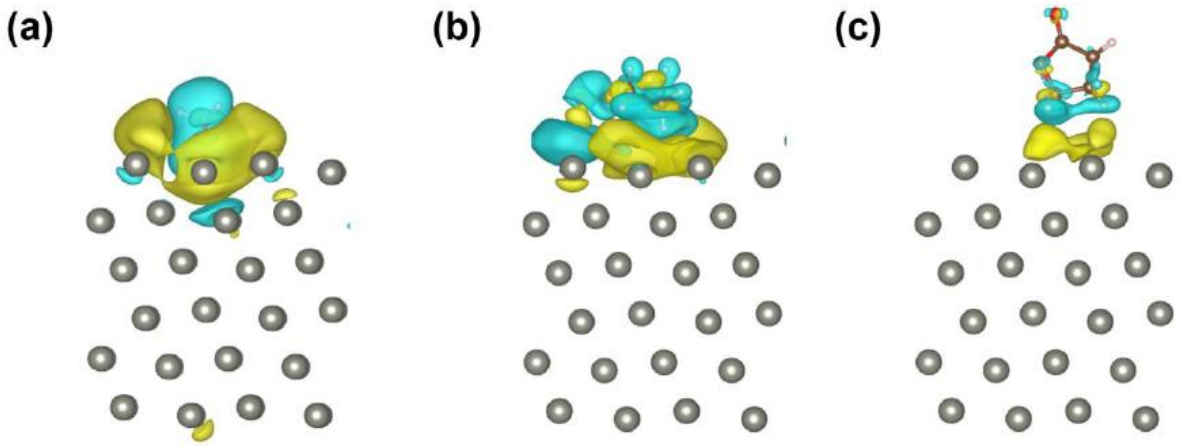

Figure 5.16 Iso-surface model of charge density difference for ZSC-101 with (a) one H_2O, (b) one GBL in a parallel direction and (c) one GBL vertically (iso-value = 2.5 x 10^{-4} e $Bohr^{-3}$).

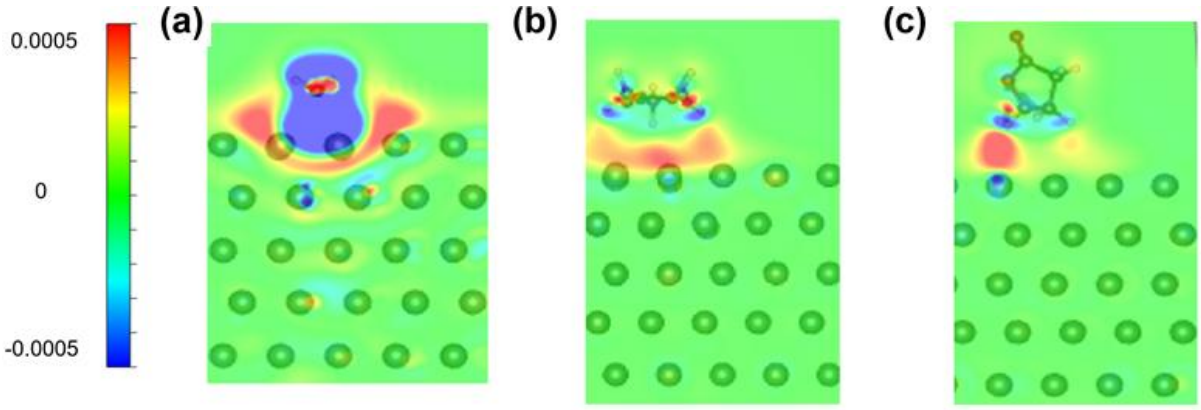

Figure 5.17 2D contours for charge density difference for ZSC-002 with (a) one H_2O, (b) one GBL in a parallel direction and (c) one GBL vertically (iso-value = 2.5 x 10^{-4} e $Bohr^{-3}$).

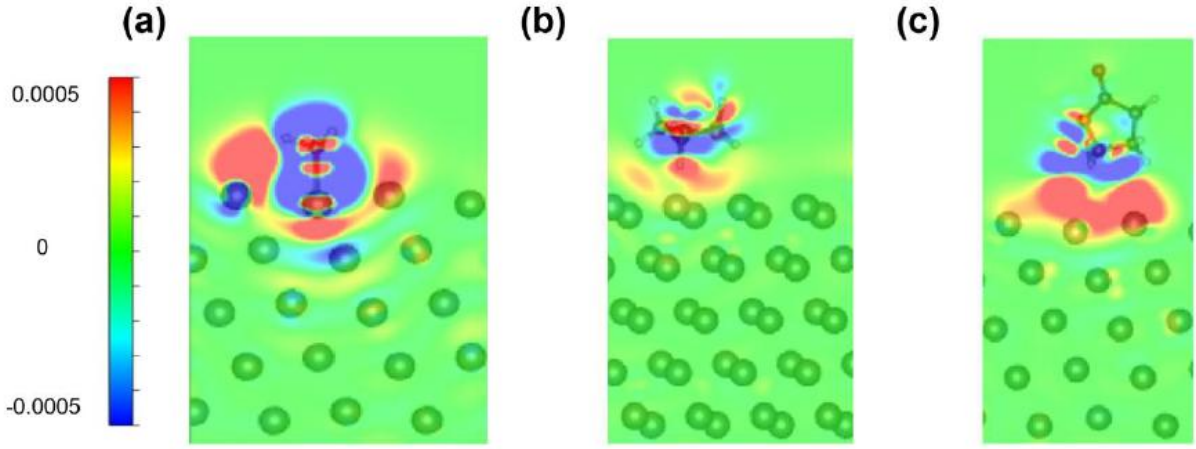

Figure 5.18 2D contours for charge density difference for ZSC-101 with (a) one H_2O, (b) one GBL in a parallel direction and (c) one GBL vertically (iso-value = 2.5 x 10^{-4} e $Bohr^{-3}$).

To assess the practical feasibility of GBL addition in boosting performance of the full cells, Zn-MnO_2 full cells were assembled in which the β-MnO_2. With limited GBL addition, the performance of Zn-MnO_2 cells was boosted as was confirmed in cyclic voltammetry (CV), rate performance from 0.1 to 1 A g^{-1} and galvanostatic charge-discharge (GCD), Figure 5.23 (a-c). The Zn-MnO_2 full cells using $ZnSO_4$-GBL electrolyte exhibited a high capacity of 287 mAh g^{-1} at 0.5 A g^{-1} and good capacity retention of 88 % following 400 cycles, Figure 5.23d. Significantly, the cathode following 50 cycles was retained as the fresh electrode, confirming the stability of MnO_2 in the $ZnSO_4$-GBL electrolyte (Figure 5.24).

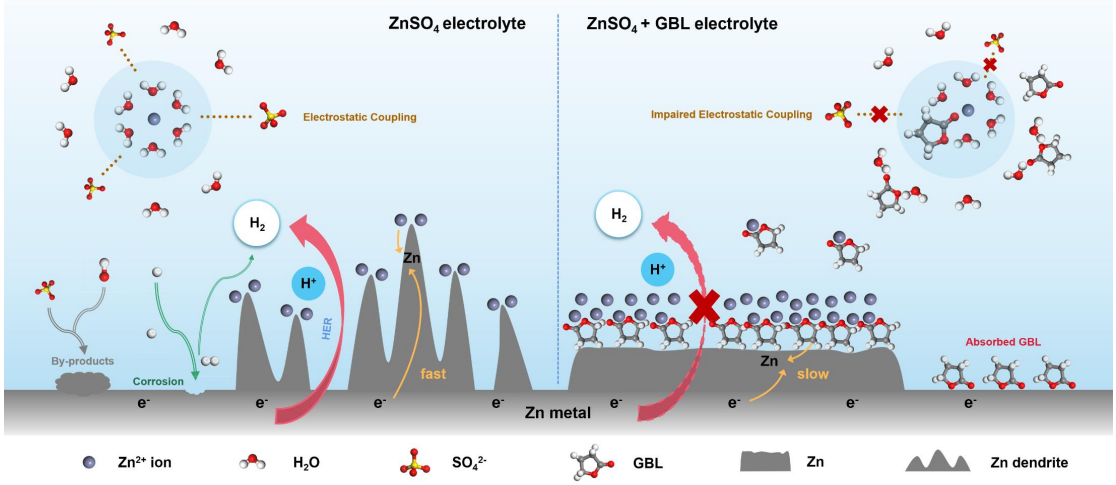

Figure 5.19 Schematic mechanism of some reactions between electrolytes and electrode.

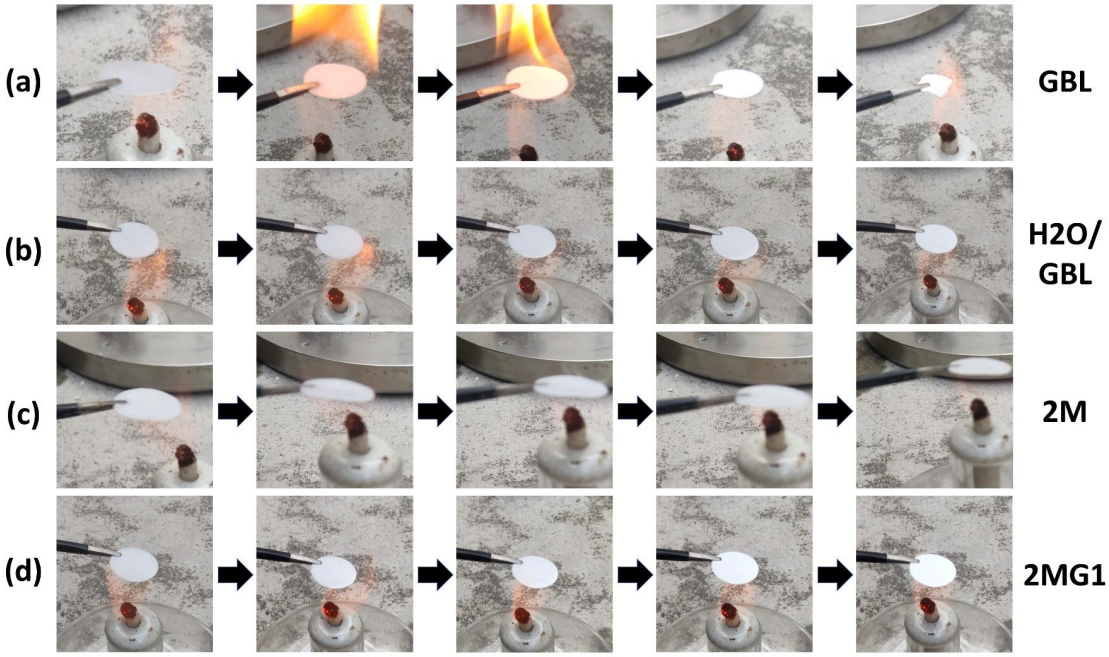

Figure 5.20 Ignition test for a pristine glass-fibre separator with saturated GBL, H_2O/GBL solution, 2M $ZnSO_4$ solution (2M) and 2M $ZnSO_4$-GBL solution (2MG1).

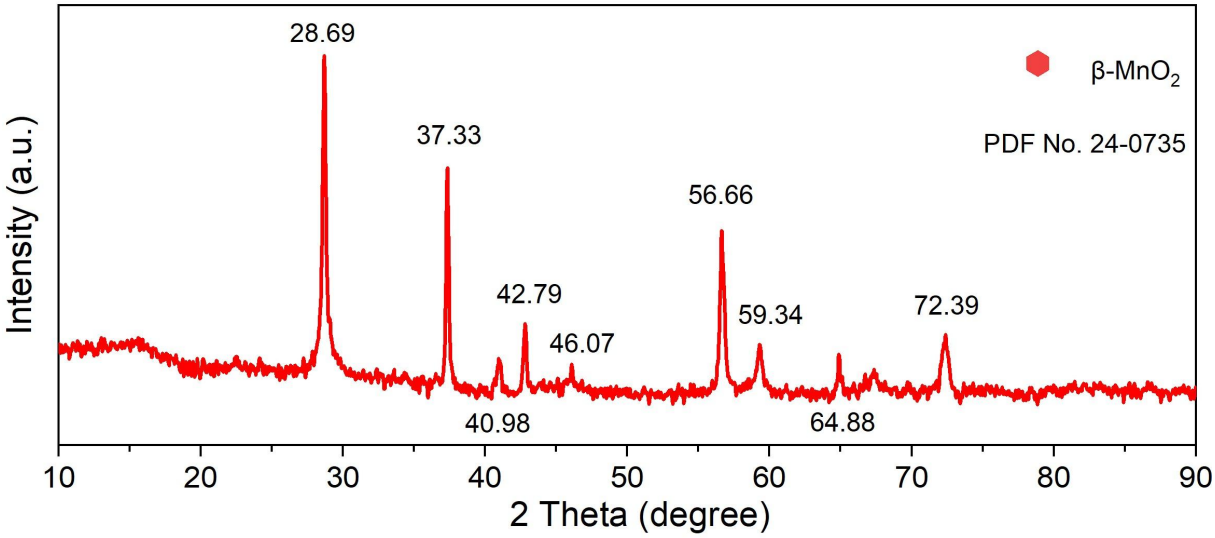

Figure 5.21 XRD pattern for β-MnO_2 nano-rod.

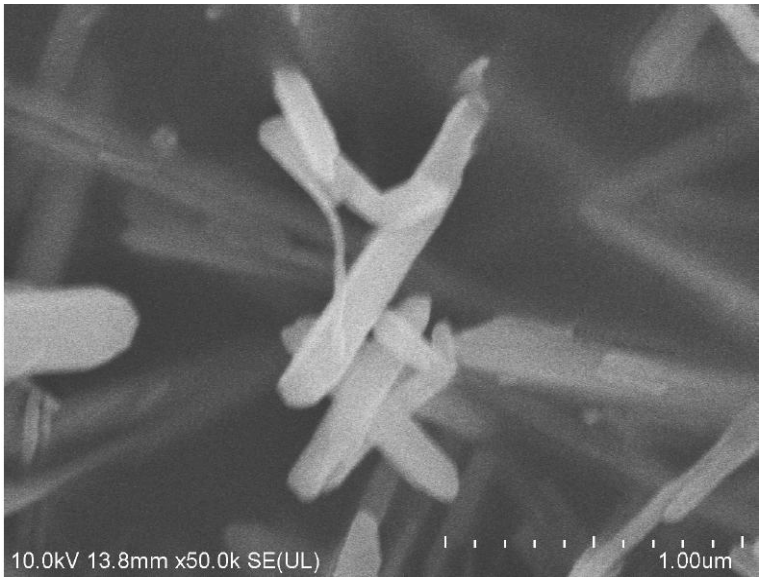

Figure 5.22 SEM image of β-MnO_2 nano-rod.

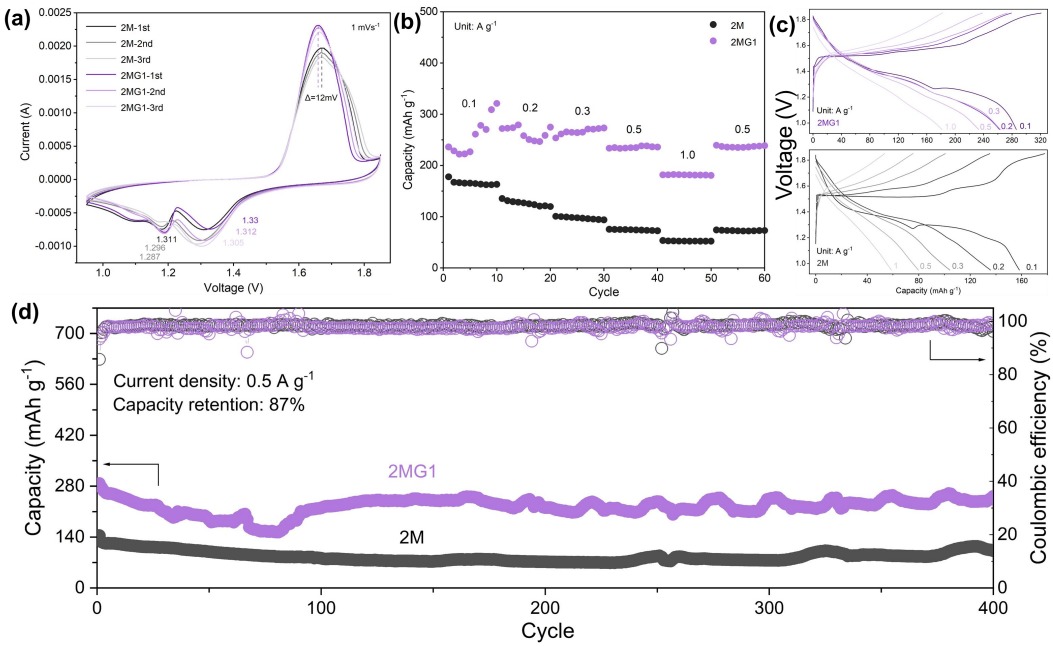

Figure 5.23 Zn||MnO_2 full cell performance. (a) Cyclic voltammetry curves for 1st, 2nd and 3rd cycle. (b) Rate capability at 0.1, 0.2, 0.3, 0.5, and 1 A g^{-1} and back to 0.5 A g^{-1}. c) Galvanostatic Charge and Discharge (GCD) profiles at current density of 0.1, 0.2, 0.3, 0.5 and 1 A g^{-1} and (d) Cycle performance of full cell with 2M and 2MG1 electrolyte.

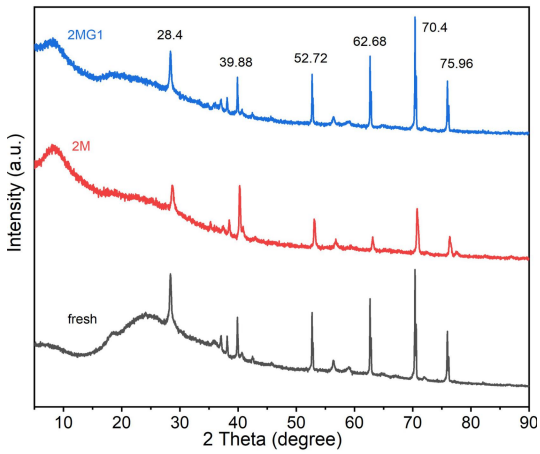

Figure 5.24 XRD pattern confirms stability of MnO_2 electrodes in $ZnSO_4$-GBL electrolyte before and following 50 cycles in electrolyte at 0.5 A g^{-1}.

5.3 Conclusion

Trace low vapour pressure organic solvent, gamma butyrolactone (GBL), is introduced into the typical ZnSO4 electrolyte to achieve highly stable and reversible AZIBs. Experiments (NMR, FTIR, Raman) and theoretical calculations (MD, DFT) suggest that the functional

GBL can not only manipulate the electrolyte structure by rearranging the "Zn^{2+}−H_2O−SO_4^{2-}−GBL" bonding network, but also alter the Zn anode-electrolyte interface by absorbing GBL molecules on Zn surface. Both of the functions help in reducing the water activity, suppressing the corrosion and the generation of by-product, and enabling the uniform and compact Zn deposition. As a result, the Zn anodes run over 2720 cycles (5440 h) with average Coulombic efficiency of 99.9% under 1 mA cm^{-2} and 1 mA h cm^{-2}. The Zn anodes also present a stable and reversible Zn plating/stripping cycling for 1170 h under harsh testing conditions (10 mA cm^{-2} and 10 mA h cm^{-2}). Such the reversibility and stability of Zn anodes are far surpassing that using $ZnSO_4$ electrolyte. Moreover, the Zn-MnO_2 full cells using $ZnSO_4$-GBL electrolyte can deliver a higher capacity of 287 mAh g-1 at 0.5 A g-1 and improved cycling stability (87% capacity retention after 400 cycles) demonstrating the effectiveness of the GBL additive. At higher current density (1A g^{-1} and 5 A g^{-1}), Zn-MnO_2 full cells using $ZnSO_4$-GBL also exhibited more stable and higher capacity cycling performance. Importantly, the 2M ZnSO4-GBL electrolyte is nonflammable, which makes AZIBs promising for large scale applications.

Table 5.1 Boiling point, flash point and solubility (25 °C) of selected rganic additives in electrolyte of AZIBs.

Organic additive	**Boiling point (°C)**	**Flash point (°C)**	**Solubility in water (25 °C)**	**Viscosity (mPa·s)**
AM (acrylamide)	231.7	79.0 ± 19.8	Soluble	
Amino acid Arg	367.6 ± 52	176.1 ± 30.7	Soluble	
AN (acetonitrile)	63.5	5.6	Soluble	0.325-0.375
DME (1,2-dimethoxyethane)	84.5	0.0	Soluble	1.1
DMSO (dimethyl sulfoxide)	189.0 ± 9.0	85.0	Miscible	1.1

Et (erythritol)	330.0	208.7 ± 21.1	Soluble	
EC (ethyl carbonate)	126.8	31.1	Insoluble	0.748-0.868
EMC (ethyl methyl carbonate)	107.5	26.7 ± 7.8	Immiscible	0.65
EG (ethylene glycol)	197.5	108.2 ± 13.0	Miscible	10.38-86.9
Glucose	527.1 ± 50.0	286.7± 26.6	Freely soluble	
Glycerol	290.0	160.0	Soluble	18-243
Maltose	667.9 ± 55.0	357.8 ± 31.5	Very soluble	
Methanol	48.1 ± 3.0	11.1	Miscible	0.5142-0.6405
Na_2EDTA	> 100	325.2	Miscible	
PAM (polyacrylamide)	231.7	79.0 ± 19.8	Soluble	
Sac (saccharin)	438.9 ± 28.0	219.3 ± 24.0	Slightly soluble	
SL (sulfolane)	285.6 ± 8.0	165.6	Soluble	10.286
SN (succinonitrile)	268.5 ± 13.0	141.1 ± 13.7	Slightly soluble	2.591
TEP (triethyl phosphate)	219.3 ± 8.0	115.6	Soluble	N/A
TFEP (tris(2,2,2-trifluoroethyl) phosphate)	176.2 ± 40.0	60.4 ± 27.3	N/A	N/A
TMP (trimethyl phosphate)	197.2	83.7 ± 38.8	Soluble	N/A
Urea	165.1 ± 23.0	53.7± 22.6	Soluble	
GBL (This work)	204	99.2	Miscible	1.7

Table 5.2 Comparison of accumulative plated capacity with current density of selected organic additives in electrolyte of AZIBs.

Organic additive	Current density (mA cm^{-2})	Accumulative plated capacity (mAh cm^{-2})	Reference
AM	10	900	7
	2	380	
	1	340	
Amino acid Arg	5	5500	8
	10	4500	
	1	1475	
AN	1	650	9
	2	600	
	0.5	250	
BIS-TRIS	5	1500	10
	1	625	
CT3G30	2	800	11
DME	2	375	12
DMSO	0.5	250	13
Et_2O	0.2	25	15
EG	2	135	16
Glucose	1	1000	17
	5	687.5	
Glycerol	2	900	18
	1	750	
ILZE	2	1500	19
Maltose	1	600	20
Methanol	1	450	21
$Me_3EtNOTF$	0.5	1500	1

Na_2EDTA	5	5000	22
	2	450	
P_{4441}-TFSI	0.5	1600	23
	1	400	
	2.5	350	
PAM	20	1100	24
	2	170	
	1	90	
PEG-400	2	8000	25
	1	4500	
	0.5	2000	
PEO-4000	1	600	26
PEO-100000	1	1500	27
Saccharin	10	2750	28
	40	1100	
SDBS	0.5	375	29
SL	0.5	200	30
SN	0.2	40	31
	0.05	20	
TBA_2SO_4	10	2000	32
	5	1125	
	2	300	
TC	5	1250	33
	1	1072.5	
	10	850	
TEP	1	750	34

TEP-PC	0.5	650	35
TFEP	0.5	175	36
TMP-DMC/DMF	1	2500	37
Trisodium citrate	5	100	38
Urea	0.1	120	39a
	1	350	39b
GBL	**10**	**5850**	**This work**
	1	**2720**	
	20	**1400**	

Table 5.3 Comparison of Coulombic efficiency (CE) and cumulaltive plated capacity for Zn half cells with selected organic additives in electrolyte of AZIBs.

Organic additive	**Cumulative plated capacity ($Ah\ cm^{-2}$)**	**CE (%)**	**Reference**
AM	0.04	N/A	7
Amino acid Arg	0.325	98.3[a]	8
AN	0.3	99.3[a]	9
BIS-TRIS	0.4	98.5[a]	10
DME	0.156	N/A	12
DMSO	0.2	99.5[a]	13
EG	0.12	98[a]	16
Glucose	0.1	97.3[a]	17
Glycerol	0.5	98.3[a]	18
ILZE	0.3	99.36[b]	19
Maltose	0.032	99.7[a]	20
Methanol	0.45	99.7[a]	21

$Me_3EtNOTF$	0.5	99.8[a]	1
Na_2EDTA	0.7	99.5[a]	22
P_{4441}-TFSI	N/A	98.1[a]	23
PEO-4000	0.35	98.7[b]	26
PEO-100000	1.5	99.5[b]	27
Saccharin	0.5	99.6[a]	28
SL	0.05	98[b]	30
SN	0.025	98.4[a]	31
TBA_2SO_4	N/A	98[b]	32
TC	750 cycles at 1 mA cm^{-2}	97.7[b]	33
TEP	0.126	99.5[a]	34
TEP-PC	N/A	97.7[b]	35
TFEP	0.175	99.1[a]	36
TMP	5	99.57[a]	37
Urea	N/A	96.2[b]	39a
GBL	**2.722**	**99.9[a]**	**This work**

[a] average CE, [b] reaches until stable CE, N/A: not available.[2]

References

[1] L. Cao, D. Li, T. Pollard, T. Deng, B. Zhang, C. Yang, L. Chen, J. Vatamanu, E. Hu, M. J. Hourwitz, L. Ma, M. Ding, Q. Li, S. Hou, K. Gaskell, J. T. Fourkas, X.-Q. Yang, K. Xu, O. Borodin, C. Wang, *Nat. Nanotechnol.* **2021**, *16*, 902-910.

[2] A. Bernardi, R. Faller, D. Reith, K. N. Kirschner, *Softwarex* **2019**, *10*, 100241.

[3] a) W. L. Jorgensen, J. Tirado-Rives, *Proc. Natl. Acad. Sci. U.S.A.* **2005**, *102*, 6665; b) L. S. Dodda, J. Z. Vilseck, J. Tirado-Rives, W. L. Jorgensen, *J. Phys. Chem. B* **2017**, *121*, 3864-3870.

[4] G. Bussi, D. Donadio, M. Parrinello, *J. Chem. Phys.* **2007**, *126*, 014101.

[5] H. J. C. Berendsen, J. P. M. Postma, W. F. van Gunsteren, A. DiNola, J. R. Haak, *J. Chem. Phys.* **1984**, *81*, 3684-3690.

[6] a) P. E. Blöchl, *Phys. Rev. B* **1994**, *50*, 17953-17979; b) B. Hammer, L. B. Hansen, J. K. Nørskov, *Phys. Rev. B* **1999**, *59*, 7413-7421; c) G. Kresse, D. Joubert, *Phys. Rev. B* **1999**, *59*, 1758-1775; d) J. Tao, J. P. Perdew, V. N. Staroverov, G. E. Scuseria, Phys. Rev. Lett. **2003**, *91*, 146401; e) S. Lebègue, O. Eriksson, *Phys. Rev. B* **2009**, *79*, 115409.

[7] X. Zeng, X. Meng, W. Jiang, M. Ling, L. Yan, C. Liang, *Electrochim. Acta* **2021**, *378*, 138106.

[8] H. Lu, X. Zhang, M. Luo, K. Cao, Y. Lu, B. B. Xu, H. Pan, K. Tao, Y. Jiang, *Adv. Funct. Mater.* **2021**, *31*, 2103514.

[9] J. Shi, K. Xia, L. Liu, C. Liu, Q. Zhang, L. Li, X. Zhou, J. Liang, Z. Tao, *Electrochim. Acta* **2020**, *358*, 136937.

[10] M. Luo, C. Wang, H. Lu, Y. Lu, B. B. Xu, W. Sun, H. Pan, M. Yan, Y. Jiang, *Energy Stor. Mater.* **2021**, *41*, 515-521.

[11] M. Chen, J. Chen, W. Zhou, X. Han, Y. Yao, C.-P. Wong, *Adv. Mater.* **2021**, *33*, 2007559.

[12] J. Cui, X. Liu, Y. Xie, K. Wu, Y. Wang, Y. Liu, J. Zhang, J. Yi, Y. Xia, *Mater. Today Energy* **2020**, *18*, 100563.

[13] L. Cao, D. Li, E. Hu, J. Xu, T. Deng, L. Ma, Y. Wang, X.-Q. Yang, C. Wang, *J. Am. Chem. Soc.* **2020**, *142*, 21404-21409.

[14] Z. Huang, T. Wang, X. Li, H. Cui, G. Liang, Q. Yang, Z. Chen, A. Chen, Y. Guo, J. Fan, C. Zhi, *Adv. Mater.* **2021**, *n/a*, 2106180.

[15] W. Xu, K. Zhao, W. Huo, Y. Wang, G. Yao, X. Gu, H. Cheng, L. Mai, C. Hu, X. Wang, *Nano Energy* **2019**, *62*, 275-281.

[16] N. Chang, T. Li, R. Li, S. Wang, Y. Yin, H. Zhang, X. Li, *Energy Environ. Sci.* **2020**, *13*, 3527-3535.

[17] P. Sun, L. Ma, W. Zhou, M. Qiu, Z. Wang, D. Chao, W. Mai, *Angew. Chem. Int. Ed.* **2021**, *60*, 18247-18255.

[18] Y. Zhang, M. Zhu, K. Wu, F. Yu, G. Wang, G. Xu, M. Wu, H.-K. Liu, S.-X. Dou, C. Wu, Journal of Materials Chemistry A **2021**, *9*, 4253-4261.

[19] L. Ma, S. Chen, N. Li, Z. Liu, Z. Tang, J. A. Zapien, S. Chen, J. Fan, C. Zhi, *Adv. Mater.* **2020**, *32*, 1908121.

[20] W. Chen, S. Guo, L. Qin, L. Li, X. Cao, J. Zhou, Z. Luo, G. Fang, S. Liang, *Adv. Funct. Mater.* **2022**, *n/a*, 2112609.

[21] J. Hao, L. Yuan, C. Ye, D. Chao, K. Davey, Z. Guo, S.-Z. Qiao, *Angew. Chem. Int. Ed.* **2021**, *60*, 7366-7375.

[22] S.-J. Zhang, J. Hao, D. Luo, P.-F. Zhang, B. Zhang, K. Davey, Z. Lin, S.-Z. Qiao, *Adv. Energy Mater.* **2021**, *11*, 2102010.

[23] L. Ma, T. P. Pollard, Y. Zhang, M. A. Schroeder, M. S. Ding, A. V. Cresce, R. Sun, D. R. Baker, B. A. Helms, E. J. Maginn, C. Wang, O. Borodin, K. Xu, *Angew. Chem. Int. Ed.* **2021**, *60*, 12438-12445.

[24] Q. Zhang, J. Luan, L. Fu, S. Wu, Y. Tang, X. Ji, H. Wang, *Angew. Chem. Int. Ed.* **2019**, *58*, 15841-15847.

[25] Y. Wu, Z. Zhu, D. Shen, L. Chen, T. Song, T. Kang, Z. Tong, Y. Tang, H. Wang, C. S. Lee, *Energy Stor. Mater.* **2022**, *45*, 1084-1091.

[26] M. Yan, C. Xu, Y. Sun, H. Pan, H. Li, *Nano Energy* **2021**, *82*, 105739.

[27] Y. Jin, K. S. Han, Y. Shao, M. L. Sushko, J. Xiao, H. Pan, J. Liu, *Adv. Funct. Mater.* **2020**, *30*, 2003932.

[28] C. Huang, X. Zhao, S. Liu, Y. Hao, Q. Tang, A. Hu, Z. Liu, X. Chen, *Adv. Mater.* **2021**, *33*, 2100445.

[29] J. Hao, J. Long, B. Li, X. Li, S. Zhang, F. Yang, X. Zeng, Z. Yang, W. K. Pang, Z. Guo, *Adv. Funct. Mater.* **2019**, *29*, 1903605.

[30] X. Lin, G. Zhou, M. J. Robson, J. Yu, S. C. T. Kwok, F. Ciucci, *Adv. Funct. Mater.* **2021**, *n/a*, 2109322.

[31] W. Yang, X. Du, J. Zhao, Z. Chen, J. Li, J. Xie, Y. Zhang, Z. Cui, Q. Kong, Z. Zhao, C. Wang, Q. Zhang, G. Cui, *Joule* **2020**, *4*, 1557-1574.

[32] A. Bayaguud, X. Luo, Y. Fu, C. Zhu, *ACS Energy Lett.* **2020**, *5*, 3012-3020.

[33] R. Yao, L. Qian, Y. Sui, G. Zhao, R. Guo, S. Hu, P. Liu, H. Zhu, F. Wang, C. Zhi, C. Yang, *Adv. Energy Mater.* **2022**, *12*, 2102780.

[34] S. Liu, J. Mao, W. K. Pang, J. Vongsvivut, X. Zeng, L. Thomsen, Y. Wang, J. Liu, D. Li, Z. Guo, *Adv. Funct. Mater.* **2021**, *31*, 2104281.

[35] X. Qiu, N. Wang, X. Dong, J. Xu, K. Zhou, W. Li, Y. Wang, *Angew. Chem. Int. Ed.* **2021**, *60*, 21025-21032.

[36] L. Cao, D. Li, E. Hu, J. Xu, T. Deng, L. Ma, Y. Wang, X.-Q. Yang, C. Wang, *J. Am. Chem. Soc.* **2020**, *142*, 21404-21409.

[37] A. Naveed, H. Yang, Y. Shao, J. Yang, N. Yanna, J. Liu, S. Shi, L. Zhang, A. Ye, B. He, J. Wang, *Adv. Mater.* **2019**, *31*, 1900668.

[38] N. Wang, S. Zhai, Y. Ma, X. Tan, K. Jiang, W. Zhong, W. Zhang, N. Chen, W. Chen, S. Li, G. Han, Z. Li, *Energy Stor. Mater.* **2021**, *43*, 585-594.

[39] a) J. Zhao, J. Zhang, W. Yang, B. Chen, Z. Zhao, H. Qiu, S. Dong, X. Zhou, G. Cui, L. Chen, *Nano Energy* **2019**, *57*, 625-634; b) Z. Hou, M. Dong, Y. Xiong, X. Zhang, H. Ao, M. Liu, Y. Zhu, Y. Qian, *Small* **2020**, *16*, 2001228.

CHAPTER 6 Pyrrolidone as Electrolyte additives for aqueous Zn-ion batteries

6.1 Introduction

To achieve carbon neutrality by 2050, a significantly increased use of clean energy technologies including, electric vehicles (EVs) and energy efficient building retrofits, will be needed. Storage of energy is critical to underpinning sustainable consumer electronics, transport and industry smart-grids. Li-ion batteries have been dominant. However, significant drawbacks include relative high cost and low safety.[1,2] Aqueous rechargeable zinc-ion batteries (AZIBs) have attracted research attention for large-scale energy storage because of advantageous, high safety, low toxicity, abundance of materials and unique properties of zinc including, low redox potential (- 0.7626 V *vs*. standard hydrogen electrode), high gravimetric capacity (820 mA h g^{-1}), and high volumetric capacity (5585 mAh cm^{-3}).[3-6] Drawbacks however include, Zn dendrite formation, corrosion and by-product and H_2 evolution that mitigate against sufficiently high reversibility and stability.

Electrochemical behavior of Zn metal is determined principally by the properties of the aqueous electrolyte and electrode-electrolyte interface. These are closely related to the solvation structures of hydrated Zn^{2+} ions, anions, and hydrogen bonding-network. Therefore, a reconstruction of the chemical bonding-network and solvation structure of cations and anions in aqueous electrolyte, and optimization of the electrode-electrolyte interface can be used to practically regulate the performance of Zn anodes. Proposals to tune the solvation structure of electrolyte and boost reversibility of Zn anodes included, high concentration, [7-9] hydrate/deep-in-eutectic, [10-14] and aqueous/organic hybrid electrolytes [15-18]. Drawbacks from these electrolytes have included however, high cost, unwanted low ionic conductivity and high viscosity. The addition of organics has been reported because these species, as liquids or solids can interact with Zn^{2+} and H_2O molecules to change the solvated structure of Zn

hydration and the hydrogen bonding-network without high concentration of slats or solvents. [19-29] However, the electrochemical performance of these Zn anodes remains poor, especially under harsh condition of high current density/capacity of up to 10 mA cm^{-2} and 10 mAh cm^{-2}. Additionally, particular organic molecules are highly flammable. Although the nonflammable nature of water assures safety of AZIBs, the hydrogen evolution reaction (HER) and/or oxygen evolution reaction (OER) during battery cycling and/or idling, lowers the Coulombic efficiency (CE) and cycle life and may cause explosions. Any application to AZIBs must therefore suppress these reactions without reducing practical safety. A nonflammable and/or low vapor pressure solvent is necessarily required therefore to regulate solvation structure and interface so as to boost reversibility and stability of Zn anodes under harsh conditions.

Because Pyrrolidone (Pr) has a high boiling and flash temperature, respectively, T_b = 250 °C and T_f = 138 °C, it is practically attractive as an electrolyte additive for rechargeable batteries. Pyrrolidone-based electrolytes have in fact been used in Li-ion batteries over a range of temperature. [30,31]

Here Pyrrolidone was adopted as a new electrolyte additive to $ZnSO_4$ electrolyte. It was postulated that through adjusting the mole ratio of Pyrrolidone in Pyrrolidone-based electrolytes, 3% Pyrrolidone, in 2 M $ZnSO_4$ would significantly boost Zn plating/stripping performance under different current density. Experiment and theoretical computation confirmed that the functional Pyrrolidone additive weakens the bonding strength between Zn^{2+} ion and solvated H_2O and rearranges the 'Zn^{2+}–H_2O–SO_4^{2-}–Pyrrolidone' bonding-network to reduce water activity and suppress corrosion and generation of by-product. The Zn metal surface absorbs Pyrrolidone rather than H_2O which restricts uncontrollable 2D diffusion and gives rise to uniform deposition. Thus, the Zn-MnO_2 full cells using $ZnSO_4$-Pyrrolidone electrolyte exhibited superior performance to that using Pyrrolidone -free electrolyte. Importantly, because 2 M $ZnSO_4$-Pyrrolidone electrolyte is nonflammable it makes AZIBs practically promising for large-scale application.

6.2 Results and Discussion

6.2.1 Stability of the Zn Electrode

The stability of the Zn electrode in aqueous electrolyte with and without Pyrrolidone was compared in Zn||Zn symmetric cells, Figure 6.1a. Pyrrolidone addition resulted in excellent stability of Zn in Zn||Zn in normal to harsh condition. With an optimized electrolyte of 2 M $Zn(SO_4)_2$ with 3% Pyrrolidone in amount (2MP3), the Zn symmetrical cell exhibited highly stable cycling performance for over 1200 h at a current density of 1 mA cm^{-2} and an areal capacity of 1 mA h cm^{-2}, significantly however, the 2M $ZnSO_4$ electrolyte failed following 700 h, Figure 1a. Under harsh conditions of 10 mA cm^{-2} and 10 mA h cm^{-2}, the Zn electrode with 2MP3 electrolyte remained stable and exhibited reversible Zn plating/stripping for 456 h. Importantly, this is significantly longer than that in the blank electrolyte of 70 h, Figure 1b. At a high 20 mA cm^{-2} and 20 mA h cm^{-2}, Figure 6.1c, the Zn electrode in the symmetrical cell with optimized electrolyte exhibited stable cycling for about 100 h, whilst the Zn electrode in the blank electrolyte exhibited a short-circuit in < 25 h. These findings strongly evidence the significant boost in reversibility and stability of the Zn anodes resulting from Pyrrolidone addition.

6.2.2 Reversibility of the Zn Electrode

Reversibility of the Zn electrode in aqueous electrolyte with and without GBL was compared in Zn||Cu asymmetric cells, Figure 6.2. It was found that there are marginal differences in the initial Coulombic efficiency, that increases with increasing $ZnSO_4$ concentration i.e., 2MP3 >= 2MP1 >= 2MP5 > 2M (Figure 6.2a). The addition of less or more Pyrrolidone, reduced the initial Coulombic efficiency (Figure 6.2a). The presence of 3% Pyrrolidone boosted the initial Coulombic efficiency to 98.5 % at 1 mA cm^{-2} and 1 mA h cm^{-2}, and the average CE increased to 99.9 % for over 2720 cycles (5440 h), Figure 6.2a. In comparison, the 2 M $ZnSO_4$ electrolyte

exhibited a low initial Coulombic efficiency of 91.1 % and an average CE of 99.6 %, noticeably failing at the 222th cycle, Figures 6.2d, 6.2e.

Addition of Pyrrolidone concomitantly tuned Zn deposition morphology and suppressed corrosion. The scanning electron microscopy (SEM) images confirmed that following 50 cycles with Zn||Cu cells, the Zn surface in the $ZnSO_4$ electrolyte become an apparent scattered microporous structure, Figure 6.2e, whilst there remained a planar stage structure on the Zn surface in the $ZnSO_4$-Pyrrolidone electrolyte; this formed a densely integrated binding network, Figure 6.2f. A reduced hydrogen and oxygen evolution current obtained from linear sweep voltammetry (LSV) curves confirm the impact on boosting reversibility and stability *via* controlled manipulation with Pyrrolidone additive. (Figure 6.3)

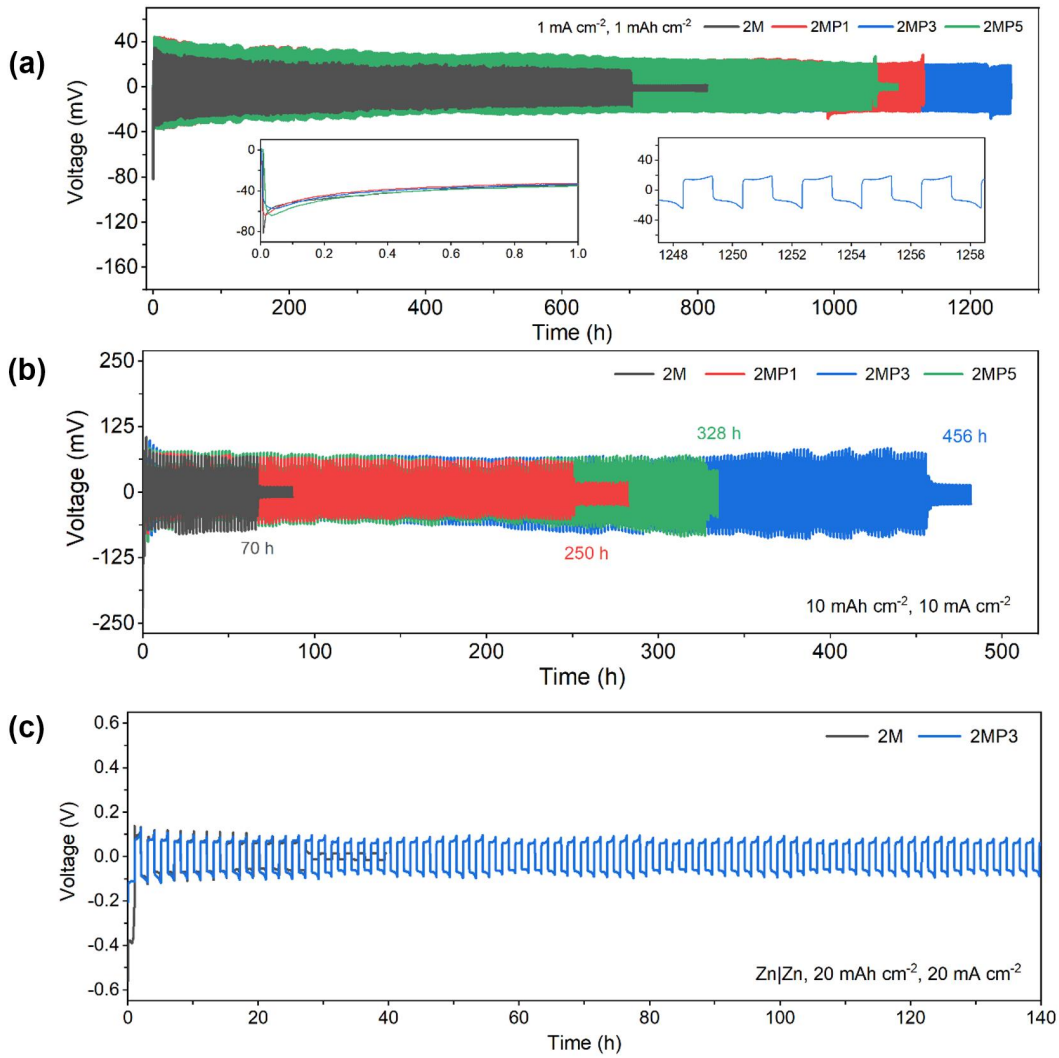

Figure 6.1 Zn|Zn symmetric cells containing 2M $ZnSO_4$ with different amount of Pyrrolidone at the areal capacity and current density of (a) 1 mAh cm^{-2} at 1 mA cm^{-2}; (b) 10 mAh cm^{-2} at 10 mA cm^{-2} and (c) 20 mAh cm^{-2} at 20 mA cm^{-2}

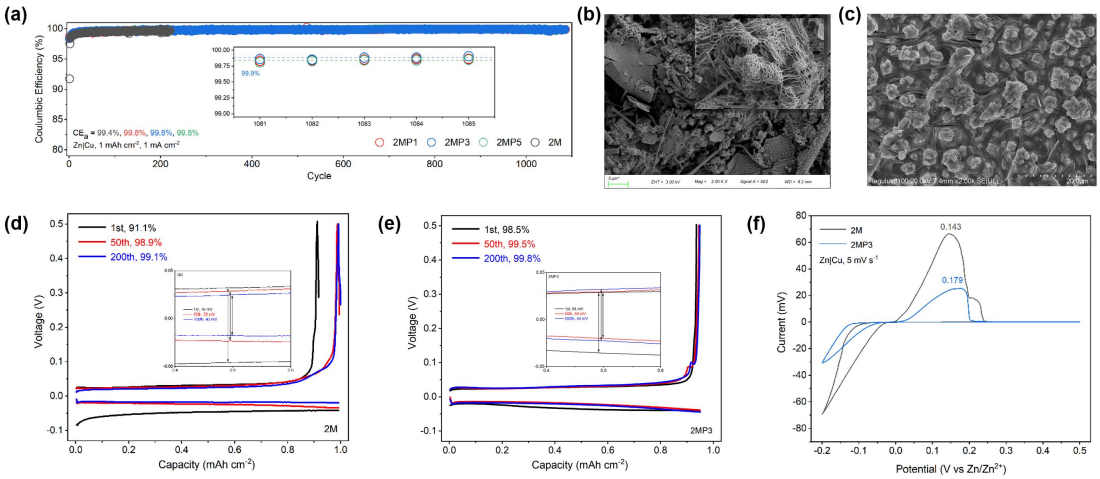

Figure 6.2 Zn|Cu half cells performance and properties. (a) Coulombic efficiency of the cells in 2M $ZnSO_4$ electrolytes with different amount of Pyrrolidone. The half cells after 50 cycles at 1 mAh cm^{-2} at 1 mA cm^{-2}. Charge/discharge voltage profiles of half cells with (b) 2M and (c) 2MP3 electrolytes at 1st, 50th and 200th cycles with magnified views of corresponding cycles in the potential range between 0.4 and 0.6 V at a current density of 1 mA cm^{-2}. SEM images of the Zn foils in (d) 2M and (e) 2MP3 electrolytes for half cells after 50 cycles. (f) Cyclic voltammetry at 5 mV s^{-1}.

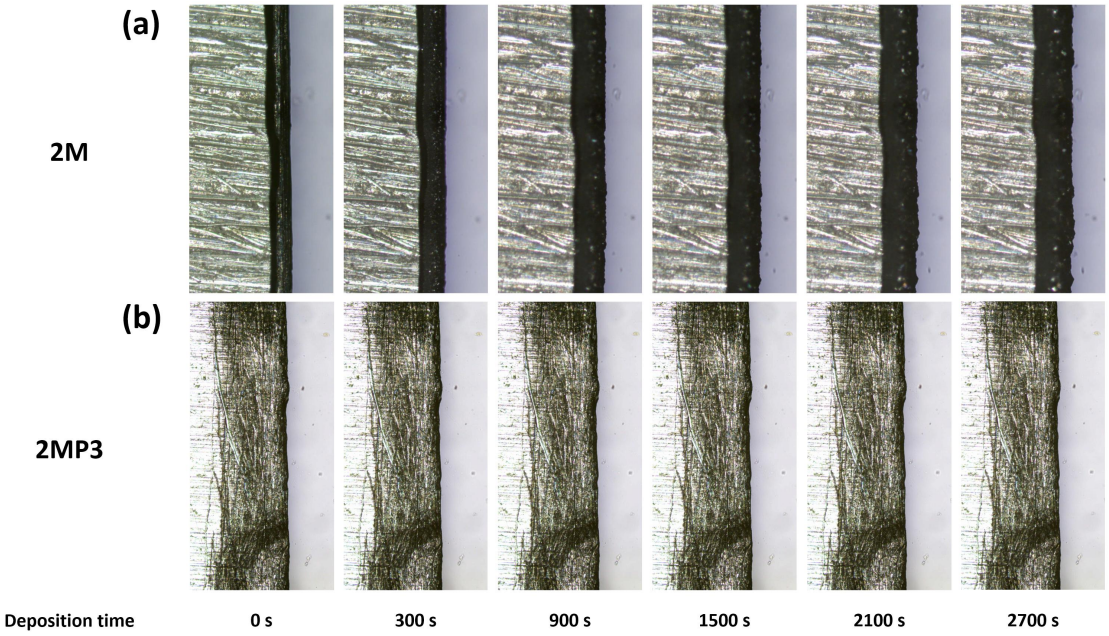

Figure 6.3 *In-situ* optical microscopic images for Zn deposition process at the current density of 5 mA cm^{-2}.

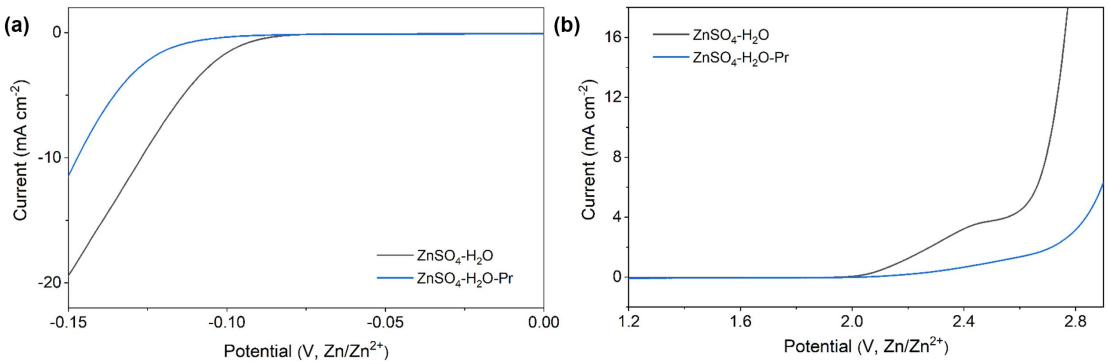

Figure 6.4 (a) Anodic and (b) cathodic LSV response curves for aqueous $ZnSO_4$ and $ZnSO_4$-Pyrrolidone electrolyte at 1 mV s^{-1}.

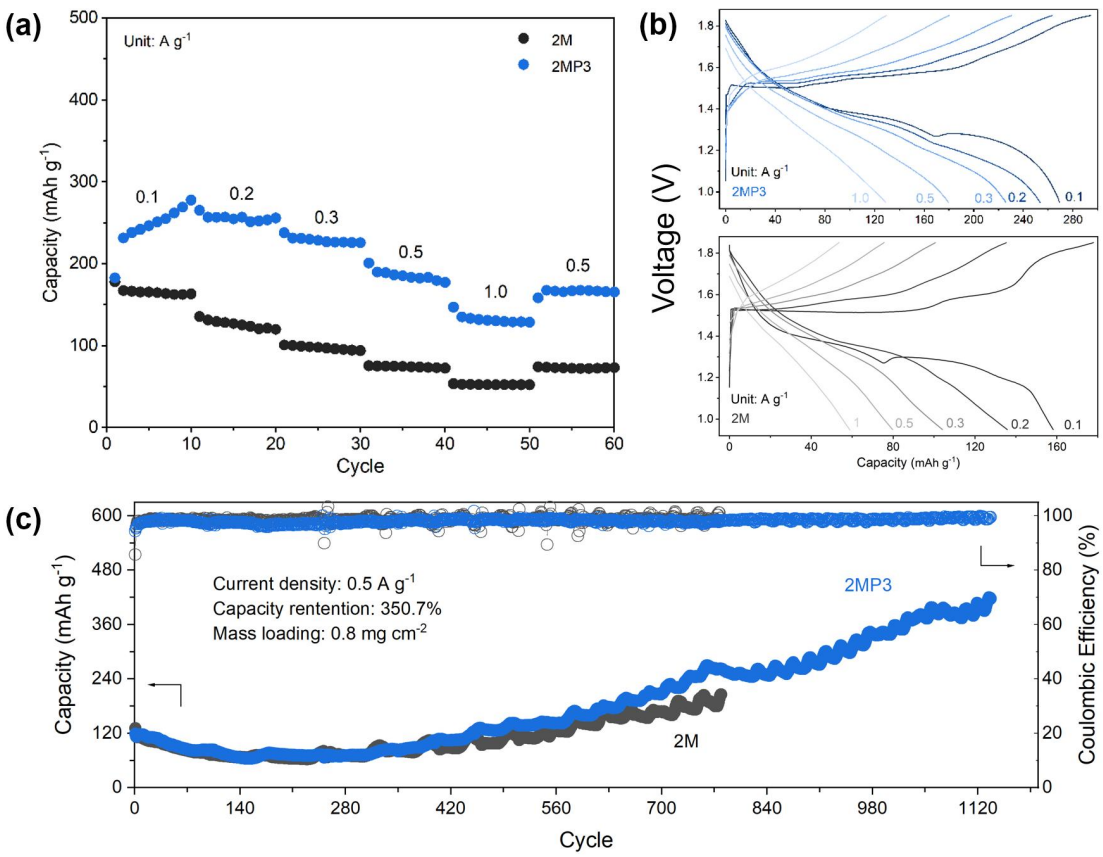

Figure 6.5 Zn|MnO_2 full cells performance. (a) Rate capability at 0.1, 0.2, 0.3, 0.5, 1 A g^{-1} and back to 0.5 A g^{-1}; (b) Galvanostatic Charge Discharge (GCD) profiles at different current density 0.1, 0.2, 0.3, 0.5 and 1 A g^{-1}; and (d) Cycle performance at 1 A g^{-1} (activation process: 0.1 A g^{-1} for 10 cycles).

6.2.3 Chemical and physical properties of electrolytes

Judiciously combined experimental characterizations including Fourier transform infrared spectroscopy (FTIR) and Raman spectroscopy were used to determine the underlying mechanism for Zn metal in $ZnSO_4$-Pyrrolidone. The addition of Pyrrolidone weakens the solvation coordination between Zn^{2+} and water. This finding was confirmed *via* FTIR (Figure 6.5) and Raman (Figure 6.6) results. Compared with pure Pyrrolidone, the C-H stretching moves to lower wave number in $ZnSO_4$-Pyrrolidone caused by interaction between Pyrrolidone and water.

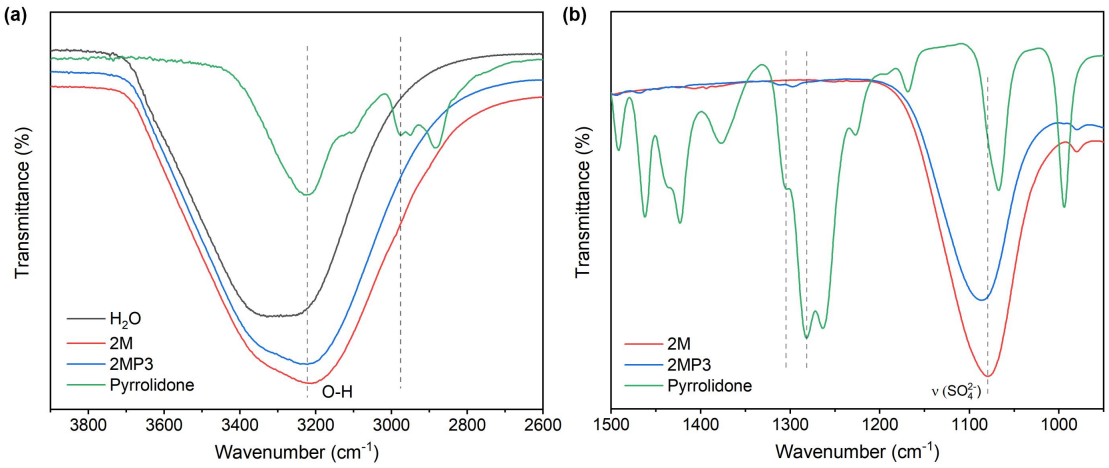

Figure 6.6 FT-IR spectra of 2 M $ZnSO_4$ electrolytes without and with different amount of Pyrrolidone at ATR mode. (a) 3900-2600 cm^{-1}, O-H stretching and (b) 1500-950 cm^{-1}, ν (SO_4^{2-}).

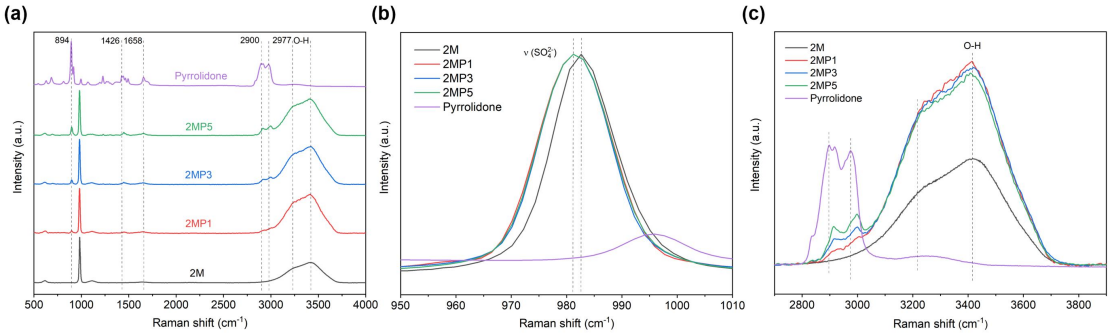

Figure 6.7 Raman spectra of 2 M $ZnSO_4$ electrolytes without and with different amount of Pyrrolidone. (a) 500-4000 cm^{-1} (b) 920-1180 cm^{-1} and (c) 3050-3650 cm^{-1}.

The strong interaction between Pyrrolidone and H_2O without interference of Zn^{2+} was evidenced *via* findings from FTIR, Figure 6.5. It can be seen in the figure that compared with $ZnSO_4$ electrolyte, the ν (SO_4^{2-}) vibration is shifted in 2MP3, Figure 6.6. This shift vibration is evidenced in the Raman spectra, Figure 6.6.

The contact angle of the Zn electrode in $ZnSO_4$-Pyrrolidone was determined as 69.0°, less than that in $ZnSO_4$ of 75.0°, Figure 6.7. This difference aids practically in a uniform electric distribution and production of homogeneous plating of Zn. The uniform deposition and suppressed corrosion result in high reversibility and stability of Zn chemistry.

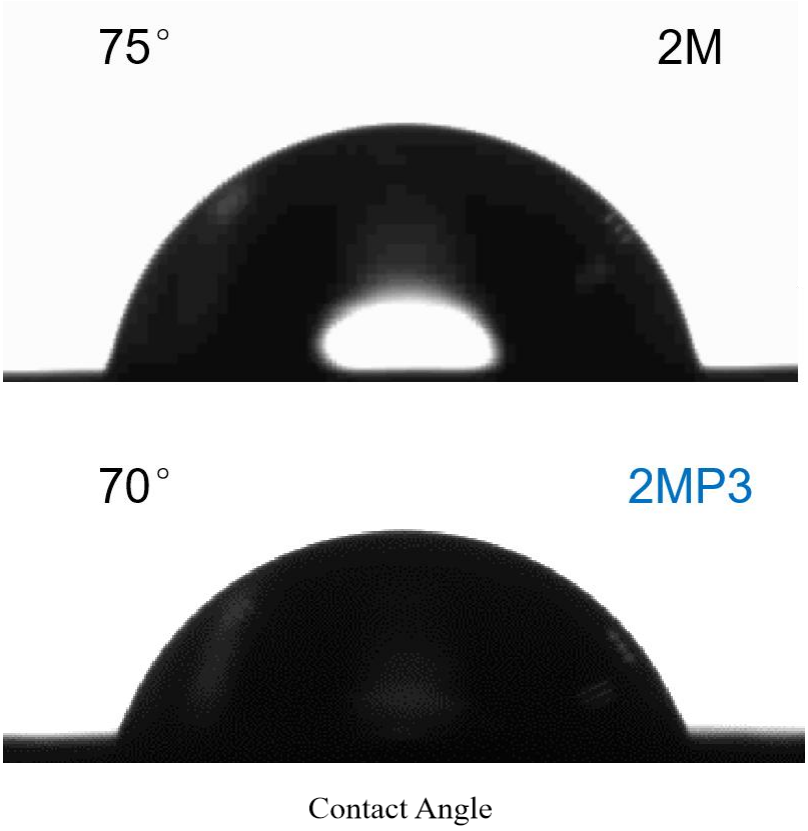

Figure 6.8 Contact angle 2M and 2MP3 electrolytes with Zn foil.

6.2.4 Mechanism Analysis

During Zn deposition, the hydrated $[Zn(H_2O)_n]^{2+}$ in pure $ZnSO_4$ electrolyte brings significant numbers of H_2O molecules that are reduced to release H_2. The increase in local pH because of H_2 evolution promotes formation of Zn^{2+}-insulating hydroxide zinc-salt passivation on the Zn surface and reduces Zn utilization and cycle life, and promotes Zn dendrite growth. In comparison with addition of Pyrrolidone, the average coordination number of Zn-H_2O in the primary hydration layer is reduced, and the bonding strength between Zn^{2+} ion and solvated H_2O is weakened. This additional interaction amongst Pyrrolidone, Zn^{2+}, SO_4^{2-} and H_2O rearranges the 'Zn^{2+}–H_2O–SO_4^{2-}–Pyrrolidone' bonding-network, reduces water activity and generation of by-product $(Zn(OH)_2)_3(ZnSO_4)(H_2O)_3$. Moreover, Pyrrolidone molecules absorb on the Zn surface, regulating the homogeneous distribution of Zn^{2+} flux and restricting uncontrolled 2D

diffusion that results in uniform and compact Zn deposition. Because of function in both electrolyte structure, and at the electrode-electrolyte interface, the Pyrrolidone additive boosts reversibility and cycling stability of Zn anodes. Importantly, because $ZnSO_4$-Pyrrolidone electrolyte is non-flammable (Figure 6.13), it is practically attractive for large-scale applications. Its high boiling and flash point contribute to safety and reduced risk of explosion including, in electrolyte leakage and thermal runaway.

6.3 Conclusion

3% organic additive, Pyrrolidone can be used to controllably manipulate typical $ZnSO_4$ electrolyte to give a highly stable and reversible aqueous zinc-ion battery (AZIB). Combined experiment, including FTIR and Raman analyzes reveals that the functional Pyrrolidone manipulates the electrolyte structure by rearranging the 'Zn^{2+}–H_2O–SO_4^{2-}–Pyrrolidone' bonding-network and altering Zn anode-electrolyte interface via absorbtion of Pyrrolidone on the Zn surface. This reduces the water activity, suppresses corrosion and generation of by-product, and gives a uniform compact Zn deposit. The anode ran over 1100 cycles (2200 h) with an average CE of 99.9 % under 1 mA cm^{-2} and 1 mA h cm^{-2}, and; exhibited stable and reversible Zn plating/stripping cycling for 456 h under testing conditions of 10 mA cm^{-2} and 10 mA h cm^{-2}. The reversibility and stability of the Zn anode significantly outperformed that using $ZnSO_4$ electrolyte. The Zn-MnO_2 full cells using $ZnSO_4$-Pyrrolidone electrolyte exhibited a high capacity of 400 mAh g^{-1} at 0.5 A g^{-1} and an improved cycling stability (350 % capacity retention following 1120 cycles). These findings offer a quantitative engineering strategy to boost reversibility and stability of Zn anodes in rechargeable AZIBs. Importantly, because the 2 M $ZnSO_4$-Pyrrolidone electrolyte is nonflammable, it makes AZIBs advantageous for large-scale and low-cost application in electrical-grid storage and clean energy storage.

References

[1] M. Li, J. Lu, Z. Chen, K. Amine, *Adv. Mater.* **2018**, *30*, 1800561.

[2] J. Wu, Y. Cao, H. Zhao, J. Mao, Z. Guo, *Carbon Energy* **2019**, *1*, 57-76.

[3] M. Song, H. Tan, D. Chao, H. J. Fan, *Adv. Funct. Mater.* **2018**, *28*, 1802564.

[4] T. Zhang, Y. Tang, S. Guo, X. Cao, A. Pan, G. Fang, J. Zhou, S. Liang, *Energy Environ. Sci.* **2020**, *13*, 4625-4665.

[5] S. L. Liu, R. Z. Zhang, J. F. Mao, Y. L. Zhao, Q. Cai, Z. P. Guo, *Science Advances*, **2022**, doi: 10.1126/sciadv.eabn5097.

[6] Y. Wang, Z. Wang, F. Yang, S. Liu, S. Zhang, J. Mao, Z. Guo, *Small* **2022**, doi: 10.1002/smll.202107033.

[7] F. Wang, O. Borodin, T. Gao, X. Fan, W. Sun, F. Han, A. Faraone, J. A. Dura, K. Xu, C. Wang, *Nat. Mater.* **2018**, *17*, 543-549.

[8] C. Zhang, J. Holoubek, X. Wu, A. Daniyar, L. Zhu, C. Chen, D. P. Leonard, I. A. Rodríguez-Pérez, J.-X. Jiang, C. Fang, X. Ji, *ChemComm* **2018**, *54*, 14097-14099.

[9] Y. Zhu, J. Yin, X. Zheng, A.-H. Emwas, Y. Lei, O. F. Mohammed, Y. Cui, H. N. Alshareef, *Energy Environ. Sci.* **2021**, *14*, 4463-4473.

[10] J. Zhao, J. Zhang, W. Yang, B. Chen, Z. Zhao, H. Qiu, S. Dong, X. Zhou, G. Cui, L. Chen, *Nano Energy* **2019**, *57*, 625-634.

[11] W. Yang, X. Du, J. Zhao, Z. Chen, J. Li, J. Xie, Y. Zhang, Z. Cui, Q. Kong, Z. Zhao, C. Wang, Q. Zhang, G. Cui, *Joule* **2020**, *4*, 1557-1574.

[12] J. Shi, T. Sun, J. Bao, S. Zheng, H. Du, L. Li, X. Yuan, T. Ma, Z. Tao, *Adv. Funct. Mater.* **2021**, *31*, 2102035.

[13] X. Lin, G. Zhou, M. J. Robson, J. Yu, S. C. T. Kwok, F. Ciucci, *Adv. Funct. Mater.* **2021**, *n/a*, 2109322.

[14] D. Han, C. Cui, K. Zhang, Z. Wang, J. Gao, Y. Guo, Z. Zhang, S. Wu, L. Yin, Z. Weng, F. Kang, Q.-H. Yang, *Nat. Sustain.* **2021**.

[15] S. Liu, J. Mao, W. K. Pang, J. Vongsvivut, X. Zeng, L. Thomsen, Y. Wang, J. Liu, D. Li, Z. Guo, *Adv. Funct. Mater.* **2021**, *31*, 2104281.

[16] J. Hao, L. Yuan, C. Ye, D. Chao, K. Davey, Z. Guo, S.-Z. Qiao, *Angew. Chem. Int. Ed.* **2021**, *60*, 7366-7375.

[17] N. Chang, T. Li, R. Li, S. Wang, Y. Yin, H. Zhang, X. Li, *Energy Environ. Sci.* **2020**, *13*, 3527-3535.

[18] J. Q. Huang, X. Y. Guo, X. Y. Lin, Y. Zhu, B. Zhang, *Research* **2019**, *2019*, 10.

[19] D. Wang, Q. Li, Y. Zhao, H. Hong, H. Li, Z. Huang, G. Liang, Q. Yang, C. Zhi, *Adv. Energy Mater.* **2022**, *n/a*, 2102707.

[20] H. Lu, X. Zhang, M. Luo, K. Cao, Y. Lu, B. B. Xu, H. Pan, K. Tao, Y. Jiang, *Adv. Funct. Mater.* **2021**, *31*, 2103514.

[21] J. Cui, X. Liu, Y. Xie, K. Wu, Y. Wang, Y. Liu, J. Zhang, J. Yi, Y. Xia, *Mater. Today Energy* **2020**, *18*, 100563.

[22] L. Cao, D. Li, E. Hu, J. Xu, T. Deng, L. Ma, Y. Wang, X.-Q. Yang, C. Wang, *J. Am. Chem. Soc.* **2020**, *142*, 21404-21409.

[23] P. Sun, L. Ma, W. Zhou, M. Qiu, Z. Wang, D. Chao, W. Mai, *Angew. Chem. Int. Ed.* **2021**, *60*, 18247-18255.

[24] L. Cao, D. Li, T. Pollard, T. Deng, B. Zhang, C. Yang, L. Chen, J. Vatamanu, E. Hu, M. J. Hourwitz, L. Ma, M. Ding, Q. Li, S. Hou, K. Gaskell, J. T. Fourkas, X.-Q. Yang, K. Xu, O. Borodin, C. Wang, *Nat. Nanotechnol.* **2021**, *16*, 902-910.

[25] L. Ma, T. P. Pollard, Y. Zhang, M. A. Schroeder, M. S. Ding, A. V. Cresce, R. Sun, D. R. Baker, B. A. Helms, E. J. Maginn, C. Wang, O. Borodin, K. Xu, *Angew. Chem. Int. Ed.* **2021**, *60*, 12438-12445.

[26] Q. Zhang, J. Luan, L. Fu, S. Wu, Y. Tang, X. Ji, H. Wang, *Angew. Chem. Int. Ed.* **2019**, *58*, 15841-15847.

[27] C. Huang, X. Zhao, S. Liu, Y. Hao, Q. Tang, A. Hu, Z. Liu, X. Chen, *Adv. Mater.* **2021**, *33*, 2100445.

[28] M. D. Yan, N. Dong, X. S. Zhao, Y. Sun, H. L. Pan, *ACS Energy Lett.* **2021**, *6*, 3236-3243.

[29] X. Zeng, K. Xie, S. Liu, S. Zhang, J. Hao, J. Liu, W. K. Pang, J. Liu, P. Rao, Q. Wang, J. Mao, Z. Guo, *Energy Environ. Sci.* **2021**, *14*, 5947-5957.

[30] D. Belov, D. T. Shieh, *J Solid State Electrochem* **2012**, *16*, 603-615.

[31] T. Doi, Y. Shimizu, M. Hashinokuchi, M. Inaba, *ChemElectroChem* **2017**, *4*, 2398-2403.

Table 6.1 Boiling point, flash point and solubility (25 °C) of selected rganic additives in electrolyte of AZIBs.

Organic additive	**Boiling point (°C)**	**Flash point (°C)**	**Solubility in water (25 °C)**	**Viscosity (mPa·s)**
AM (acrylamide)	231.7	79.0 ± 19.8	Soluble	
Amino acid Arg	367.6 ± 52	176.1 ± 30.7	Soluble	
AN (acetonitrile)	63.5	5.6	Soluble	0.325-0.375
DME (1,2-dimethoxyethane)	84.5	0.0	Soluble	1.1
DMSO (dimethyl sulfoxide)	189.0 ± 9.0	85.0	Miscible	1.1
Et (erythritol)	330.0	208.7 ± 21.1	Soluble	
EC (ethyl carbonate)	126.8	31.1	Insoluble	0.748-0.868
EMC (ethyl methyl carbonate)	107.5	26.7 ± 7.8	Immiscible	0.65
EG (ethylene glycol)	197.5	108.2 ± 13.0	Miscible	10.38-86.9
Glucose	527.1 ± 50.0	286.7± 26.6	Freely soluble	
Glycerol	290.0	160.0	Soluble	18-243
Maltose	667.9 ± 55.0	357.8 ± 31.5	Very soluble	
Methanol	48.1 ± 3.0	11.1	Miscible	0.5142-0.6405
Na_2EDTA	> 100	325.2	Miscible	
PAM (polyacrylamide)	231.7	79.0 ± 19.8	Soluble	
Sac (saccharin)	438.9 ± 28.0	219.3 ± 24.0	Slightly soluble	
SL (sulfolane)	285.6 ± 8.0	165.6	Soluble	10.286
SN (succinonitrile)	268.5 ± 13.0	141.1 ± 13.7	Slightly	2.591

			soluble	
TEP (triethyl phosphate)	219.3 ± 8.0	115.6	Soluble	N/A
TFEP (tris(2,2,2-trifluoroethyl) phosphate)	176.2 ± 40.0	60.4 ± 27.3	N/A	N/A
TMP (trimethyl phosphate)	197.2	83.7 ± 38.8	Soluble	N/A
Urea	165.1 ± 23.0	53.7± 22.6	Soluble	
Pyrrolidone (This work)	250	138	Miscible	N/A

Table 6.2 Comparison of accumulative plated capacity with current density of selected organic additives in electrolyte of AZIBs.

Organic additive	**Current density ($mA\ cm^{-2}$)**	**Accumulative plated capacity ($mAh\ cm^{-2}$)**	**Reference**
AM	10	900	7
	2	380	
	1	340	
Amino acid Arg	5	5500	8
	10	4500	
	1	1475	
AN	1	650	9
	2	600	
	0.5	250	
BIS-TRIS	5	1500	10
	1	625	
CT3G30	2	800	11
DME	2	375	12

DMSO	0.5	250	13
Et_2O	0.2	25	15
EG	2	135	16
Glucose	1	1000	17
	5	687.5	
Glycerol	2	900	18
	1	750	
ILZE	2	1500	19
Maltose	1	600	20
Methanol	1	450	21
$Me_3EtNOTF$	0.5	1500	1
Na_2EDTA	5	5000	22
	2	450	
P_{4441}-TFSI	0.5	1600	23
	1	400	
	2.5	350	
PAM	20	1100	24
	2	170	
	1	90	
PEG-400	2	8000	25
	1	4500	
	0.5	2000	
PEO-4000	1	600	26
PEO-100000	1	1500	27
Saccharin	10	2750	28
	40	1100	

SDBS	0.5	375	29
SL	0.5	200	30
SN	0.2	40	31
	0.05	20	
TBA_2SO_4	10	2000	32
	5	1125	
	2	300	
TC	5	1250	33
	1	1072.5	
	10	850	
TEP	1	750	34
TEP-PC	0.5	650	35
TFEP	0.5	175	36
TMP-DMC/DMF	1	2500	37
Trisodium citrate	5	100	38
Urea	0.1	120	39a
	1	350	39b
Pyrrolidone	**10**	**2280**	**This work**
	20	**900**	
	1	**600**	

Table 6.3 Comparison of Coulombic efficiency (CE) and cumulaltive plated capacity for Zn half cells with selected organic additives in electrolyte of AZIBs.

Organic additive	**Cumulative plated capacity ($Ah\ cm^{-2}$)**	**CE (%)**	**Reference**
AM	0.04	N/A	7

Amino acid Arg	0.325	98.3[a]	8
AN	0.3	99.3[a]	9
BIS-TRIS	0.4	98.5[a]	10
DME	0.156	N/A	12
DMSO	0.2	99.5[a]	13
EG	0.12	98[a]	16
Glucose	0.1	97.3[a]	17
Glycerol	0.5	98.3[a]	18
ILZE	0.3	99.36[b]	19
Maltose	0.032	99.7[a]	20
Methanol	0.45	99.7[a]	21
$Me_3EtNOTF$	0.5	99.8[a]	1
Na_2EDTA	0.7	99.5[a]	22
P_{4441}-TFSI	N/A	98.1[a]	23
PEO-4000	0.35	98.7[b]	26
PEO-100000	1.5	99.5[b]	27
Saccharin	0.5	99.6[a]	28
SL	0.05	98[b]	30
SN	0.025	98.4[a]	31
TBA_2SO_4	N/A	98[b]	32
TC	750 cycles at 1 mA cm^{-2}	97.7[b]	33
TEP	0.126	99.5[a]	34
TEP-PC	N/A	97.7[b]	35
TFEP	0.175	99.1[a]	36
TMP	5	99.57[a]	37
Urea	N/A	96.2[b]	39a

Pyrrolidone	**1.1**	**99.9[a]**	**This work**

[a] average CE, [b] reaches until stable CE, N/A: not available.[2]

References

[1] L. Cao, D. Li, T. Pollard, T. Deng, B. Zhang, C. Yang, L. Chen, J. Vatamanu, E. Hu, M. J. Hourwitz, L. Ma, M. Ding, Q. Li, S. Hou, K. Gaskell, J. T. Fourkas, X.-Q. Yang, K. Xu, O. Borodin, C. Wang, *Nat. Nanotechnol.* **2021**, *16*, 902-910.

[2] A. Bernardi, R. Faller, D. Reith, K. N. Kirschner, *Softwarex* **2019**, *10*, 100241.

[3] a) W. L. Jorgensen, J. Tirado-Rives, *Proc. Natl. Acad. Sci. U.S.A.* **2005**, *102*, 6665; b) L. S. Dodda, J. Z. Vilseck, J. Tirado-Rives, W. L. Jorgensen, *J. Phys. Chem. B* **2017**, *121*, 3864-3870.

[4] G. Bussi, D. Donadio, M. Parrinello, *J. Chem. Phys.* **2007**, *126*, 014101.

[5] H. J. C. Berendsen, J. P. M. Postma, W. F. van Gunsteren, A. DiNola, J. R. Haak, *J. Chem. Phys.* **1984**, *81*, 3684-3690.

[6] a) P. E. Blöchl, *Phys. Rev. B* **1994**, *50*, 17953-17979; b) B. Hammer, L. B. Hansen, J. K. Nørskov, *Phys. Rev. B* **1999**, *59*, 7413-7421; c) G. Kresse, D. Joubert, *Phys. Rev. B* **1999**, *59*, 1758-1775; d) J. Tao, J. P. Perdew, V. N. Staroverov, G. E. Scuseria, Phys. Rev. Lett. **2003**, *91*, 146401; e) S. Lebègue, O. Eriksson, *Phys. Rev. B* **2009**, *79*, 115409.

[7] X. Zeng, X. Meng, W. Jiang, M. Ling, L. Yan, C. Liang, *Electrochim. Acta* **2021**, *378*, 138106.

[8] H. Lu, X. Zhang, M. Luo, K. Cao, Y. Lu, B. B. Xu, H. Pan, K. Tao, Y. Jiang, *Adv. Funct. Mater.* **2021**, *31*, 2103514.

[9] J. Shi, K. Xia, L. Liu, C. Liu, Q. Zhang, L. Li, X. Zhou, J. Liang, Z. Tao, *Electrochim. Acta* **2020**, *358*, 136937.

[10] M. Luo, C. Wang, H. Lu, Y. Lu, B. B. Xu, W. Sun, H. Pan, M. Yan, Y. Jiang, *Energy Stor. Mater.* **2021**, *41*, 515-521.

[11] M. Chen, J. Chen, W. Zhou, X. Han, Y. Yao, C.-P. Wong, *Adv. Mater.* **2021**, *33*, 2007559.

[12] J. Cui, X. Liu, Y. Xie, K. Wu, Y. Wang, Y. Liu, J. Zhang, J. Yi, Y. Xia, *Mater. Today Energy* **2020**, *18*, 100563.

[13] L. Cao, D. Li, E. Hu, J. Xu, T. Deng, L. Ma, Y. Wang, X.-Q. Yang, C. Wang, *J. Am. Chem. Soc.* **2020**, *142*, 21404-21409.

[14] Z. Huang, T. Wang, X. Li, H. Cui, G. Liang, Q. Yang, Z. Chen, A. Chen, Y. Guo, J. Fan, C. Zhi, *Adv. Mater.* **2021**, *n/a*, 2106180.

[15] W. Xu, K. Zhao, W. Huo, Y. Wang, G. Yao, X. Gu, H. Cheng, L. Mai, C. Hu, X. Wang, *Nano Energy* **2019**, *62*, 275-281.

[16] N. Chang, T. Li, R. Li, S. Wang, Y. Yin, H. Zhang, X. Li, *Energy Environ. Sci.* **2020**, *13*, 3527-3535.

[17] P. Sun, L. Ma, W. Zhou, M. Qiu, Z. Wang, D. Chao, W. Mai, *Angew. Chem. Int. Ed.* **2021**, *60*, 18247-18255.

[18] Y. Zhang, M. Zhu, K. Wu, F. Yu, G. Wang, G. Xu, M. Wu, H.-K. Liu, S.-X. Dou, C. Wu, Journal of Materials Chemistry A **2021**, *9*, 4253-4261.

[19] L. Ma, S. Chen, N. Li, Z. Liu, Z. Tang, J. A. Zapien, S. Chen, J. Fan, C. Zhi, *Adv. Mater.* **2020**, *32*, 1908121.

[20] W. Chen, S. Guo, L. Qin, L. Li, X. Cao, J. Zhou, Z. Luo, G. Fang, S. Liang, *Adv. Funct. Mater.* **2022**, *n/a*, 2112609.

[21] J. Hao, L. Yuan, C. Ye, D. Chao, K. Davey, Z. Guo, S.-Z. Qiao, *Angew. Chem. Int. Ed.* **2021**, *60*, 7366-7375.

[22] S.-J. Zhang, J. Hao, D. Luo, P.-F. Zhang, B. Zhang, K. Davey, Z. Lin, S.-Z. Qiao, *Adv. Energy Mater.* **2021**, *11*, 2102010.

[23] L. Ma, T. P. Pollard, Y. Zhang, M. A. Schroeder, M. S. Ding, A. V. Cresce, R. Sun, D. R. Baker, B. A. Helms, E. J. Maginn, C. Wang, O. Borodin, K. Xu, *Angew. Chem. Int. Ed.* **2021**, *60*, 12438-12445.

[24] Q. Zhang, J. Luan, L. Fu, S. Wu, Y. Tang, X. Ji, H. Wang, *Angew. Chem. Int. Ed.* **2019**, *58*, 15841-15847.

[25] Y. Wu, Z. Zhu, D. Shen, L. Chen, T. Song, T. Kang, Z. Tong, Y. Tang, H. Wang, C. S. Lee, *Energy Stor. Mater.* **2022**, *45*, 1084-1091.

[26] M. Yan, C. Xu, Y. Sun, H. Pan, H. Li, *Nano Energy* **2021**, *82*, 105739.

[27] Y. Jin, K. S. Han, Y. Shao, M. L. Sushko, J. Xiao, H. Pan, J. Liu, *Adv. Funct. Mater.* **2020**, *30*, 2003932.

[28] C. Huang, X. Zhao, S. Liu, Y. Hao, Q. Tang, A. Hu, Z. Liu, X. Chen, *Adv. Mater.* **2021**, *33*, 2100445.

[29] J. Hao, J. Long, B. Li, X. Li, S. Zhang, F. Yang, X. Zeng, Z. Yang, W. K. Pang, Z. Guo, *Adv. Funct. Mater.* **2019**, *29*, 1903605.

[30] X. Lin, G. Zhou, M. J. Robson, J. Yu, S. C. T. Kwok, F. Ciucci, *Adv. Funct. Mater.* **2021**, *n/a*, 2109322.

[31] W. Yang, X. Du, J. Zhao, Z. Chen, J. Li, J. Xie, Y. Zhang, Z. Cui, Q. Kong, Z. Zhao, C. Wang, Q. Zhang, G. Cui, *Joule* **2020**, *4*, 1557-1574.

[32] A. Bayaguud, X. Luo, Y. Fu, C. Zhu, *ACS Energy Lett.* **2020**, *5*, 3012-3020.

[33] R. Yao, L. Qian, Y. Sui, G. Zhao, R. Guo, S. Hu, P. Liu, H. Zhu, F. Wang, C. Zhi, C. Yang, *Adv. Energy Mater.* **2022**, *12*, 2102780.

[34] S. Liu, J. Mao, W. K. Pang, J. Vongsvivut, X. Zeng, L. Thomsen, Y. Wang, J. Liu, D. Li, Z. Guo, *Adv. Funct. Mater.* **2021**, *31*, 2104281.

[35] X. Qiu, N. Wang, X. Dong, J. Xu, K. Zhou, W. Li, Y. Wang, *Angew. Chem. Int. Ed.* **2021**, *60*, 21025-21032.

[36] L. Cao, D. Li, E. Hu, J. Xu, T. Deng, L. Ma, Y. Wang, X.-Q. Yang, C. Wang, *J. Am. Chem. Soc.* **2020**, *142*, 21404-21409.

[37] A. Naveed, H. Yang, Y. Shao, J. Yang, N. Yanna, J. Liu, S. Shi, L. Zhang, A. Ye, B. He, J. Wang, *Adv. Mater.* **2019**, *31*, 1900668.

[38] N. Wang, S. Zhai, Y. Ma, X. Tan, K. Jiang, W. Zhong, W. Zhang, N. Chen, W. Chen, S. Li, G. Han, Z. Li, *Energy Stor. Mater.* **2021**, *43*, 585-594.

[39] a) J. Zhao, J. Zhang, W. Yang, B. Chen, Z. Zhao, H. Qiu, S. Dong, X. Zhou, G. Cui, L. Chen, *Nano Energy* **2019**, *57*, 625-634; b) Z. Hou, M. Dong, Y. Xiong, X. Zhang, H. Ao, M. Liu, Y. Zhu, Y. Qian, *Small* **2020**, *16*, 2001228.

CHAPTER 7 Conclusion and Prospects

7.1 Conclusion

To achieve the strategies of the European Commission's (EC) green deal and recovery plan. Rechargeable batteries are one of the most important technologies to store and transfer energy, for large-scale application including the innovational electronics, such as autonomous robotics, electric scooters, delivery drones, sensors, wearable devices, especially for medical use and power tools.[1] Aqueous Zn-ion batteries have been regarded as the promising alternative of LIBs for large-scale application due to their advantages of low cost, high performance, safety index, and environmental benignity. However, the state-of-the-art aqueous Zn battery is still far from meeting the ever-increasing large-scale energy demands. In this doctoral thesis, recent progress on the aqueous ZIBs with mild electrolyte have been comprehensively summarized, including the Mn-based cathode materials, Zn-ion storage mechanism, electrolyte formulation, and Zn electrode. Zn metal electrode persistently suffer from the poor reversibility and low CE in the mild electrolyte, which seriously restricted further development of Zn-based batteries. To effectively enhance the Zn performance, we proposed the strategy of strong absorption energy to suppress Zn dendrite and resolve other issues, including adding the electrolyte additive, building the absorbed organic buffer layers on protrusions of Zn electrode surface.

In the first case, relatively low content organic molecules, (MSM) can be used to controllably manipulate typical $ZnSO_4$ electrolyte to give a highly stable and reversible aqueous zinc-ion battery (AZIB). Combined experiment, including FTIR and Raman analyzes reveals that the functional MSM manipulates the electrolyte structure by rearranging the 'Zn^{2+}–H_2O–SO_4^{2-}–MSM' bonding-network and altering Zn anode-electrolyte interface via absorbtion of MSM on the Zn surface. This reduces the water activity, suppresses corrosion and generation of by-product, and gives a uniform compact Zn deposit. The anode ran over

900 cycles (1800 h) with an average CE of 99.9 % under 1 mA cm^{-2} and 1 mA h cm^{-2}, and; exhibited stable and reversible Zn plating/stripping cycling for 460 h under testing conditions of 5 mA cm^{-2} and 5 mA h cm^{-2}. The reversibility and stability of the Zn anode was improved outperformed that using $ZnSO_4$ electrolyte. The Zn-MnO_2 full cells using $ZnSO_4$-MSM electrolyte exhibited a high capacity of 272 mAh g^{-1} at 0.5 A g^{-1} and an improved cycling stability (125 % capacity retention following 700 cycles). These findings offer a quantitative engineering strategy to boost reversibility and stability of Zn anodes in rechargeable AZIBs. Importantly, because the 2 M $ZnSO_4$-MSM electrolyte is nonflammable, it makes AZIBs advantageous for large-scale and low-cost application in electrical-grid storage and clean energy storage.

In the second case, trace low vapour pressure organic solvent, gamma butyrolactone (GBL), is introduced into the typical ZnSO4 electrolyte to achieve highly stable and reversible AZIBs. Experiments (NMR, FTIR, Raman) and theoretical calculations (MD, DFT) suggest that the functional GBL can not only manipulate the electrolyte structure by rearranging the "Zn^{2+}−H_2O−SO_4^{2-}−GBL" bonding network, but also alter the Zn anode-electrolyte interface by absorbing GBL molecules on Zn surface. Both of the functions help in reducing the water activity, suppressing the corrosion and the generation of by-product, and enabling the uniform and compact Zn deposition. As a result, the Zn anodes run over 2720 cycles (5440 h) with average Coulombic efficiency of 99.9% under 1 mA cm^{-2} and 1 mA h cm^{-2}. The Zn anodes also present a stable and reversible Zn plating/stripping cycling for 1170 h under harsh testing conditions (10 mA cm^{-2} and 10 mA h cm^{-2}). Such the reversibility and stability of Zn anodes are far surpassing that using $ZnSO_4$ electrolyte. Moreover, the Zn-MnO_2 full cells using $ZnSO_4$-GBL electrolyte can deliver a higher capacity of 287 mAh g-1 at 0.5 A g^{-1} and improved cycling stability (87% capacity retention after 400 cycles) demonstrating the effectiveness of the GBL additive. At higher current density (1A g^{-1} and 5 A g^{-1}), Zn-MnO_2 full cells using $ZnSO_4$-GBL also exhibited more stable and higher capacity cycling performance. Importantly, the 2M $ZnSO_4$-GBL electrolyte is nonflammable, which makes AZIBs promising for large scale applications.

In the third case, 3% organic additive, Pyrrolidone can be used to controllably manipulate typical $ZnSO_4$ electrolyte to give a highly stable and reversible aqueous zinc-ion battery (AZIB). Combined experiment, including FTIR and Raman analyzes reveals that the functional Pyrrolidone manipulates the electrolyte structure by rearranging the 'Zn^{2+}–H_2O–SO_4^{2-}—Pyrrolidone' bonding-network and altering Zn anode-electrolyte interface via absorbtion of Pyrrolidone on the Zn surface. This reduces the water activity, suppresses corrosion and generation of by-product, and gives a uniform compact Zn deposit. The anode ran over 1100 cycles (2200 h) with an average CE of 99.9 % under 1 mA cm^{-2} and 1 mA h cm^{-2}, and; exhibited stable and reversible Zn plating/stripping cycling for 456 h under testing conditions of 10 mA cm^{-2} and 10 mA h cm^{-2}. The reversibility and stability of the Zn anode significantly outperformed that using $ZnSO_4$ electrolyte. The Zn-MnO_2 full cells using $ZnSO_4$-Pyrrolidone electrolyte exhibited a high capacity of 400 mAh g^{-1} at 0.5 A g^{-1} and an improved cycling stability (350 % capacity retention following 1120 cycles). These findings offer a quantitative engineering strategy to boost reversibility and stability of Zn anodes in rechargeable AZIBs. Importantly, because the 2 M $ZnSO_4$-Pyrrolidone electrolyte is nonflammable, it makes AZIBs advantageous for large-scale and low-cost application in electrical-grid storage and clean energy storage.

Additive (BP, FP, solubility at 25 ℃)	Amount (mol L^{-1}) or volume (%)	Mechanism	Battery type	Zn-Zn symmetrical cell		Zn-Cu half cell		Zn-MnO_2 full cell	
				Current density (mA cm^{-2})	Accumulative plated capacity (mAh cm^{-2})	Cumulative plated capacity (mAh cm^{-2})	CE (%)	Current density (A g^{-1})	Capacity (mAh g^{-1}) @ cycle
Methyl Sulfonyl Methane (358.8, 185, miscible)	0.9 M	Strong adsorption, change of solvation structure, buffer layer on Zn surface	2032 Coin-type	5	1350	850	99.9	0.5	272 @ 700
				1	600				
Gamma butyrolactone (204, 99.2, miscible)	1 %			10	5850	2722	99.9		287 @ 400
				1	2720				
				20	1400				
Pyrrolidone (250, 138, miscible)	3 %			10	2280	1100	99.9		400 @ 1120
				20	900				
				1	600				

Table 7.1 The summary of properties and battery performance of Methyl Sulfonyl Methane, Gamma butyrolactone, and Pyrrolidone.

7.2 Prospects for future work

Zn electrode: large number of reported aqueous ZIBs and Zn hybrid batteries directly use commercial Zn foil as the Zn anode. However, it suffers from several irreversibility issues during the cycling process in mild aqueous electrolytes, such as the dendrite growth, corrosion, as well as hydrogen evolution, which will affect the cycling performance of Zn-based systems. Until now, only limited work focused on the optimization of Zn metal and the Zn electrode reversibility behaviour under the aqueous mild electrolytes is not well understood. The effective methods to suppress the dendrite growth and achieve high CE should be building a stable artificial layer (organic buffer layer or inorganic thin, compact and high conductivity of SEI layer) on Zn electrode surface and optimizing the electrolyte formulation. More progresses are desired to be achieved by learning from other metal anode protecting technology such as Li/Li-S/Na metal batteries. Moreover, the strategies for improving the performance of Zn electrode (proper thickness for N/P ratio) should be demonstrated in full cells towards practical applications.

Electrolyte: The optimization of the electrolyte is critical for achieving high performance batteries by enabling highly efficient Zn plating/stripping and stabilizing the cathode materials, which are related to the Zn salts, salt concentrations, elements and additives. However, batteries using $ZnSO_4$ electrolyte still suffer from the rapid capacity decay due to the formation and growth of Zn dendrites and electrode dissolution. In addition, the formation and dissolution of hydroxide sulphate ($Zn_4(OH)_6SO_4 \cdot xH_2O$) associated with ZnSO4 electrolyte still needs to be understood, as well as the effect on the electrochemical performance. Batteries employing the $Zn(CF_3SO_3)_2$ electrolyte show superior electrochemical properties compare to these using $ZnSO_4$ electrolyte, the high price of $Zn(CF_3SO_3)_2$ severely retards its wide application on a large scale, however. Thus, exploring the new Zn salts or Zn composites with affordable price will be worthwhile to boost the potential of Zn-based systems by enhancing the CE, cycling stability and rate performance, and more importantly suppressing Zn dendrite growth. In addition, most of the aqueous Zn salt electrolytes are

actually the mild acidic electrolyte (pH 4 ~ 6), where the issues of corrosion of the metal and current collector should be considered and resolved. Moreover, the narrow electrochemical window of aqueous electrolyte would trigger the water-based side reactions and limit the operating voltage of cathode materials. Efforts are still highly desirable to research the new additives or electrolyte concentration, aiming to explore the electrolyte additives from working temperature range, thermal stability, cost, high ionic conductivity, viscosity, chemical stability and bring more potential materials into Zn-based system. And we could analysis and screen out the most reliable and valuable electrolyte-additive system by the characterization including FTIR, Raman, NMR, DSC, EXAFS and simulation, etc.

Configuration: Currently, the vast majority of work about ZIBs and hybrid Zn batteries are still conducted in the coin cell or pouch cell. To meet the different demands at the future market, the different types of aqueous Zn-based technologies should be available in parallel, including coin cell, pouch cell, cylindrical cell (18650) and prismatic cell. An additional challenge is whether strategies suitable for coin cells will work in large-scale cells, for practical application, materials should be demonstrated in large-scale cells. In addition, wearable and flexible electronics with high flexibility and reliable electrochemical properties is a vibrant and active research area for the large demand of portable applications. Benefiting from its green and sustainable features, flexible aqueous or all-solid-sate Zn-based devices may be a good choice for practical wearable applications. However, only few works focused on flexible Zn-based batteries in neutral or mild acidic media was proposed until now due to the limitations of stable electrode materials and appropriate electrolyte. Therefore, new strategies are highly needed to develop new materials and electrolyte with both excellent electrical conductivity and outstanding flexibility for the further development of well-designed and safe Zn-based batteries.[1]

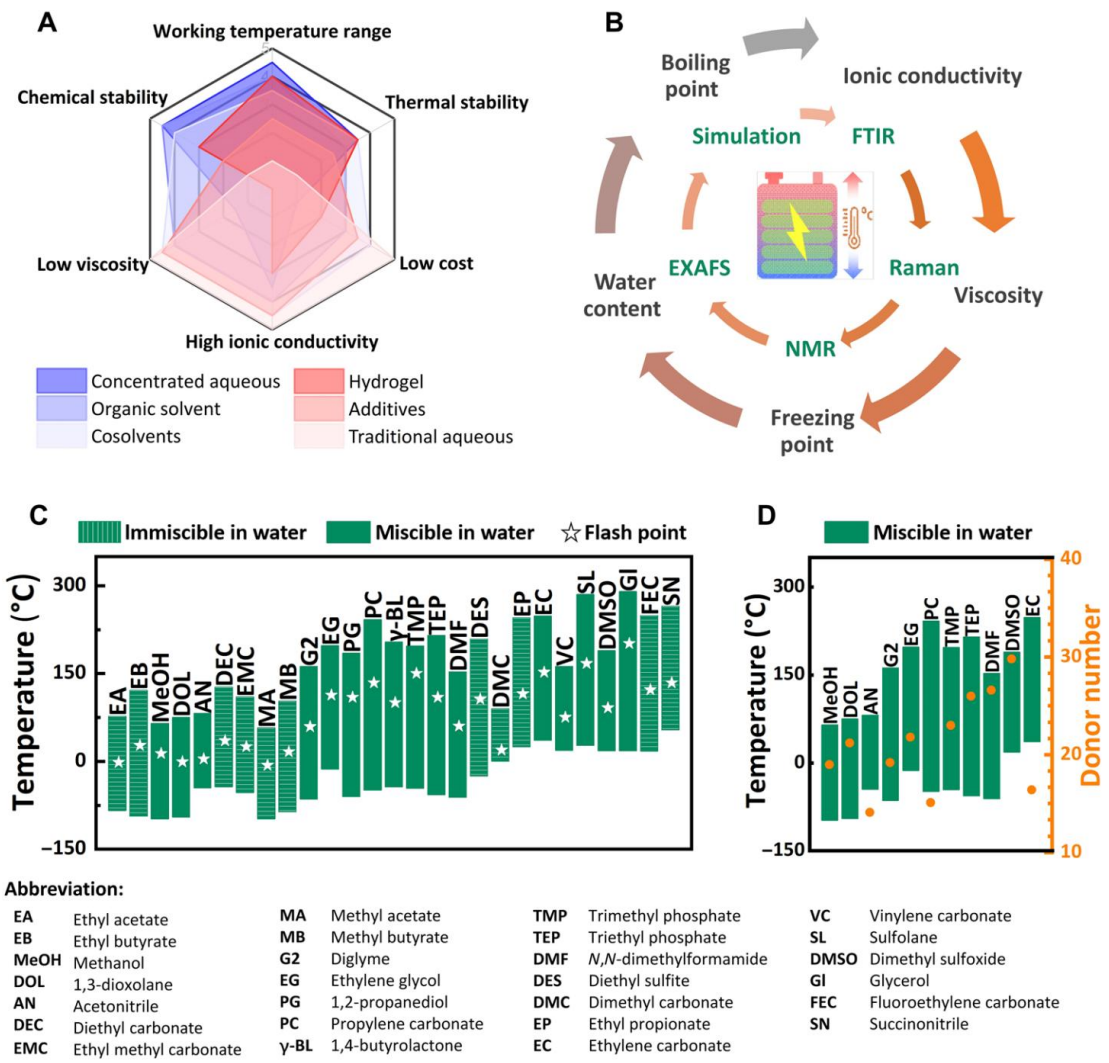

Figure 7.2 Comparison of different electrolyte design strategies and potential candidates as solvents or additives/cosolvents for AZIBs that can operate at harsh temperatures. (A) Spider chart for an itemized comparison of different types of electrolytes in AZIBs based on their summarized performances. (B) The key parameters and in-depth analysis techniques for the study of electrolytes intended for harsh temperature applications. (C) Liquid temperature range, miscibility in water, and flash point of organic solvents that are promising to use in AZIBs for harsh temperature application. (D) Liquid temperature range and DN of water-miscible organic solvents that are promising candidates as additives/cosolvents for AZIBs operating at harsh temperatures. [1]

To go beyond the state-of-the-art the battery chemistry, more sustainable, more scalable, and faster research approaches are required that simultaneously consider the need for novel electrolytes and new concepts for faster exploration and scaling-up (experimentally and theoretically). Moreover, we also could focus on the innovation in reinvent the way we invent the batteries of the future.[2]

References

[1] S. Liu, R. Zhang, J. Mao, Y. Zhao, Q. Cai, Z. Guo. *Sci. Adv.* **2022**, *8*, eabn5097.

[2] K. Edström, E. Ayerbe, I.E. Castelli, I.C. Laskovic, R. Dominko, A. Grimaud, T. Vegge, and W. Wentzel. *Adv. Energy Mater.* **2022**, *12*, 202200644.

Appendix A: Publications

1. ***Haiji Huang***, Dongmei Xie, Jiachang Zhao, Pinhua Rao*, Won Mook Choi*, Kenneth Davey, Jianfeng Mao*. Boosting reversibility and stability of Zn anodes via manipulation of electrolyte structure and interface with addition of trace organic molecules. Under review.
2. Yinong Wang[#], ***Haiji Huang***[#] and Won Mook Choi*. Polypyrrole decorated cobalt carbonate hydroxide on carbon cloth for high performance flexible supercapacitor electrodes. Journal of Alloys and Compounds 886 (2021) 161171.
3. ***Haiji Huang***, Pinhua Rao and Won Mook Choi*. Carbon-coated silicon/crumpled graphene composite as anode material for lithium-ion batteries. Current Applied Physics 19 (2019) 1349-1354.
4. Dongmei Xie, Jiachang Zhao, Qiong Jiang, Hao Wang, ***Haiji Huang***, Pinhua Rao, Jianfeng Mao. A high-performance alginate hydrogel binder for aqueous Zn-ion batteries. Under review

Appendix B: Conferences & Activities

1. KOBS 한국전지학회 2018 년도 춘계 학술대회
2. 2019 KIChE Spring Meeting 한국화학공학회 2019 년도 봄 총회 및 학술대회
3. 2020 KIChE Spring Meeting 한국화학공학회 2020 년도 봄 총회 및 학술대회